

Alma Mater Studiorum – Università di Bologna

DOTTORATO DI RICERCA IN ALTO APPRENDISTATO  
IN INGEGNERIA ELETTRONICA, DELLE TELECOMUNICAZIONI  
E TECNOLOGIE DELL'INFORMAZIONE, IN COLLABORAZIONE  
CON RETE FERROVIARIA ITALIANA

Ciclo XXIX

**Settore Concorsuale di afferenza:** 09/F2 - TELECOMUNICAZIONI

**Settore Scientifico disciplinare:** ING-INF/03 - TELECOMUNICAZIONI

EVOLUTION OF COMMUNICATION AND MONITORING SYSTEMS  
FOR THE MANAGEMENT OF TRAFFIC  
AND SAFETY CONTROL SYSTEMS IN RAILWAY SITES

**Presentata da:** Marco Govoni

**Coordinatore Dottorato**

Prof. Ing. A. Vanelli-Coralli

**Relatore**

Prof. Ing. D. Dardari

**Correlatori**

Prof. Ing. V. Degli Esposti

Prof. Ing. G. Tartarini

**Supervisore RFI:**

Ing. G. Sorbello

**Esame finale anno 2017**



# Contents

<b>Introduction</b>	<b>4</b>
<b>1 Integrated Automatic Protection of LC (PAI-PL)</b>	<b>9</b>
1.1 Safety Requirements . . . . .	9
1.2 Surveillance Systems State of the Art . . . . .	12
1.3 ultrawide-band (UWB) Radar Overview . . . . .	15
1.3.1 Ultra Wideband Technology . . . . .	15
1.3.2 UWB Partial multi-static Radar: Overview . . . . .	16
<b>2 Ray-Tracing</b>	<b>18</b>
2.1 Introduction to Ray-Tracing . . . . .	19
2.1.1 Reflection, Refraction and diffraction . . . . .	20
2.1.2 Diffuse Scattering . . . . .	21
2.2 3D Scat RT Simulator . . . . .	23
2.2.1 Input files . . . . .	23
2.2.2 Transmitter and Receiver files . . . . .	24
2.2.3 Run parameters . . . . .	26
2.2.4 Output . . . . .	26
2.3 Post Processing and $H(f)$ for PAI-PL Scenario . . . . .	28
<b>3 Radio-over-Fiber</b>	<b>31</b>
3.1 State-of-the-art of RoF systems . . . . .	31
3.1.1 Impairments in Analogue ROF Systems . . . . .	33
3.2 UWB-over-fiber in railway scenario . . . . .	34
<b>4 UWB PAI-PL with Fixed Object Scanning</b>	<b>39</b>
4.1 UWB sensor networks: Overview . . . . .	39
4.2 Multi-static UWB radar and Imaging scanner radar . . . . .	41

4.2.1	Multi-static UWB radar . . . . .	41
4.2.2	Imaging scanner radar . . . . .	43
4.3	Advantages and disadvantage of Multi-static and Imaging radars . . .	46
4.4	The FOS Imaging Algorithm . . . . .	47
4.4.1	Signal Model . . . . .	48
4.4.2	Clutter Removal and Ghost Effect Mitigation . . . . .	49
4.4.3	3D Image Formation . . . . .	50
4.4.4	Obstacle Volume Estimation . . . . .	53
<b>5</b>	<b>Simulation Results</b>	<b>55</b>
5.1	Simulation results with multi-static radar approach . . . . .	56
5.2	Simulation results with FOS algorithm . . . . .	57
5.3	UWBoF Simulation Results . . . . .	59
<b>6</b>	<b>Experimental Results</b>	<b>64</b>
6.1	Time Domain devices . . . . .	65
6.2	Mono-static Measurements . . . . .	66
6.2.1	Mono-static Setup . . . . .	67
6.2.2	Mono-static measurement results . . . . .	69
6.3	Bi-static Measurements . . . . .	71
6.3.1	Bi-static Setup . . . . .	72
6.3.2	Bi-static Measurements results . . . . .	73
6.4	Multi-static radar Measurements . . . . .	74
6.4.1	Multi-static Setup . . . . .	75
6.4.2	Multi-static Measurements results . . . . .	75
<b>7</b>	<b>Conclusions</b>	<b>78</b>
<b>A</b>	<b>RayTracing files</b>	<b>81</b>
A.1	Reference Scenario . . . . .	81
A.2	Run Time File and auxiliary parameters . . . . .	83
<b>B</b>	<b>Software tool for experimental measurements</b>	<b>86</b>
B.1	Monostatic Radar Module (MRM) . . . . .	86
B.1.1	Configuration of Parameters . . . . .	87
B.1.2	Logging File . . . . .	88
B.2	Channel Analysis Tool (CAT) . . . . .	89

B.2.1	Parameter Settings . . . . .	90
	<b>Bibliography</b>	<b>93</b>



# List of Figures

1	Cost-Effectiveness PL actions . . . . .	3
2	PAI-PL operational principle . . . . .	7
1.1	Different PAI-PL technologies . . . . .	11
1.2	UWB Multistatic Radar for LC surveillance area . . . . .	17
2.1	Possible physical interactions . . . . .	19
2.2	Image principle for reflection phenomena . . . . .	20
2.3	Diffraction law and Keller's cone . . . . .	21
2.4	Scenario created in RT simulator with obstacle . . . . .	24
2.5	Electromagnetic characteristics of materials . . . . .	25
2.6	Example of TX file . . . . .	25
2.7	Reflection vs Scattering . . . . .	27
2.8	Impinging rays in the RT scenario . . . . .	28
2.9	Induced current by rays in the receiver equivalent circuit . . . . .	29
3.1	Types of radio-over-fiber (RoF) communication systems . . . . .	32
3.2	Classic analogue RoF communication systems . . . . .	33
3.3	Inter-Modulation Distortion effect . . . . .	33
3.4	Block diagram of the receiving chain . . . . .	35
3.5	Example of computed behaviour of $W_{1,1}(t)$ . . . . .	37
4.1	UWB different configuration . . . . .	40
4.2	The pulse template in time domain . . . . .	42
4.3	Anti-intruder UWB multi-static radar system [1] . . . . .	43
4.4	AOA & convergence orbit of the intersection points [2] . . . . .	44
4.5	Measurement setup of the 2D circular track [3] . . . . .	45
4.6	Active sensors in FOS . . . . .	49
4.7	Path loss between nodes when obstacle is present . . . . .	50

5.1	Illuminated pixels with 4-sensor classic approach . . . . .	57
5.2	3D image metal box of $5.83 m^3$ in the middle. ASVC method . . . . .	58
5.3	3D image metal box of $5.83 m^3$ . Classic approach . . . . .	59
5.4	3D image metal box of $1 m^3$ in the corner. ASVC method . . . . .	59
5.5	3D image metal box of $1 m^3$ in the middle. ASVC method . . . . .	60
5.6	3D image metal box of $0.34 m^3$ in the middle. APVC method . . . . .	60
5.7	3D image metal box of $1.00 m^3$ with $S = 0.2$ . APVC method . . . . .	61
5.8	Error estimation of volume with cube of $1 m^3$ . . . . .	62
5.9	Error estimation of volume with cube of $0.34 m^3$ . . . . .	63
6.1	P410 RCM device with Broadspec antenna . . . . .	65
6.2	An example of prototype in the laboratory . . . . .	67
6.3	Mono-static prototype in the laboratory . . . . .	68
6.4	Mono-static measurement set up . . . . .	69
6.5	Clutter removal with the 3rd reference signal . . . . .	70
6.6	Clutter removal with 1st and 3rd reference signal . . . . .	71
6.7	Bi-static measurement set up . . . . .	73
6.8	Clutter removal with 1st and 3rd reference signal . . . . .	74
6.9	Clutter removal with 1st and 3rd reference signal . . . . .	74
6.10	Amplitude variation in 1st and 2nd reference signal . . . . .	76
6.11	Error in the Clutter removal with 1st and 2nd reference signal . . . . .	76
B.1	MRM Configuration screen with indication of the main areas . . . . .	87
B.2	MRM-RET Configuration Tab . . . . .	88
B.3	MRM RET Logfile Format . . . . .	89
B.4	CAT Configuration Tab showing settings . . . . .	90
B.5	Sample captured waveform showing potential radio lock spots [4] . . . . .	92

# List of Tables

1.1	Monitoring technologies comparison . . . . .	14
5.1	Volume derived after FOS algorithm . . . . .	61
5.2	Quantities utilized in the simulation of the <i>RoF</i> link . . . . .	62
5.3	Object volume estimation capabilities without clipping operation . .	63
6.1	P410 characteristics . . . . .	66
6.2	Transmission and reception by sensors . . . . .	75
B.1	Antenna Configuration . . . . .	91

# Preface

**Level Crossings** or **Railway Crossings** are those singular points where railways intersect public and/or private roads with the aim to separate the rail traffic from that of wheeled vehicles, and pedestrians. A Level crossing (LC) is always a dangerous point of the railway infrastructure, even when protection devices (barrier, red light and alarm) are adopted to ensure the LC closure, with respect to the wheeled and pedestrian traffic, before each oncoming train.

The mechanisms and design parameters constituting the protection of a LC are considered safe, since they are compliant with the national specifications. The risk determined by their presence is effectively mitigated and accepted by the "traffic code" (called "*Codice della Strada*" in Italy) which explains the behaviour that should be observed by people to avoid potential accidents or hazards.

When we talk about dangers of a LC people usually think about the damage potentially encounter by road users. Instead, we should keep in mind that also the train, with its passengers, might suffer of serious damages!

In the 2013, **Rete Ferroviaria Italiana** (R.F.I. S.p.A.) has proposed a national program to reduce global risks of LC accidents, through the implementation of preventative measures, compatible with the resources provided by the Government, in order to understand what are the most effective risk reduction methods.

The first step of the program was to take a census of the LC presence in the National Infrastructure from 1987 to 2013, as well as to analyse the effort made to suppress those placed on primary railway lines with high traffic and it falls in the "*PL suppression program*" initiated by *Ferrovie dello Stato* (FS) in the 80s. Further, all types of accidents were investigated according to various kinds of LCs, arguing that:

- *half-barriers* level crossings are the most vulnerable;
- *complete-barriers* level crossings have higher accident rate.

From these results it was evident that acting primarily on the last ones, a considerable reduction of global accident statistics is expected.

Suppression of all LCs is the most effective way to reduce the accident risk, however this is unfeasible for all the LCs in exercise, due to the costs and the time associated with civil works (flyover and underpasses).

In order to bring down the global accident risk the following actions were proposed:

- A. "PL Suppression program" continuation to eliminate the hazard;
- B. public education campaign to increase awareness of road users to LC risks;
- C. speed reducer bumps installation placed close to the LC to draw attention of drivers;
- D. new technological systems of *Integrated Automatic Protection (PAI-PL)*, to avoid obstacles trapped between rails (causing collisions);
- E. measures to mitigate the global accident risk increasing the existing road sign and the predisposition of safeguard zones in order to better fit the regulations.

Among all the proposed actions, particular attention has been focused on the solution number 4, "**PAI-PL**", which is considered the most reliable solution against the obstacles trapped within the railway crossing. The PAI-PL are integrated automatic protection systems (using microwave radar or lasers radar technologies) to detect the presence or absence of obstacles within the monitored area and set up green light protection signals of the LC.

Figure 1 shows the cost-effectiveness analysis of actions to reduce the accident risk. It is evident that PAI-PL has the best trade-off among all solutions proposed.

Starting from this in-depth analysis of cause-effect-possible feasible solution, R.F.I. S.p.A. called for help the major national Companies in monitoring and radar fields to find their own "*PAI-PL solutions*". The call was not limited to Companies but also Universities. In particular **Alma Mater Studiorum of Bologna** has submitted its solution, based on Ultra-Wide band technology, through a collaboration within a *PhD (Doctor of Philosophy)* program in *High Apprenticeship*.

The research of a feasible solution for monitoring a LC area is the core of this dissertation. All the steps followed in the project, the studied solutions and the implemented technologies will be explained in detail in this thesis.

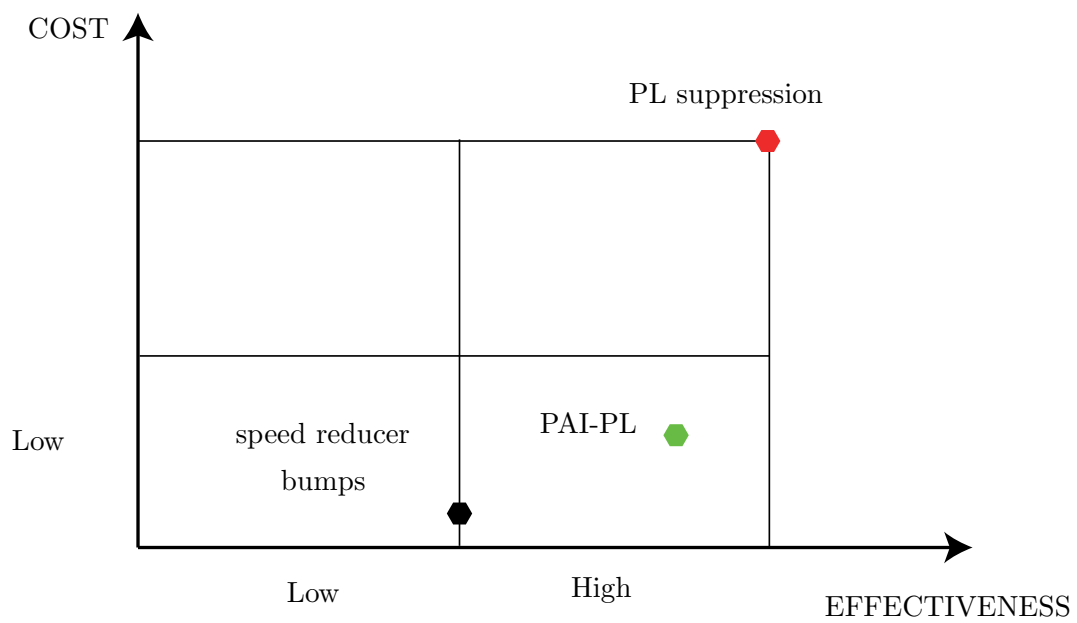


Figure 1: Cost-Effectiveness analysis of actions to reduce the accident risk.

# Introduction

Almost 50% of all train accident events caused by third parties take place in LCs, which are very difficult for the railway companies to control. In the US there are about 270 deaths per year at public and private grade crossings and nearly every 180 minutes someone is hit by a train [5]. The Federal Railroad Administration (FRA), through the efforts of its Highway-Rail Crossing and Trespasser Prevention Division, is committed to reduce that number. Trespassing along rail road rights-of-way is the leading cause of rail-related deaths in America. Nationally, more than 431 trespass fatalities occur each year, and nearly as many injuries, the vast majority of which are preventable. Federal funding for installing automatic warning devices and other improvements for public highway-rail crossings is managed by the Federal Highway Administration and commonly referred to as the Section 130 program.

In 2010 the European Railway Agency (ERA) disclosed the European benchmark in LC safety reporting 619 significant LC accidents resulting in 359 fatalities and 327 serious injuries. In EU LC accidents represents 27% of all significant railway accidents and 28% of all fatalities on railway, excluding suicides [6]. There are currently about 1.2 million LCs in the EU and, on average, there are five LCs per 10 line-km. Half of them are active LCs with some sort of user-side warning, while the remainders are passive LCs typically equipped only with the St. Andrew's cross traffic sign. A similar active/passive percentage (43%/57%) applies also to the reported 250/523 highway-rail grade crossings in the United States [5]. LCs with automatic user-side warning -typically flashing lights and sound- are the most common type of active crossings in Europe (38%), closely followed by the LCs with automatic user-side protection and warning (barriers with lights) (34%). The economic impact of fatalities and serious injuries in LC accidents was estimated in 350 million Euros in 2010 [6].

The European Community is currently devoting a great effort towards the achievement of an integrated European railway area, with the main intent to guarantee fast

and safe connection among the different European countries and cities. The goal is expected to be achieved by developing a high-performance network for freights and passengers, by promoting competition and creating incentives for innovation and quality of service. To this purpose, with the release of the first package of Technical Specifications for Interoperability (TSI) at the beginning of the 21th century, the European railway market opened to the *Trans-European Rail network*, which is divided in the Trans-European high-speed rail network and in the Trans-European conventional rail network, successively fused according to the 2008/57/CE directive. The aforementioned high-quality connection has to be obtained through the technical harmonization for interoperability of national and international services thus allowing the safe and uninterrupted movement of trains according to the target levels of performance.

The 2004/49 CE directive is oriented to promote the development and improvement of safety on EU Community's railways by harmonizing the regulatory structure in the member states.

The concepts of *common safety targets* and *common safety methods* have been here introduced to ensure that a high level of safety is maintained and possibly enhanced, and one of the most critical points is the protection of *LCs*, which is defined in the common safety indicator (CSI) of this directive. CSIs are based on common definitions and calculation methods. The data set is structured following significant accidents, deaths and serious injuries, economic impact of accidents, technical aspects (level crossings by type and automatic train protection systems) and management of safety [7]. In order to maximize the LC safety level while preserving a reliable and fast network, is then required to develop technical solutions complying with the EU safety requirements.

High safety requirements for LC have led to the development of surveillance systems matching EU regulation to eliminate unacceptable risk. As stated in the preface, among all possible feasible solutions, against LC accidents and to prevent collisions with trains caused by trapped obstacles (like vehicles) in the LC area, the most suitable countermeasure is making safer these singular points through the adoption of technological monitoring systems to control unauthorized access.

In Italy the National Railway Operator (R.F.I. S.p.a.) has identified two main systems to monitor the access in LC areas:

- A. *TV-PL* are television-based systems where a operator (stationmaster) controls on the monitor the presence or absence of obstacles before acting the LC

barriers closure;

- B. *PAI-PL* are systems integrated with railway signalling mechanisms, which automatically protect the LC area by preventing the train to pass through. PAI-PLs vary in different types depending on technology (microwave, radar, 3d laser, etc);

The PAI-PL ability to automatically handle the safety of the LCs without human decision, makes these systems the best solution to be directly integrated with existing signalling mechanisms and with faster barriers closing process, optimized with respect to the impact on road traffic.

R.F.I. S.p.A., to be compliant with the European standards, wrote a specification document in order to define a set of technical and functional requirements for PAI-PLs able to increase LCs safety.

This document not only defines the functional requirements that systems must satisfy in terms of obstacle dimension recognition (alarm for critical volume), robustness to weather conditions, and easy installation on existing infrastructures; but gives specific implementation constraints and steps that surveillance algorithms have to work out. In particular, it defines the required phases of detection as "scan period", the overall time in which the scan must be performed (from the complete closure of barriers to their re-opening) and "reference period" as the time from the instant of complete closure to when the PAI-PL decides that no obstacles are present. Moreover, it gives explicit indication of subsystems constituting the overall system:

- the first subsystem consists of the sensors dedicated to safely detection;
- data processing subsystem: securely processes the information mentioned above of the subsystem;
- interface subsystem with the signalling system.

## **Master-plan of the PhD activity**

The collaboration between R.F.I. S.p.A. and Alma Mater Studiorum of Bologna had the purpose to evaluate the feasibility and to investigate the main radar sensor technologies suited to be integrated with existing signalling systems in rail sites, with particular reference to the UWB technology. This activity has been supported by

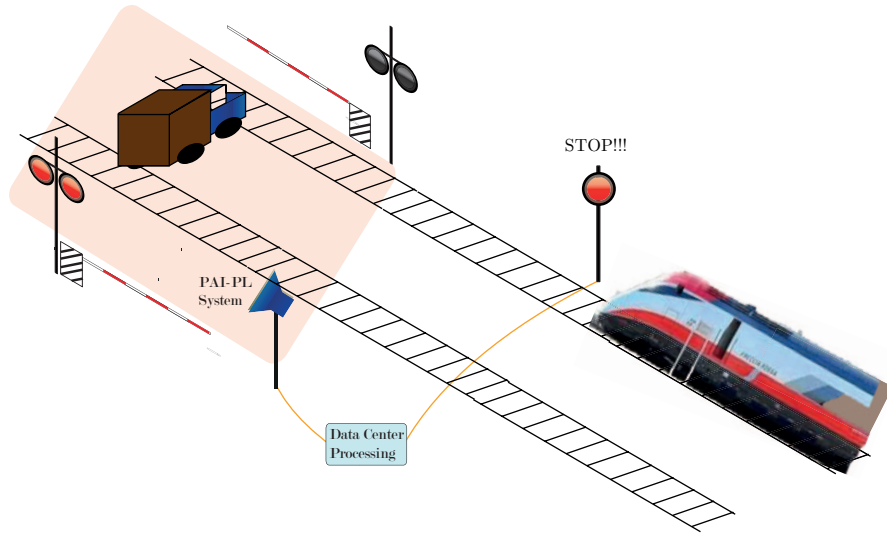


Figure 2: PAI-PL operational principle

a study of the UWB radio channel characteristics in a reference (LC-like) scenario, through ray tracing (RT) simulation. It was also studied, with the aid of computer simulations, the remote interconnection of several radars via fiber optic links (RoF), in order to concentrate in a single physical location all the signal processing operations and network control.

In particular, I have followed the master-plan below:

#### A. Preliminary study of the problem

- Identification and definition of functional requirements to best fit the PAI-PL specifications;
- With reference to the monitoring of level crossings, comparative analysis of technologies compliant with the requirements. Special attention was given to 3D laser radar technology and UWB;

#### B. Test of the UWB radar through simulation

- Simulation using RT of the backscattering characteristics of the UWB signal in a reference scenario (level crossing -like);
- Test of obstacle localization algorithms, using the results obtained in the previous step;
- Preliminary study and simulation of the transmission of signals through Optical Fiber;

### C. Validation in laboratory of the set-up prototype through measurement campaign

- set-up of a mono-static and bi-static measurement system, utilizing the Time Domain UWB commercial devices;
- Validation test.

The thesis is structured as follows. Chapter 1 introduces the main PAI-PL characteristics and requirements, with a brief state-of-the-art about the actual available technologies as well as an overview on their advantages and disadvantages (section 1.2). Chapter 2 explains the theoretical foundations of Ray-Tracing (RT) channel modelling, and describes how the RT simulator has been used to characterize the UWB channel in railway infrastructure scenarios. Chapter 3 describes the RoF technique by illustrating advantages and disadvantages of directly carrying UWB signals on the existing fiber-optic backbone to remote the post-processing operations. In chapter 4 the UWB technology is introduced with particular focus on multistatic radar systems as good candidates for LC protection. Here, starting from section 4.4, the fixed object scanner (FOS) algorithm is introduced. I introduce the mathematical model (section 4.4) of FOS and afterwards I derive the maximum likelihood (ML) approach which provides localization and volume estimation capability. In chapter 5 the simulation results provided by FOS algorithm are shown. Moreover, in section 5.3 a trade-off between the number of LCs which can be remotized through fiber optical link and the distance of the fusion center is derived. These results has convinced us to perform experimental measurements in the last PhD year to assess the performance of the FOS algorithm in realistic conditions. These efforts are reported in chapter 6. The set up of the prototype based on commercial UWB sensors and related software are also described. Experimental data have been collected both in mono-static and multi-static configuration and given in input to the FOS algorithm. Finally, conclusions about the work are drawn.

# Chapter 1

## Integrated Automatic Protection of LC (PAI-PL)

In this chapter I describe the main safety requirements which have to be respected in LC areas as well as the state of the art of current technologies adopted to guarantee the LC safety by discussing their advantages and limitations. The management of reliability, availability, maintainability and safety, denoted with the term RAMS is promoted in EN 50126 (CENELEC) regulation by defining common approaches. In the following, particular attention is given to Safety. Subsequently, in section 1.3 the system designed in the Thesis based on partial UWB multi-static radar is introduced.

### 1.1 Safety Requirements

Safety requirements and regulations are specific to each country and, in some cases, to single rail infrastructure operators, therefore in the following we use the European scenario as a reference.

Passive safety requirements for railway vehicles are defined in the Commission Decision UE 291/2011 (par. 4.2.2.5), and refer to all subsystems, comprising surveillance system for LC areas, which can operate independently from the railway infrastructure.

Passive safety is aimed at complementing active safety when all other measures have failed. This definition fits the LC scenario where, despite the automatic user-side warning as well as barrier closing, a road vehicle could be entrapped inside a LC generating an extremely dangerous situation that could lead to a collision with the

incoming train. Two reference collision cases are classified for LCs: the impact of the train with a *large obstacle* or with a *small obstacle*. The entrapped object of the first case is described in EN15227/2008 (Table 2, Sec. 5) and can be, for example, a heavy truck or a tank. In the second case the EU decision does not provide specific information about the smallest size of the obstacle. To fix a requirement, it is reasonable to consider the minimum size of a vehicle which must be detected inside the LC in order to generate an alarm. This can be approximated with a parallelepiped volume placed on the ground with dimension equal to  $2 \times 1.1 \times 1.3 \text{ m}^3$ . This dimension is slightly smaller than that of the smallest minicar available in the market. Under a conservative setting, the critical dimension for the performance assessment of different surveillance systems can be chosen equal to one cubic meter. Therefore one of the key performance parameter is the capability of the system to discriminate the volume of the obstacle (when present), as only obstacles larger than one cubic meter must generate an alarm with consequent stop of the train.

According to current EU regulations, LC surveillance systems must also satisfy functional requirements in terms of robustness to weather conditions, cost, and ease of installation on existing infrastructures, making their design challenging. In particular, the *tolerable hazard rate* is defined as a target measure of both systematic and unpredictable failure integrity. For instance, LC surveillance systems must guarantee a *false alarm rate* (i.e. the erroneous detection of obstacles when these are actually not present in the area) smaller than  $1.9 \cdot 10^{-4}$ , which is equivalent to one false alarm per year with a traffic of 20 trains per day. On the other hand, the *misdetection rate* (i.e. the missed detection of an obstacle when it is effectively present in the area) must be below  $10^{-8}$  [7]. Moreover, another important issue is the detection of steady obstacle in static environments, e.g. radar systems are designed to detect moving obstacles taking advantage from the Doppler effect. This adds a further degree of complexity to the system development.

In the following, we describe current possible solutions which aim to preserve safety in LC areas. Specifically, only systems that can be integrated with the railway infrastructure without human interaction will be considered here. As a consequence, other solutions such as those that rely on car speed reduction through bumpers, on traffic signals improvement, or on TV-based surveillance are out of the scope of this work.

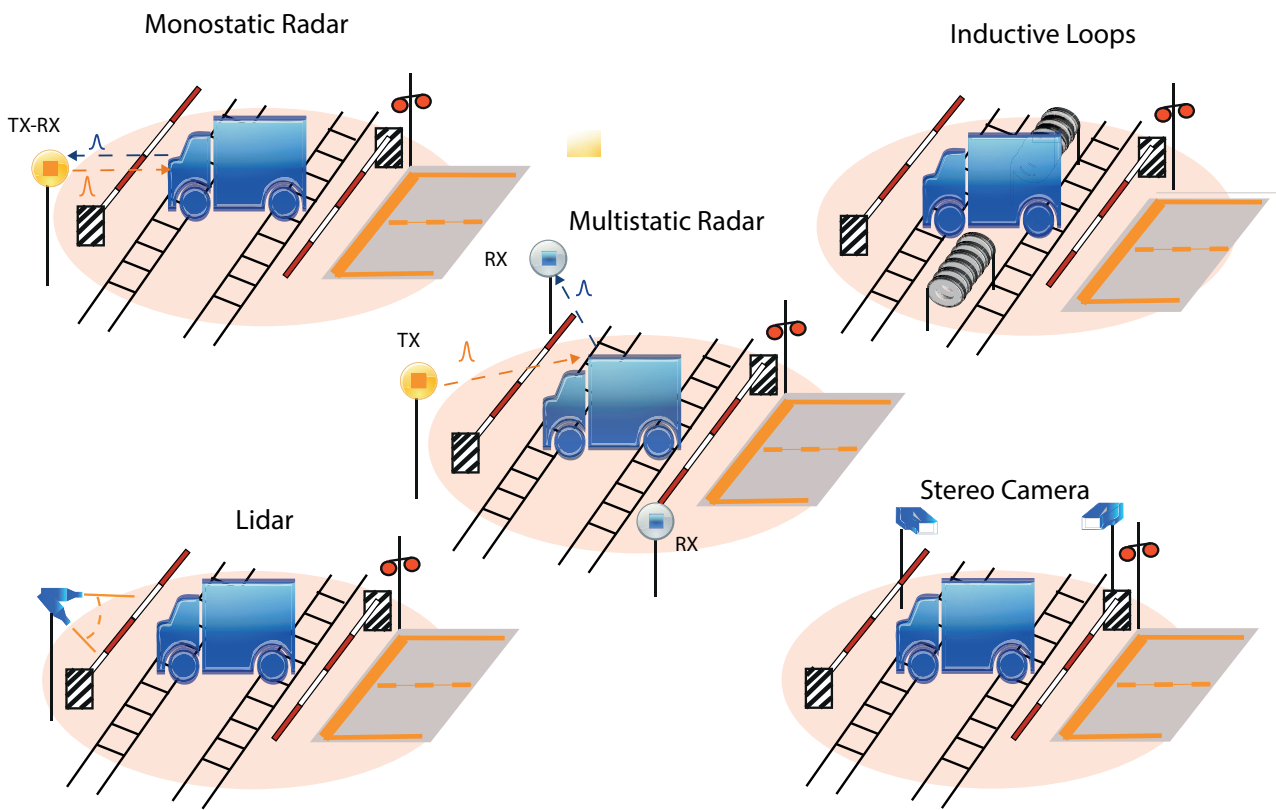


Figure 1.1: Different technologies available to detect the presence of an entrapped object inside the level crossing area

## 1.2 Surveillance Systems State of the Art

In recent years several systems have been proposed for LC surveillance, each supported by a different technology:

- Microwave/millimeter-wave Radar;
- Inductive Loops Detector
- Laser Imaging Detection and Ranging (LIDAR);
- Stereo Camera Detection.

The radar concept was born with microwave technology with the main intent to detect the presence of an intruder inside a monitored area. A key radar indicator is the radar cross section (RCS), which represents the projected area of a metal sphere that would scatter the same power in the same direction as the target does. Most of radar systems rely their capability in discriminating the dimension of the object on RCS estimate by analyzing the reflected signal (backscatter). Several operating frequency bands as well as radar architecture configurations have been exploited. For example, in [8], two UWB mono-static radars cover half-portion of the monitored area, respectively (see Fig. 1.1a). Each UWB radar detects obstacles in case they are present in its covered area portion by analyzing the backscattered signal to obtain only a rough approximation of the obstacle's size. Unfortunately the coverage area separation among sensors determines a low localization resolution and makes the system performance particularly sensitive to single sensor outage. In [9], the multiple-input multiple-output (MIMO) antenna array concept is developed for a frequency modulated continuous wave (FMCW) radar operating at 25 GHz. Even though the dimension of obstacle still relies on RCS, the MIMO configuration allows for a 2D angular resolution in azimuth.

With the liberalization and the possibility to use the Ka-band and higher bands (e.g. V-band), different systems exploit these new frequencies that are characterized by a low level of interference. In particular, [10] adopts FMCW at 36.5 GHz using up to 9 sensors, whereas [11] investigates a spread spectrum radar at 60 GHz using the correlation of pseudo-noise codes to detect the obstacle in distance and azimuth, respectively.

A common limitation of all these systems is that RCS is not a reliable indicator of the object's dimension as it strongly depends on object reflection characteristics and shape which are not known a priori. Moreover, since electromagnetic waves

propagation cannot be confined in a specific area, false alarms caused by objects located outside the LC area are possible. This is actually the main limitation of radio-based systems that can be mitigated only if high-accuracy localization capabilities are implemented, as detailed in Sec. 4.4.

The solution based on Inductive Loops [12] was among the first to be proposed. The loops are excited with signals whose frequencies range from 10 KHz to 50 KHz, and when a vehicle stops on or passes over, their inductance is decreased. Depending on the resonance frequency generated by the wire loop it is possible to identify specific metal portions of the vehicle. This system is very simple but extremely inaccurate in estimating obstacle's dimensions. The massive presence of metal in the railway causes problems in threshold setting and, additionally, wire loops are subjected to traffic stresses and temperature effects.

Another solution is represented by the LIDAR technology, which exploits ultraviolet, visible, or near infrared light to illuminate a target with a laser. Objects detection and 3D image reconstruction are based on the time-of-flight (TOF) of the electromagnetic wave. In [13], environment scanning is performed through a single-head 3D laser range finder which is tilted to create a 3D image of the scene, as shown in Fig. 1.1c. This technique is based on TOF estimate for different head tilts and on background subtraction approaches. As for the stereo camera solutions, several works have been published extracting 3D information from digital images by comparing the same scene taken from two advantageous locations.

A common problem of image detection methods is the static background estimation, which causes the necessity to detect and track incoming, staying or outgoing objects in the LC area, as investigated in [14], where the 3D localization is performed by hierarchical belief propagation algorithms. Differently, [15] assumes that the displacement of the image contents between two nearby instants (frames) is small and approximately constant within a neighborhood of the point under consideration. Thus the optical flow equation can be assumed to hold for all pixels within a window centered at that point.

The main characteristics of current technologies are summarized in Table 1.1, where it can be noted that present microwave and millimeter-wave solutions do not provide any or only rough information about the obstacle volume and position. On the other side, the solutions based on image detection, while exhibiting very high resolution in obstacle shape detection, might suffer from image degradation when working in non-optimal weather conditions. In table 1.1 the different solutions are

Table 1.1: Comparison between the characteristics of different monitoring technologies.

Technology	System Architecture	Dimension Estimation	Localization Capability	Heavy Rain	Dense Fog	Cost Range
<i>Mono-static radar</i>	two sensors [8]	RCS estimation	none	reliable	reliable	low
<i>Ka-band radar</i>	independent multiple sensors [10]	RCS estimation	none	reliable	reliable	Medium
<i>V-band radar</i>	antenna array [11]	RCS estimation	approximated 2D localization	reliable	reliable	Medium
<i>MIMO radar</i>	antenna array [9]	RCS estimation	approximated 2D localization	reliable	reliable	Medium
<i>FOS radar</i>	multiple sensors [16]	good resolution	good 3D localization	reliable	reliable	Medium
<i>Inductive loops</i>	multiple buried turns [12]	low resolution	none	reliable	reliable	Low
<i>LIDAR</i>	single head [13]	high resolution	high 3D localization	blind spot	unreliable, image degradation	High
<i>Stereo Camera</i>	single head [14, 15]	high resolution	high 3D localization	unreliable, image degradation	unreliable, image degradation	High

compared also in terms of cost of the technological apparatus. We must point out that other related costs, such as those site-specific deriving from the installation of the supporting infrastructure, might have a determinant impact and can be hardly generalized. Similar considerations apply to other related costs, like the ones related to works on the railway infrastructure, which depend on particular aspects which are characteristic of each LC.

Another important parameter is the maintainability, which falls into the so called management of RAMS (reliability, availability, maintainability and safety). One of the figures of merit defined in the EN-50126 European Standard for Railway Applications, adopted also by other international projects like the California High Speed Train (CHSTP), is the mean down time (MDT), which is the average time when a system is not operational. All the considered systems exhibit a degree of quantifiable self-imposed down time for periodical calibration. However, the times related to repairing, corrective and preventive maintenance, and logistic or administrative

delays depend again on the individual instance considered, and therefore a general comparison in terms of MDT has not been included in Table 1.1.

## 1.3 UWB Radar Overview

### 1.3.1 Ultra Wideband Technology

A promising wireless technique for position location and object identification in short range environments, constituted by radio sensor networks, is UWB technology. A signal is classified UWB by the Federal Communications Commission (FCC) if it has either a bandwidth larger than 500 *MHz* or a fractional bandwidth greater than 0.2 [17]. Their fundamental advantage comes from their huge bandwidth which may be up to several *GHz* depending on the national regulation rules and can be seen as the transmission of (sub-)nanosecond duration pulse. The allowed power spectral density (PSD) by the FCC is under  $-41.3$  *dBm/MHz*

Consequently, UWB sensor networks offer an extraordinary resolution and localization precision of passive objects in short range distance. Moreover, with the lower frequencies involved in the UWB spectrum, it becomes feasible to look into or through non-metallic materials and objects as it is done in through-wall/ground detection. Other remarkable advantages of UWB include, but are not limited to, low-power consumption (battery life), extremely accurate (centimetric) ranging and positioning also in indoor environments, robustness to multipath, low probability to be intercepted (security), large number of devices operating and coexisting in small areas, robustness to narrowband jamming [17].

Despite the excellent range resolution capabilities of UWB radar sensors, detection and localization performance can be significantly improved by cooperation between spatially distributed nodes of a sensor network. This allows robust detection and localisation even in case of partially non-line-of-sight (NLOS) minimizing the false alarm probability due to obstacles outside the monitored area. In fact, the position of the generic TX-RX pair in a bi-static configuration represent the foci of an ellipse (see Fig.4.1) within which, if present, obstacles can be detected and not otherwise. In addition, distributed observation also allows identification of certain features of objects such as shape (take a rough picture or images), dynamic parameters and time variant behaviour [1].

### 1.3.2 UWB Partial multi-static Radar: Overview

In this thesis, I have exploited both features to reduce false alarm detection namely the extraordinary localization precision and the imaging capabilities of cooperative multistatic radars. In the next chapter, a UWB partial multi-static radar for railway crossings surveillance capable of detecting, localizing and estimating the obstacle volume, even in static conditions, is presented and studied. It makes use of a fixed set of UWB nodes to obtain the information about the volume of the obstacle thus discriminating between large or small obstacles (see Fig. 1.2). The proposed system, namely FOS [16], performs a sequence of scanning phases where only suitable subsets of nodes participate to the measurement of the environment response (backscatter) to the UWB interrogation signals emitted by the nodes themselves. All measurements are successively collected by a fusion node responsible for taking an overall decision on the event. To reduce the number of level crossings to be monitored by a given fusion center, an interesting opportunity is to connect the sensors and the fusion center through fiber optic links. Within this perspective, the possibility to exploit the UWB-over-Fiber technology is under investigation [18]. Note that FOS can be considered as an hybrid approach combining the UWB multi-static radar and the mono-static imaging scanner configurations. As a consequence, it allows for gaining some of the advantages of both configurations and mitigating their drawbacks. Indeed, it overcomes the limitations of optical based systems [13, 14] and, at the same time, offers good obstacle detection and localization performance inside the level crossing.

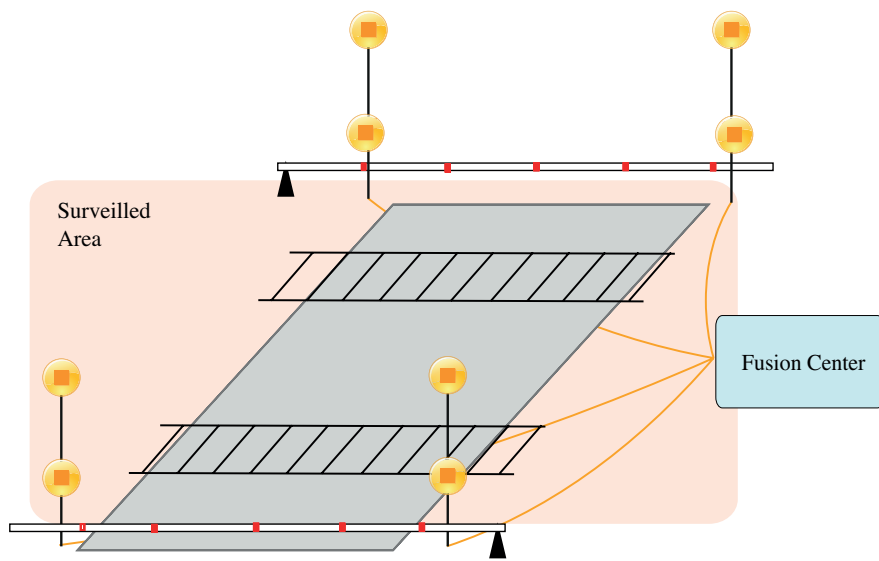


Figure 1.2: UWB Multistatic Radar for LC surveillance area

## Chapter 2

# Ray-Tracing

To evaluate properties of obstacles backscattering to be detected in a Ultra-Wide Band frequency range, it was necessary to make a preliminary analysis of the wireless channel to a scenario like LC. Propagation in a real environment is more complex than in free-space condition describes by the simple Friis formula. Real scenarios generates *multi-path propagation* that must be properly characterized in order to better design a communication system.

The multi-path creates different replicas of the propagated wave between transmitters and receivers due to the scenario complexity as we can see in Fig. 2.1. Each of these waves arrive at receivers with a different time-of-arrival (TOA), direction of arrival (DOA) and phase-shift depending on the possible physical interactions of waves with scenario:

- A. *reflection*, when a incident wave impinging a surface creating a reflected wave and refracted one that depends on the electromagnetic object characteristics in a neighbourhood of the reflection point.
- B. *diffraction*, is the wave interaction with obstacles which have dimensions of order of  $\lambda$  and generally this effect is considerable when waves impinging edges and/or vertices (corners).
- C. *diffuse scattering*, due to non homogeneous materials and the surface roughness resulting in a distribution of the scattered power in all directions and not only in the specular one; this phenomenon will be better discussed next.

In this chapter will be introduced the main characteristics of the RT channel model used to characterize the UWB channel in the LC scenario will be introduced.

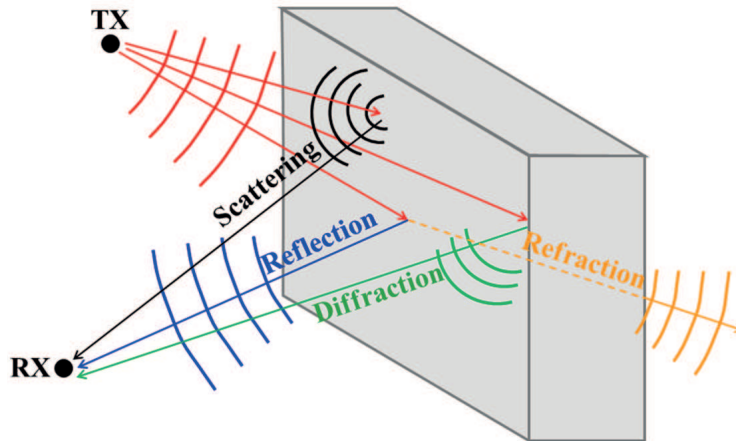


Figure 2.1: Possible physical interactions

## 2.1 Introduction to Ray-Tracing

Ray-Tracing is a deterministic propagation model based on the geometric theory of propagation (GTP) [19]. Since the electric field produced by a point source propagates in free space as a spherical wave, in the far-field region these waves can be considered as plane waves (locally), and thus represented geometrically as rays that come from the transmitter to the receiver (with trajectories such as to minimize the path).

The simulator involves the computation of rays that connect the two terminals through the free space and through interactions with the environment. More precisely, reflection, refraction, diffraction and diffuse scattering represent the interaction mechanisms that are processed by the construction of a tree, also called *visibility tree*. Specifying the maximum number of interactions that a ray may undergo, or according to a minimum power threshold for a ray to be propagated, a branch of the tree can be inserted or discarded.

The advantage of RT is a better accuracy of the results compared to empirical or statistical models. On the other hand, being a site-specific model, the drawbacks in its use are:

- the need for a detailed database of the scenario:
- the higher computational cost than other simple models.

Evaluation of visibility/obstruction tree is the most computationally intensive part of the algorithm. Moreover, additional effort can be required if an UWB characterization is needed since simulation are repeated several times for each frequency,

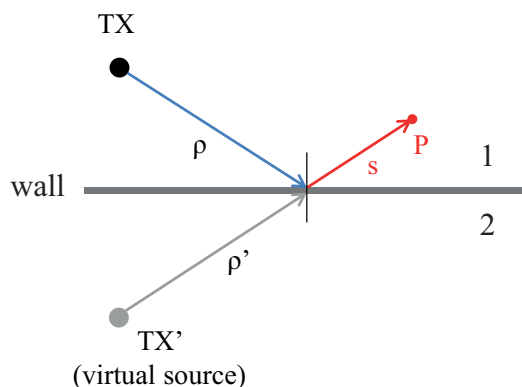


Figure 2.2: Image principle for reflection phenomena

depending on the considered bandwidth. Nevertheless, with the advent of new more performing computers, adopting proper speed-up techniques and CPU/GPU parallelization the computational cost has become a less critical problem.

Ray-Tracing works by step:

- A. Evaluation of level visibility from TX or Virtual TX.
- B. Application of interaction coefficients and generation of new Virtual TXs, in an iterative way. RT takes into account specular reflection (as explained in section 2.1.1), transmission (if obstacles are penetrable), diffraction and diffuse scattering (as shown in section 2.1.2).
- C. Field computation.

In the next section, 2.2, will be explained more in detail what are the input data needed by the RT simulator.

### 2.1.1 Reflection, Refraction and diffraction

The deterministic algorithm considers first of all the possible reflections and refractions through the region of visibility created after every interaction thanks to an iterative process that exploits the theory of images. Intuitively, given a real transmitter  $TX$  the algorithm creates its image (virtual transmitter,  $TX'$ ) with respect to the wall 1, the image of  $TX'$  with respect to the wall 2 ( $TX''$ ), and so on until reaching the receiver (see Fig. 2.2).

Regarding diffractions, however, the region of visibility is detectable by analyzing directions taken by various rays that are created, which lie on the surface identified by the so-called *Keller's cone* (see Fig. 2.3).

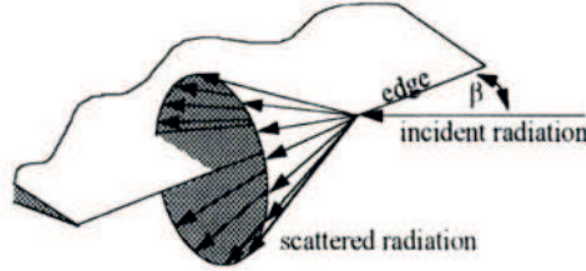


Figure 2.3: Diffraction law and Keller's cone

### 2.1.2 Diffuse Scattering

RT takes into account the effect of diffuse scattering modelled through the (heuristic) Effective Roughness (ER) approach. One of the main parameters of the ER model is the scattering parameter ( $S$ ), which accounts for the amount of the incident power diffused in all the directions at the expenses of specular reflection, due to the presence of surface and volume irregularities. The power of the rays which undergo specular reflection is correspondently decreased through the factor  $R = \sqrt{(1 - S^2)}$ , in order to satisfy the overall power balance.

The incidence point becomes a secondary source of rays which propagates in all directions to the outer surface of the obstacle. The scattering power distribution can be described by the following scattering pattern models in the backward semi-space [20, 21]:

- A. *Lambertian* model;
- B. *Single-lobe Directive* model;
- C. *Backscattering Lobe* model.

The first model follows the Lambert's law in which the beam is diffused in all directions, with an intensity that decreases according to the cosine from the normal to the surface, so independent of the angle of incidence of the incident ray. In this case, the intensity of the scattering beam is directly proportional to the cosine of the angle between the normal and the direction of the beam itself:

$$|\bar{E}_S|^2 = E_{S0}^2 \cdot \cos(\theta_S) \quad (2.1)$$

where  $\bar{E}_S$  is the intensity of the scattered field, which is evaluated according to a proper scattering coefficient  $S$  ([20]). From 2.1 follows that the *scattering radiation*

*lobe* is assumed to have its maximum,  $\bar{E}_{S0}$ , in the direction perpendicular to the wall.

The directive approach is based on the assumption that the scattering lobe is steered towards the reflected direction in case of single-lobe. The expression of this model for  $0 \leq \theta \leq \pi/2$ , so for the backward half-space (the same half space where specular reflection takes place) is [20]:

$$|\bar{E}_S|^2 = E_{S0}^2 \cdot \left( \frac{1 + \cos(\psi_R)}{2} \right)^{\alpha_R}, \quad \alpha_R = 1, 2, \dots, N \quad (2.2)$$

where  $\psi_R$  is the angle between the direction of the reflected wave and the scattering direction and the exponent  $\alpha_R$  is related to the width of the scattering lobe (i.e., the model directivity). It is evident that the maximum is for  $\psi_R = 0$  (i.e., in the direction of reflection); moreover, the greater  $\alpha_R$ , the narrower the scattering lobe.

The third model, Backscattering Lobe, is similar to the directive single-lobe model, but it includes an additional term accounting for backscattering phenomena; therefore diffuse scattering can originate non negligible contributions even in the proximity of the incident ray, but with opposite direction. A scattering lobe in the incident direction is introduced [20]:

$$|\bar{E}_S|^2 = E_{S0}^2 \cdot \left[ \Lambda \left( \frac{1 + \cos(\psi_R)}{2} \right)^{\alpha_R} + (1 - \Lambda) \left( \frac{1 + \cos(\psi_i)}{2} \right)^{\alpha_i} \right], \quad \alpha_R, \alpha_i = 1, 2, \dots, N; \Lambda \in [0, 1] \quad (2.3)$$

where  $\alpha_i$ , determine the width of the back-lobe and  $\Lambda$  is the repartition factor between the amplitude of the two lobes.  $\alpha_i$  and  $\alpha_R$  have the same meaning as in the previous model (if  $\alpha_i$  or  $\alpha_R$  increase, the width of the respective lobe decrease).  $\Lambda$  can vary in the range  $[0,1]$ , and for  $\Lambda = 1$  the model reduces to the single-lobe model seen above.

To further extend the model to the transmission half-space, the so called *forward, through-wall diffuse scattering* has been introduced. Two scattering lobes are added, the first in opposite direction w.r.t. the reflected beam in the first half-space and the second is around the transmission direction, which is the direction of the incident ray forwarded through the obstacle. For example in directive approach to consider the transmitted intensity in the second half-space the equation 2.2 must be extended as made in [21] for  $\pi/2 \leq \theta \leq \pi$ :

$$|\bar{E}_S|^2 = E_{S0}^2 \cdot \left( \frac{1 + \cos(\psi_T)}{2} \right)^{\alpha_T}, \quad \alpha_T = 1, 2, \dots, N \quad (2.4)$$

where  $\psi_T$  is the angle of the scattering direction with respect to the transmitted ray, and  $\alpha_T$  is a parameter related to the width of the forward scattering lobe. A different scattering parameter ( $S_T$ ) can also be considered in the forward half space, with respect to the one used in the backward half space (called  $S$  or  $S_R$ )

## 2.2 3D Scat RT Simulator

Here, the 3D ray tracing software described in [20] is introduced. In addition to specular reflection and edge/corner diffraction modelled through geometrical optics (GO) and uniform theory of diffraction (UTD), the RT tool takes into account the effect of diffuse scattering, modelled through the ER approach. A correct use of the program requires essentially to know the data format to give in input and to understand the results produced as the output. There is also a series (rather large) of "flags" and parameters which allow to control and to vary (within certain limits) the operation of the program. In the following, the main input data and files needed to simulate and characterize the UWB channel in the reference LC-like scenario are described.

### 2.2.1 Input files

As said, the RT model requires a detailed description of the environment, which must include

- the coordinates, the thickness and the type of each element (wall, rail, metal obstacles etc...);
- if present also the coordinates of any "holes" and discontinuities (mainly in indoor case, e.g. doors, windows, etc...);
- a list of edges where diffraction is enabled.

To provide a suitable set of scenarios to test FOS algorithm several "realizations" of the input database have been created. Each database is constituted by the empty reference scenario and by the obstacle placed in a random location, as shown in Fig. 2.4.

An example of a geometrical description of the empty reference scenario is reported in Appendix A.1 to better understand how input files made.

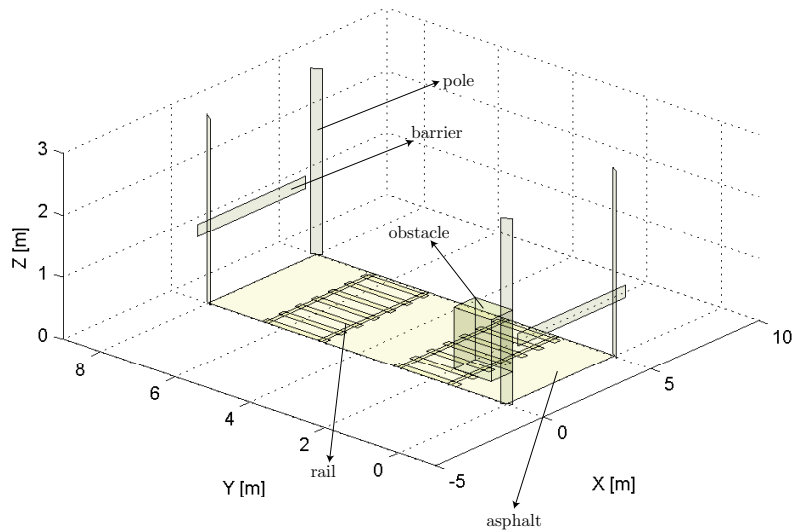


Figure 2.4: Scenario created in RT simulator with obstacle

In addition to the geometrical description, the different characteristic of the materials which compose the scenario must be listed in a specific separate file, which indicates:

- the thickness;
- the relative permittivity and the conductivity  $\sigma$  (expressed in *Siemens/m*);
- If the material is penetrable or not;
- if the object is able to reflect from both of its sides.

A file example of Electromagnetic characteristic materials is reported below, Fig. 2.5, to better understand.

### 2.2.2 Transmitter and Receiver files

These two files describe the characteristics of Transmitters and receivers (e.g. their location, antenna radiation properties, and other information). In particular, for the TX the file includes the location in Cartesian coordinates, the frequency, the transmitted power (expressed in dB-Units), and the name of the file that describes the polarization and the radiation characteristics of the antenna. Finally, three rotation angles are used to specify the orientation of the main lobe of the antenna

---

```

;tipo      eps      sigma      thick      bilat      attravers
"wall"     4.9998      0.0        0.0        .true.     .false.
"asphalt"  3.7054           0.0        0.1        .true.     .true.
"rail"    0.00 8.e6 0.005 .true. .true.
"poles"   0.00 8.e6 0.0 .true. .false.
"metal_obstacle" 0.00 8.e6 0.0 .true. .false.
"sbarre_legno" 1.60 0.00 0.15 .true. .true.
"traverse_cemento" 4.9998      0.0        0.1        .true.     .true.

```

---

Figure 2.5: Electromagnetic characteristics of materials

---

```

Position:      0      0      3.01
Power:         50      dBW
Frequency:     4300      MHz
Radiation File:      input\antennas\UWB_ISOTROPA_theta.ant
Angle 1:       0
Angle 2:       0
Angle 3:       0

```

---

Figure 2.6: Example of TX file

with respect to the Cartesian axes (in  $z$ ,  $y$ ,  $x$ -order). In the example 2.6 we can see an extract of this file for TX. In the considered reference environment, TX antennas are placed (more precisely a TX-RX pair for each sensor) are placed at the corner of the monitored area at different heights to be compliant with the requirement of not easy access to the surveillance system. In the showed case the antenna is positioned in the first corner of the LC area at the height of 3 meters.

The antenna file describes polarization and radiation properties of the antenna, referred to  $\theta$  and  $\phi$  coordinates (spherical reference system). In particular, we have to specify the antenna gain in the maximum direction and then describe the radiation pattern ( $E_\theta$ ,  $E_\phi$  field component for each direction). All this is repeated for each frequency of interest as in UWB case (not shown here for brevity).

### 2.2.3 Run parameters

To set up the simulation we need to specify some additional input parameters (set in a separated file). First of all, the maximum number of interactions has to be specified together with the size of *scattering tiles* (whose meaning is explained later) in order to manage the computational complexity of the simulation. Moreover, other many options on the scattering control are provided, including:

- enable the coherent scattering (i.e., giving a random phase to the scattering rays and considering the constructive and destructive interference caused by different ray phases);
- enable scattering at transmitter or receiver side;
- discretization of  $\theta$  and  $\phi$  coordinates (related to the size of the scattering tiles and computation of scattering points);
- maximum number of combinations of reflection (or diffraction) with diffuse scattering in the same ray;
- parameter of the ER scattering model (e.g. scattering parameter  $S$ , lobe directivity  $\alpha$ , etc.).

An example of auxiliary parameter used during simulation in the run time file is shown in Appendix A.2.

### 2.2.4 Output

Once the simulation has performed based on the data implemented in the input files, the 3D RT generates the output file containing all the information about the propagation channel, in terms of rays. For each ray traced by the algorithm the output file describes the geometry (ray trajectory, DOA, delay, etc..) and contains the electromagnetic characteristics (received field components, power, etc...). For example, arrival and departure angles (AoA and AoD) refer to angles between a reference direction and the unit vector from RX (TX) towards the last (first) interaction point. In particular, the ray is described by the following angles (in radians):

- A.  $\phi$  (azimut) is the angle between x-axis and the projection of the segment in x-y plane ( $[-\pi, \pi]$ );
- B.  $\theta$  (elevation) is the angle between the x-y plane and the segment direction that identifies the ray ( $[-\pi/2, \pi/2]$ );

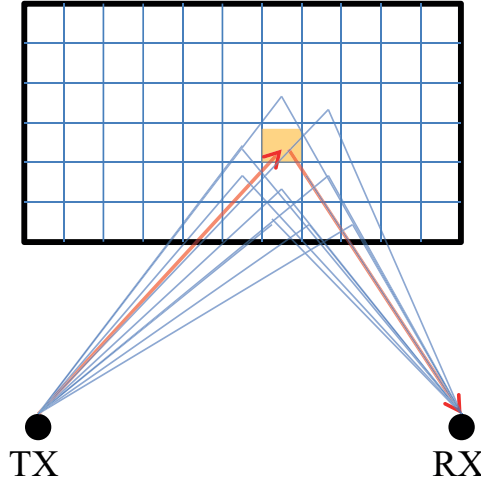


Figure 2.7: Reflection as local phenomenon vs. scattering as a distributed process

Each incident ray produces just a single reflected ray and on the contrary an infinite number of scattered rays. Therefore, the reflected contributions arriving at the receiver in a multipath, real environment are affected only by the electrical and geometrical properties of the corresponding obstacles in the immediate neighborhood of the obstacle points (see fig. 2.7). On the contrary, the overall scattered field at the receiver due to a scattering surface is the superimposition of the multitude of scattered contributions produced by all the infinitesimal surface elements  $dS$  visible from the RX (see fig. 2.7), i.e. it depends on the geometrical and electrical properties of the whole surface. In short, reflection, refraction and diffraction are "local" phenomena, whereas diffuse scattering is a "distributed" process.

For this reason, embedding diffuse scattering into a ER model can strongly increase the computation time, since the number of rays to be tracked dramatically increases. In this regard, the 3D Scat RT simulator can set "scattering tiles" discretization by launching scattering rays from the TX (or RX) towards the objects according to a proper angular discretization in  $\theta$  and  $\phi$ .

In Figure 2.8 it is possible to see the plotted rays (in blue) as the result of a RT simulation derived from the output files. A proper discretization in elevation and azimuth (in this case  $SCAT\_N\_THETA = 10$  and  $SCAT\_N\_PHI = 20$  with only one transmitting sensor is considered for scattering rays to better distinguish each ray interaction).

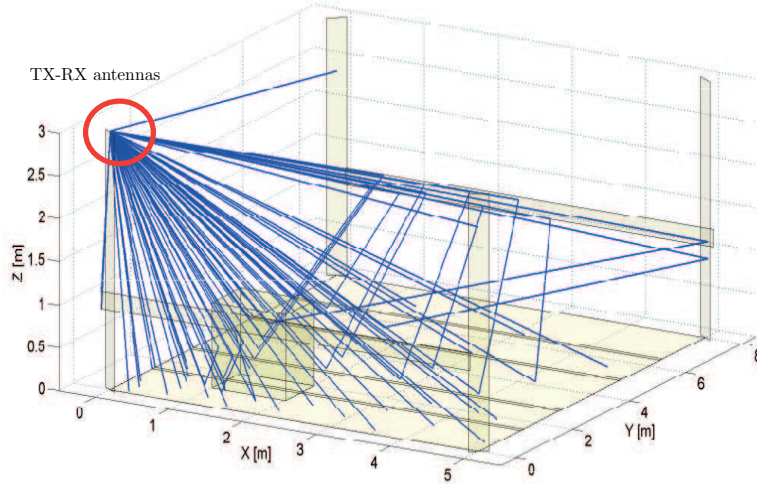


Figure 2.8: Impinging rays in the scenario plotted as the result of RT simulation

### 2.3 Post Processing and Transfer Function Computation for PAI-PL Scenario

In order to compute the required UWB channel characterization in the level crossing scenario in the post-processing, the output data are used to build the relative transfer function ( $H(f)$ ).

The transfer function is computed taking into account the power amplitude contribution  $\rho_i$  of all the rays ( $N_{rays}$ ) falling into the considered time interval and multiplied by the phase component corresponding to the considered frequency. To perform UWB characterization this computation is repeated for each frequency in the considered band (2.5) as,

$$H(f) = \sum_{i=1}^{N_{rays}} \rho_i \cdot e^{j(\theta_i - 2\pi(f_c + f)t_i)} \quad (2.5)$$

where  $\theta_i$  is the phase introduced by interactions and  $t_i$  the propagation delay.

In particular, under the assumption of perfect matching between RX antenna and receiver the received power [19] (square of  $\rho_i$ ) can be expressed as,

$$P_R = \frac{I_C^2}{8G_{in}} = \frac{\lambda^2}{8\pi\eta} \cdot g_R(\theta, \phi) \left| \vec{p}_R \cdot \vec{E} \right| \quad (2.6)$$

where  $G_{in}$  is the input conductance and  $I_C$  represents the complex induced current by rays in the receiver equivalent circuit (see Fig. 2.9) computed as,

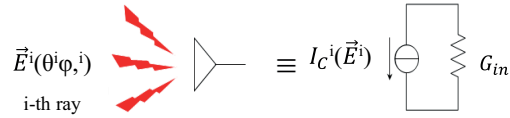


Figure 2.9: Scheme of the Rx antenna and complex signal-amplitude at the Rx induced by incoming rays

$$I_C^i = -j\lambda \sqrt{\frac{G_{in}g_R(\theta^i, \phi^i)}{\pi\eta}} \vec{p}_R(\theta^i, \phi^i) \cdot \vec{E}^i \quad (2.7)$$

Finally, in the phase introduced by interactions an additional term is added to take into account the propagation delay related to the product between phase constant and total length of the path of the ray.

$$\theta_i = \arg(I_{C_i}) + \beta \cdot r_i \quad (2.8)$$

Here after, we can see the script draw to compute the transfer function for each TX-RX pair.

```
% .....
% RUN EXECUTION DRAW

% Compute the overall H(f):

% parameters
band = 3000;      % 1GHz
tstep=1e-5;      % normalized at microsec
t_max = 0.07;    % in micorsecond
band_GHz = [ f0/1e3 - (band/1e3)/2 : 1000/1e6 : f0/1e3 + (band/1e3)/2];

% computation
for index_rx = 1:pars.RX_number
    % For each RX the H(f) is computing depending on the selected TX
    for index_tx = 1:pars.TX_number

        [abs_H arg_H] = ...
```

```

TransferFunction(Receiver,index_rx,1,index_tx,t_max,1000,'c', power, f0,
    band, 1000);

    received_signal(index_rx, index_tx).TF = abs_H .* exp(1i.*arg_H);
end
end

% overall H(f)
%H_tot = abs_H_tot .* exp(1i.*arg_H_tot);

% .....

```

The `TransferFunction` called, as explained before, computes the power amplitude of the arrival rays in the `tstep` ( $t_i$ ):

```

if(strcmp(coherent_flag,'C') || strcmp(coherent_flag,'c'))
for i=1:dim
PDP_lin(i,1)=PDP_lin(i,1)+abs(Icomplex(i,1))*abs(Icomplex(i,1))/8+abs(
    Icomplex2(i,1))*abs(Icomplex2(i,1))/8;
end
end
amplitude=sqrt(PDP_lin./TX_Power);

```

After, the phase is take into account depending on delays as in Eq. 2.8:

```

for i=1:dim
r_i=3.e2*((i-1)*tstep+min_delay);
phase(i,1)=angle(Icomplex(i,1))+beta0*r_i;
end

```

where  $r_i$  is the length of the path of the  $i$ -th ray and  $\text{angle}(I_{\text{complex}}(i,1))$  is equal to  $\text{arg}(I_{C_i})$  and  $\text{beta0}$  represents the constant phase.

## Chapter 3

# Radio-over-Fiber

radio-over-fiber (RoF) technologies combine both the high capacity transport of fiber optics and the flexibility of wireless access. The basic idea is to use the optical fiber as a transparent channel, capable to transport all kinds of signals and services in a broadband wired and wireless convergence scenario. At the same time, UWB has attracted growing attention due to its promising capabilities to provide high resolution with low cost and low power consumption in surveillance systems, as shown in section 4.2. In this chapter, we introduce the basis for a feasibility study of UWB-over-fiber (UWBoF) systems to improve the safety of rail crossing surveillance areas in case of entrapped vehicles providing location and volume information about obstacles. Two UWBoF solutions will be here introduced, which combine proper processing of UWB signal and backhauling over the already deployed optical fiber backbone. The performance of both structures will then be studied in Section 5.3. This will allow to identify promising architectures for the enhancement of level crossings safety. Before starting to explain the UWBoF techniques adopted in the PAI-PL context, we introduce the state of the art of RoF systems.

### 3.1 State-of-the-art of RoF systems

With the advent of popular bandwidth services such as HD video or on-line gaming, wireless systems require higher data speeds in order to enable the delivery of such services to the increasing number of users. High data rate communication systems optical fiber (*Gbit/s*) has already become the dominant mode of transmission due to its enormous bandwidth and low loss. RoF guarantees the seamless integration of optical and wireless communication systems [22]. The major factors that makes

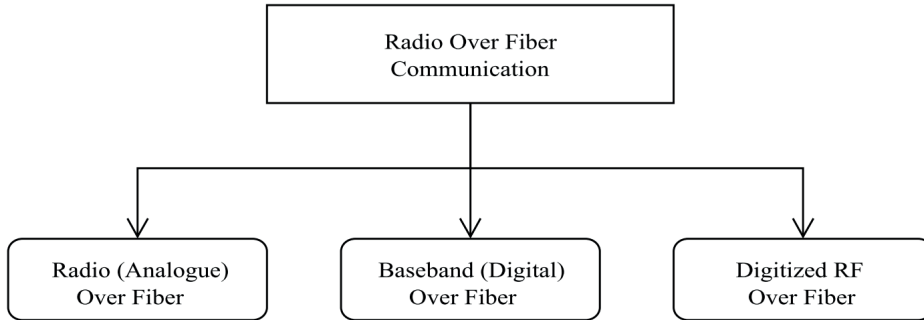


Figure 3.1: Types of RoF communication systems

RoF suitable are its transparency to the type of RF signal being transported, the large available bandwidth of fiber and its low attenuation.

There are three main types of RoF communication systems, namely *analogue* RoF, *baseband* RoF and *digitized* RoF as depicted in figure 3.1. In the baseband RoF the digital baseband data is directly transmitted over the fiber after electronic to optical conversion. These systems generally transmit optical pulses that have a Gaussian time-domain profile associated with the most compact spectrum for transmitting baseband digital data. Analogue RoF communications systems transmit the RF signal "as it is" over the fiber using an optical carrier as shown in figure 3.2. Finally, the digitized RoF communication involves the digitization of the analogue RF signal before transmission over the fiber. The analogue RF signal is converted to a series of bits through an analog-to-digital converter (ADC) and after electronic to optical conversion, it is transmitted over the fiber.

The Analogue RoF is a suitable candidate to transport UWB signals, i.e. radio transmission over a shared optical media fibre, in a rapid and cost-effective way extending the UWB radio range to in-home, in-building or even wide area applications. Two major UWB implementations are mainstream nowadays: orthogonal frequency division multiplexing (OFDM)-based and impulse radio. The compared performance of the two UWB implementations along different optical access fibre links demonstrate the feasible distribution of 1.25 *Gbit/s* UWB signals achieving bit error rate (BER) operation of  $10^{-9}$  at 50 *km* with both impulse radio UWB (IR-UWB) and OFDM-UWB implementations where impulse-radio UWB is more affected by the frequency response of the electrical devices [23].

In the next section (3.2) we discuss the use of analogue communication system through UWBoF techniques in the [3.1 – 10.6] *GHz* band for the application of

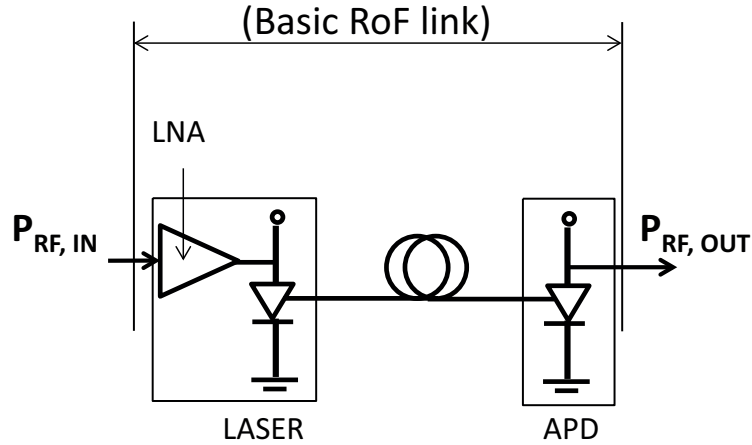


Figure 3.2: Classic analogue RoF communication systems

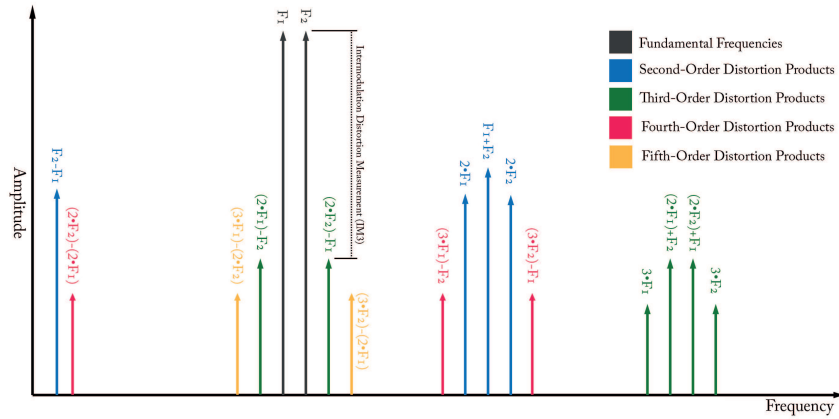


Figure 3.3: Inter-Modulation Distortion effect

PAI-PL surveillance system [18].

### 3.1.1 Impairments in Analogue ROF Systems

Before starting to describe the UWB fiber solution in railway scenario, some of the major causes of impairments on the received optical signal are introduced, which can be summarized as follows:

- **Chirp Effect.** Unwanted frequency modulation of the optical carrier related to its amplitude modulation. This effect is mainly generated when the laser is directly modulated, and, combined with the chromatic dispersion of the optical

fiber, creates unwanted additional harmonics in the spectrum of the received signal.

- **Laser Noise** Lasers generate noise which is commonly referred to as *Relative Intensity Noise (RIN)* representing the noise due to variations in the intensity of the laser light.
- **Non-linearities of the optical device.** When the RF signal enters into a modulator (which in the case of direct modulation coincides with the laser device), spurious spectral components are generated due to the modulator's non-linearity. This effect raises Intermodulation Distortion (IMD) components at the receiver which severely degrade the performance of the system, because some of these components can be very close to the desired signal frequency. Figure 3.3 shows several spurious components which appear in the spectrum together with the two original frequencies ( $f_1$  and  $f_2$ ) of the transmitted signals. It can be noted that some of the frequency components are located at a considerable distance from the desired signal frequencies, e.g.  $2f_1$  and  $2f_2$ , hence they may be filtered out. By contrast, some of the IMD products such as  $2f_1 - f_2$  and  $2f_2 - f_1$  are located close to the desired signal frequencies, hence they cannot be readily filtered out.

## 3.2 UWB-over-fiber in railway scenario

Most of countries in Europe have deployed dedicated fiber-optic communication infrastructures that could be exploited to move the signal processing tasks from LCs to a central unit. For instance, the Italian railway operator Rete Ferroviaria Italiana (RFI) has developed an optical network which covers more than 10,000 km, 50% of which are available for future applications. Thanks to the presence of this fiber infrastructure, a realistic adoptable solution is the remotization of the processing tasks utilizing the UWBoF approach. Possible implementations of this concept are illustrated in Fig. 3.4 reporting the basic block diagram of the link considered. At each LC, a number  $N$ , depending of the number of sensors, of these links are present (one for each antenna). The  $i$ -th antenna of the LC ( $i = 1, \dots, N$ ) receives the fields determined by the UWB pulse emission of all the antennas, including itself, as in time division multiple access (TDMA) approach. The input of its electronic front-end (see again Fig. 3.4) is then given by the sequence of the tensions  $W_{i,1}(t), W_{i,2}(t), \dots, W_{i,N}(t)$ , determined respectively by the UWB pulses emitted by

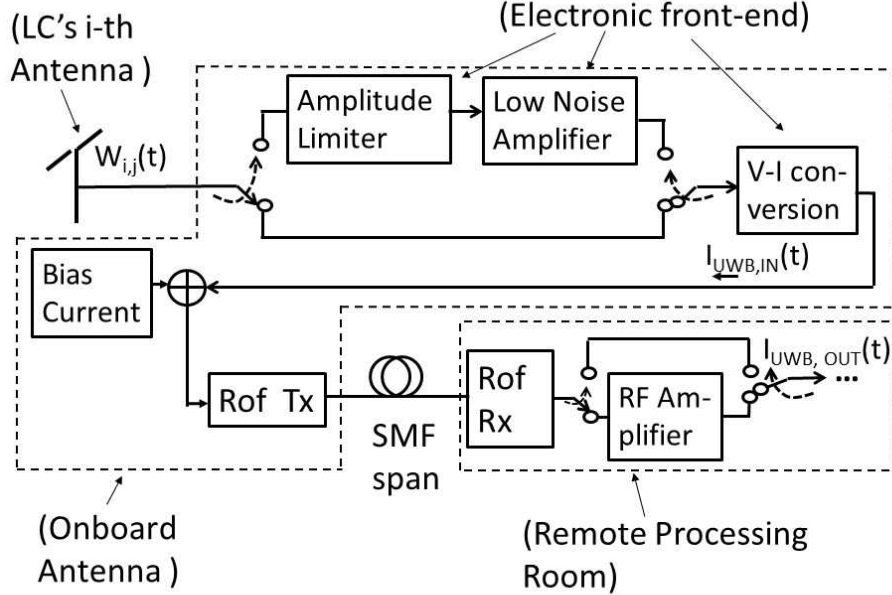


Figure 3.4: Block diagram of the receiving chain of the  $UWB$  signal up to the processing room

antennas  $1, 2, \dots, N$ . After having been processed by the electronic front-end, the various  $W_{i,j}(t)$  determine the current  $I_{UWB,IN}(t)$  which modulates the laser source. Each RoF transmitter (TX) is based on a Distribution Feed Back (DFB) laser. Although other laser sources may be less expensive (e.g. VCSELs or Fabry Perot ones), this one is to be preferred because it allows at the same time a large dynamic range of the input modulating signal and a high degree of linearity, namely high values of the second and third order input intercept points ( $IIP2$  and  $IIP3$ , respectively). On the other hand, the use of expensive highly coherent optical sources, like the External Cavity Lasers is not justified in this application, since the line-width of a few  $MHz$  easily exhibited by typical DFB lasers already allows the correct transmission of the  $UWB$  signal through direct intensity modulation.

Subsequently, a strand of G-652-compliant optical fiber is utilized, whose length typically stretches up to a few tens of km. At the centralized processing unit, each link features a RoF receiver (RX) based on a PIN-photodiode followed by an RF amplifier. The spectrum of the considered  $UWB$  signal ranges from  $3.5 GHz$  to  $5.1 GHz$ . We chose to operate in the lower part of the available spectrum (which is

$B_{Tot,UWB} = [3.1 GHz, 10.6 GHz]$  in the US and  $B_{Tot,UWB} = [3.4 GHz, 4.8 GHz][6.0 GHz, 8.5 GHz]$  in the EU) because of the widespread presence on the market of devices operating in this frequency range. Indeed, some technological requirements are here less severe. For example, at these frequencies the free space attenuation of the field is lower, and a direct modulation of the DFBs which avoids the use of costly external electro-optical modulators is easily realizable. The signal bandwidth was chosen as  $B_{Sig,UWB} = 1.6 GHz$ , which is compliant with the IEEE 802.15.4a. standard, because this value guarantees the required level of resolution in the time domain to perform an accurate post processing of the signals received by the various monitoring antennas.

The wavelength of operation for the DFB has been chosen as  $\lambda = 1310$  nm, so that, operating in the second optical window, where the chromatic dispersion is very low, the distortion effects due to the laser frequency chirp become negligible [22]. The main detrimental effect of the RoF transmission are then expected to come on one side from the undesired non linear effects like harmonic and intermodulation distortion, and on the other side from the increase in the noise figure of the system caused by the RoF link. For lower link lengths the increase of the noise figure is mainly caused by the relative intensity noise (*RIN*) of the DFB and by the shot noise of the PIN, while for higher link lengths the thermal noise of the RF amplifier of the RoF RX shows the greatest influence [24]. Note that a change in the value of the central frequency of the UWB signal from  $4.3 GHz$  to other values within the interval  $B_{Tot,UWB}$  would not lead to changes in the performance of the optical link, provided that  $B_{Sig,UWB}$  maintains the same value, and that both RoF TX and RoF RX operate correctly in the chosen frequency interval. On the contrary, the value of  $B_{Sig,UWB}$  influences the power of the different kinds of noise introduced by the optical link, which are proportional to such quantity. However, while a reduction of  $B_{Sig,UWB}$  would determine as a positive effect a reduction of the noise power, it would bring also as a negative effect a reduction of the time resolution by which the the various  $W_{i,j}(t)$  are processed, determining a detrimental influence on the monitoring capabilities of the global surveillance system.

As a further consideration, it must be taken into account that the range of maximum amplitudes exhibited by the various  $W_{i,j}(t)$  is quite wide. Indeed, when  $i = j$ , that is, when the same antenna receives the scattered field after having sent an UWB pulse, the maximum amplitude of  $I_{UWB IN}(t)$  is typically of fractions of  $mA$ . As an example, Fig. 3.5 reports typical behaviors of  $W_{1,1}(t)$  in presence and

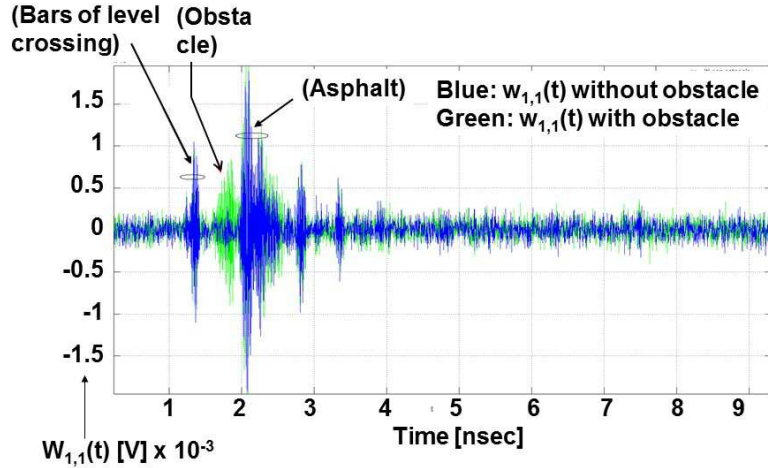


Figure 3.5: Example of computed behaviour of  $W_{1,1}(t)$  in presence and in absence of an obstacle in the LC.

in absence of an obstacle in the LC.

On the other hand, when  $i \neq j$ , the amplitude of the corresponding  $I_{UWBIN}(t)$  can reach a few tens of  $mA$ , due to the presence of a direct path between the  $i$ -th and the  $j$ -th antenna. As a consequence of this, two different configurations of the UWBoF link have been considered, which are both reported in Fig. 3.4. In the first one, the UWB signal coming from each antenna is converted into an electrical current and directly drives the DFB laser. This configuration has the advantage to be simple and less expensive. However, the absence of an initial amplification stage before the laser modulation is expected to determine a greater value of the RoF link noise figure. The second configuration shown in Fig. 3.4 includes the presence of a voltage clipper, which has been assumed ideal, limiting the maximum value of the amplitudes of the various  $W_{i,j}(t)$  so that  $|I_{UWBIN}(t)| \leq 2mA$ . This reduction of the portion of current due to the direct path does not affect the accuracy of the possible obstacle detection, since the contribution is present both in the *empty room* and in the actual measurement. The clipping operation allows then to place a Low Noise Amplifier at the electronic front-end, allowing for an expected reduction of the effect of the RoF link noise on the obstacle detection.

As mentioned above, in chapter 5 we will see the results obtained simulating the behaviour of both configurations of the UWBoF link for the centralized processing of the level crossings surveillance through a UWB partial multi-static radar.

## Chapter 4

# UWB PAI-PL with Fixed Object Scanning

As said before in section 1.3.2, the UWB radar technology and its features make it a good candidate for PAI-PL surveillance systems. The section 4.1 explains the mono-static and multi-static radar concepts, which are the basic ideas behind the multi-static and imaging radar systems (4.2). In section 4.4 I expose the mathematical model implemented to build simulated partial multi-static radars, the methods to process the UWB signals and the derivation of ML schemes to localize, detect and to provide roughly informations on volume of obstacles in our system.

### 4.1 UWB sensor networks: Overview

UWB sensor networks are extremely flexible and can be used in several configurations depending of the application. In particular we can distinguish between the following 3 configurations:

- mono-static radar: transmitter and receiver in the same location (see Fig. 4.1.b);
- bi-satic radar: transmitter and receiver are placed in different position (see Fig. 4.1.a)
- multi-static: many transmitters and receivers are placed in different position (see Fig. 4.1.c).

Unlike a mono-static radar, which uses the same antenna for both the transmitted and received signal, a multi-static radar uses at least three spatially distributed

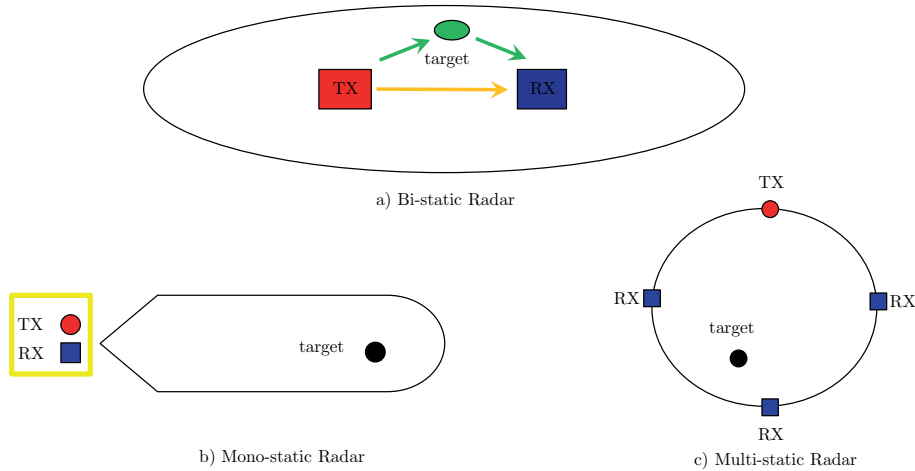


Figure 4.1: UWB different configuration

antennas for transmitting and receiving placed at precise location (sensors must at first know their own local coordinate system and their relative position) [25]. The main advantages of a multi-static radar over a classic mono-static one include a wider area coverage and a higher amount of information available due to spatial diversity. Moreover, receivers in a multi-static radar system are not required to transmit any signal, which enables development of low power and low cost equipments. When multiple antennas are used in each node, the resulting sensor network is also called MIMO radar capable of estimating, also, the angle-of-arrival (AOA) [25].

We focus on impulse IR-UWB radars which are characterized by the transmission of short duration pulses of the order of a few nanoseconds [26]. IR-UWB offers an extraordinary resolution and localization precision. Additional advantages include low power consumption, high spatial resolution (typically a few centimeters) even in indoor environments with dense multipath, high security and low probability to be intercepted, co-existence with a large number of devices operating in small areas [17]. These features make IR-UWB radars suitable for various recent applications such as radar sensor networks addressed to detect and track non-cooperative targets (e.g., human subjects) moving inside a surveillance area [1, 27].

The increased available informations of the propagation environment and UWB extraordinary resolution allow us to build a rather detailed image of the structure observed. A focussed image can be built if enough information is collected. The quality of this image heavily depends on the number and the positions of the observing sensors. If they are available simultaneously, then the collected information allows

real-time localization of objects. As it will be seen later, however, IR-UWB requires temporal synchronization between the sensors through a common time reference. By applying coherent data fusion methods an image of the propagation environment can be obtained.

For the scope of this thesis, with regard to the capabilities of sensor nodes involved and to their mutual cooperation, we refer to the multi-static approach, which assumes a number of static and synchronized cooperating sensor nodes with known distribution.

## 4.2 Multi-static UWB radar and Imaging scanner radar

In this section we discuss the main characteristics of Multi-static UWB and Imaging radar because they represent the reference architectures on which our FOS algorithm is based.

### 4.2.1 Multi-static UWB radar

UWB is the ideal candidate for short-range radar sensor network applications, especially in its impulse radio (IR) version, characterized by the transmission of a few nanoseconds duration pulses [26].

A typical multi-static UWB radar is composed of one transmitting (TX) node and  $n_R$  RX nodes (with  $n_R \geq 3$ ) deployed on the perimeter of the area to provide a full area coverage (see Fig. 4.3). A central node (or fusion node) collects the received signals from all of the receivers and performs the required data processing.

The IR-UWB radar transmits continuously a sequence of UWB pulses at time intervals  $T_P$  (few nanosecond). The received signals are observed and processed in the frame time of duration  $T_F$  (a fraction of a second). If  $N_s$  pulses are emitted by the transmitter during each frame time, then  $T_F = N_s \cdot T_P$ . At the receiver side by averaging along the frame time the signal-to-noise ratio (SNR) can be increased by factor equal to  $N_s$ , also called *processing gain*. The transmitted pulse at time  $t$  is assumed to be the first derivative Gaussian monocycle:

$$p(t) = A \cdot \exp - \left( \frac{t^2}{2\tau_p^2} \right) \quad (4.1)$$

with duration parameter  $\tau_p$ . The pulse modulates a sinusoidal carrier to make the emitted signal compliant with FCC regulations. Although in this thesis, we have used the first derivative, as in the Fig. 4.2 with  $\tau_p = 1 \text{ ns}$ , higher derivative orders

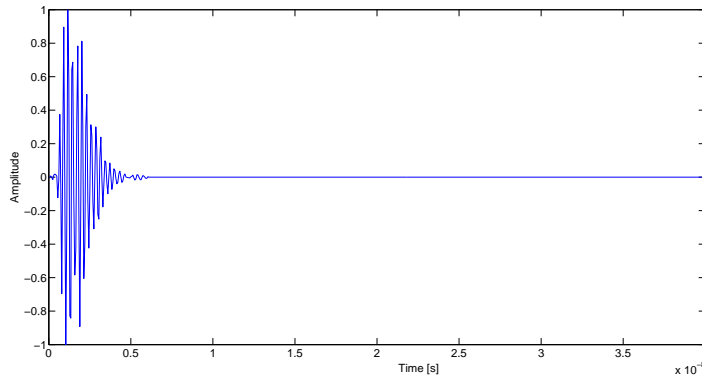


Figure 4.2: The pulse template in time domain

may also be considered without the need of sinusoidal modulation. If an obstacle is present inside the monitored area, the received signal at each receiver, corresponding to a UWB transmitted pulse, consists of the direct path pulse followed by pulse replicas due to both the clutter and the obstacle, and the noise. In the considered system, direct path and replicas are estimated through TOA principle.

An interesting application of multi-static UWB radar is the anti-intruder system able to precisely locate and eventually track moving targets inside a surveillance area, as studied in works [1, 26, 27]. The target detection and location process comprises a number of subsequent steps, which can be summarized as TOA estimation, clutter removal, soft-valued correlation map formation, imaging and detection. The TOA estimation, clutter removal and correlation map formation are performed independently by each RX node, while the other steps are performed by the fusion node (central node).

As explained before, during a frame time of duration  $T_F$ , a sequence of  $N_s$  UWB pulses at intervals  $T_P$  is emitted by the TX node. The system is designed in such a way that the channel response to a single pulse when a moving target is present does not change appreciably during a frame time, but is different for pulses belonging to subsequent frames. If a target is present inside the area, each emitted UWB pulse determines the reception, by each RX node, of the direct path pulse followed by pulse replicas due to both the clutter and the target. The estimation of the TOA of the direct path pulse allows the RX node to perform a coherent average operation of the  $N_s$  channel responses, thus reducing the noise power by a factor  $N_s$  (process gain). A clutter cancellation algorithm is then applied, e.g. frame-to-frame or empty-room algorithms [3].

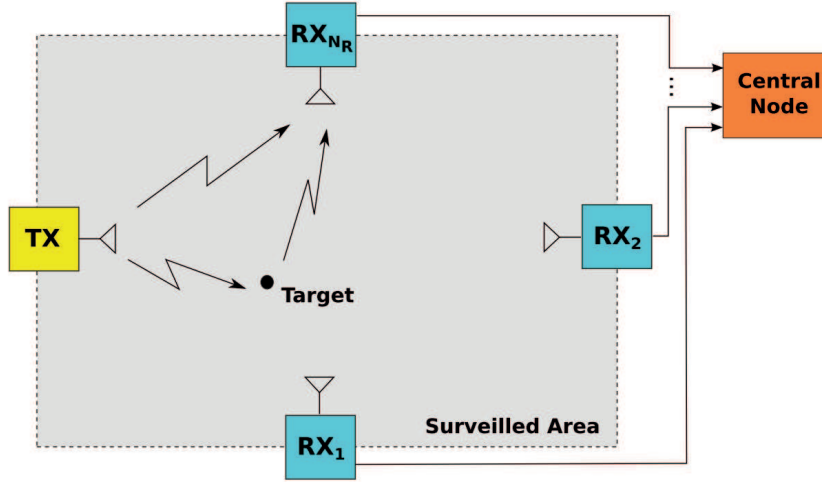


Figure 4.3: Anti-intruder UWB multi-static radar system [1]

Next, assume the area is divided into pixels. For each TX-RX pair, each pixel is associated with a specific time delay of the target-scattered pulse, w.r.t. the direct path pulse, assuming a target is present in that pixel. For all pixels, the correlation is calculated between the sampled signal obtained after the clutter removal step and a delayed local replica of the UWB pulse, with the delay relevant to the considered pixel. In such a way, each RX node computes a soft-valued correlation map of the area. The  $n_R$  correlation maps are transferred to the fusion node, where they are combined pixel-wise to obtain a soft image of the area. This image may be used to take a pixel-wise decision about the target presence or absence, where the decision is taken by comparing the local soft value with a threshold. Clearly, the correlation values returned by the  $n_R$  RX nodes in that pixel shall be combined in such a way to minimize the probability of false alarm. According to the maximum likelihood (ML) criterion, this is possible by adopting as a decision metric according to the corresponding log-likelihood ratio (LLR) [1].

#### 4.2.2 Imaging scanner radar

When a large amount of measurements from several different positions around the object are collected it is possible to reconstruct the shape of the object with high precision (imaging). The problems related to the accurate identification and super-resolution UWB imaging of shaped 3D Objects can be thought as a imaging scanner radar. In particular, the applicability of the Range Points Migration (RPM) is

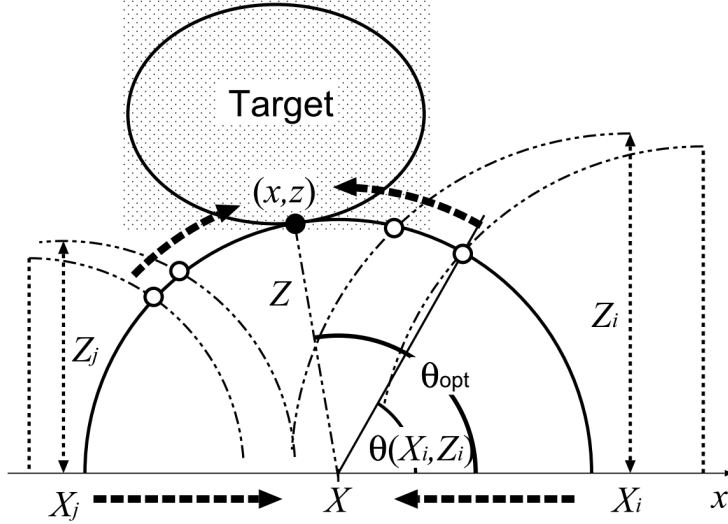


Figure 4.4: AOA & convergence orbit of the intersection points [2]

investigated in [2] and [28], in order to reconstruct the lateral object region in the first and a full 3D object contour in the latter.

The 2D RPM algorithm introduced in [2] refers to a planar mono-static sensor which perform a scanning track nearby to the object, which allows the reconstruction of a partial image of the lateral region of the object. This algorithm is based on the principle that a target boundary point should exist on the circle with center  $(X, 0)$  and radius  $Z$ . Thus, each target point  $(x, z)$ , as it can be seen in Fig. 4.4 can be calculated from the angle of the arrival. For a stable angular estimation, this method utilizes the membership function  $f(\theta, X_i, Z_i)$  as

$$f(\theta, X_i, Z_i) = \exp - \frac{[\theta - \theta(X_i, Z_i)]^2}{2\sigma_{\theta}^2} \quad (4.2)$$

where  $\theta(X_i, Z_i)$  is defined as the angle of the intersection point between the circles with  $(X, Z)$  and  $(X_i, Z_i)$ . Fig. 4.4 shows the relationship between the intersection point and  $\theta(X_i, Z_i)$ . So, it is possible to calculate the optimum angle for each  $(X, Z)$  with signal amplitude  $s(X_i, Z_i)$  as,

$$\theta_{opt} = \arg \max_{\theta} \left( \sum_i s(X_i, Z_i) f(\theta, X_i, Z_i) e^{-\frac{(X-X_i)^2}{\sigma_X^2}} \right) \quad (4.3)$$

where  $\sigma_{\theta}$  and  $\sigma_X$  are constants, that are empirically determined. The weight  $s(X_i, Z_i)$  in Eq. 4.3 improves the noise tolerance. This method realizes the direct transform from the points of  $(X, Z)$  to the target point  $(x, z)$ .

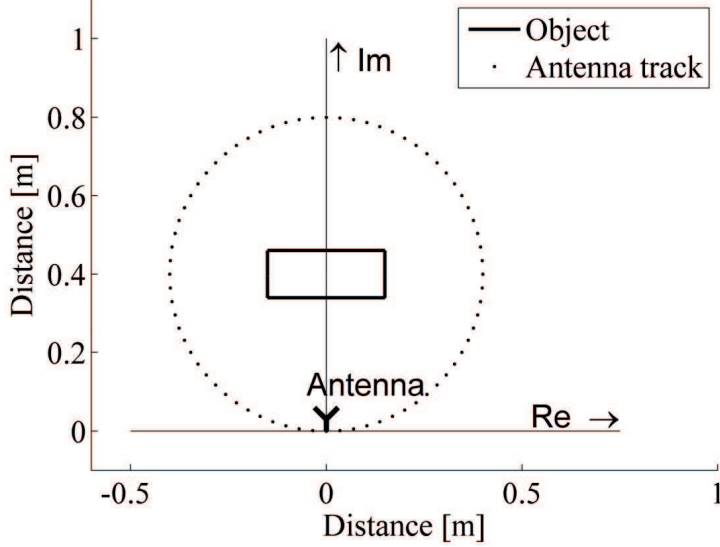


Figure 4.5: Measurement setup of the 2D circular track [3]

The 2D RPM allows only a limited imaging of the object lateral region when sensor moves along a straight trajectory. For this reason it was extended to the 3D case in [28]. To do this, the mono-static sensor is placed on a planar surface in front of the 3D object following a circularly scanning track. The 3D scenario is investigated by adding the  $z$ -axis and performing the circular tracks on different heights. The studied RPM algorithms extract a 3D image from the aforementioned multiple 2D scans. In Fig. 4.5 the measurement set-up of a 2D circular track with rectangular obstacle is shown.

The 3D RPM Imaging is an extension of the 2D scenario with circular scan track performed at different heights (depending on the resolution requirements), e.g. a grid of  $2 - 3$  cm in  $z$ -direction is sufficient for adequate 3D UWB images.

Using the same principle expressed in Eq. 4.3, 4.2  $\theta(X_i, Z_i)$  can be derived. Unfortunately, in this case by considering two antenna positions along the track, the intersection angle is ambiguous since both circles around the 2 antenna coordinates intersect twice. However, if directive horn antennas are used, it is possible to discard the intersection outside the antenna track. The angular estimation of the DOA is required as explained in [28]. Moreover, the 3D RPM version suffers from the superposition of multiple 2D images to one 3D image, and to avoid the creation of a false image, the DOA estimation for the 2D case has to be repeated for  $N_v$  positions above and below the antenna at the considered height value ( $N_v$  depending on resolution requirement).

### 4.3 Advantages and disadvantage of Multi-static and Imaging radars

The UWB radar systems illustrated in sections 4.2.2 and 4.2.1 have own advantages and disadvantage, in particular by referring to the goal of the thesis of detecting, localizing and estimating the obstacle volume within a railway monitored area like Level crossing (LC).

In the multi-static IR-UWB radar w.r.t. railway surveillance systems arises three major problems:

- A. Blind Zones for each pair of TX and RX antennas.
- B. Static Infrastructure versus a full image requirement. Most of existing algorithms detect only moving targets and fail with steady targets (e.g., a car entrapped within the LC area).
- C. No existing algorithms for full imaging in static infrastructure.

Blind zones are regions inside which the difference between the delays corresponding to target-reflected path and direct path is lower than the system time resolution. When the target is close to a line-of-sight (LOS), connecting the TX and any of the RX antennas, it may fall inside the corresponding blind zone, in which case it can not be detected by that RX antenna. Blind zones are consequence of two main concurrent phenomena as: the *non-ideal synchronization* of TOA estimation of the direct-path pulse and the *sampling resolution*, which maps the target position onto quantized ellipses inside the area [27].

The second and third disadvantages can be seen as complementary. In the literature most of results have been presented for ideal point obstacles and it is claimed that at most 4 receivers are sufficient for a reliable detection and localization without considering the fundamental role of realistic obstacles scattering characteristics. Therefore, there are not developed algorithms which give any information of volume obstacles. The absence of real imaging algorithms is exacerbated by the impossibility, for its nature, of the railway surveillance system to perform scanning track around the perimeter of the monitored area to create a full 3D image as imaging scanner radar.

On the other hand, Imaging scanner radar w.r.t. railway surveillance systems requires:

- A. Collecting a critical amount of signals to be processed;

B. Scanning track around obstacles in the perimeter of the monitored area;

C. DOA estimation.

As described in the previous section, the RPM algorithm performs a track around the obstacle and for each position track the sensor takes a decision about target point coordinates  $(x, z)$ . This process can seriously exasperate the detecting phase by leading to the desired "quasi" *real time* response about obstacle presence. Moreover as stated before, the infrastructural constraint of no moving sensor (feasible in indoor scenario) cannot allow the system to perform scanning track around obstacles for a full 3D image.

Finally, the required DOA estimation in 3D RPM algorithm impacts on the computational complexity of the system and the need to use directional antennas.

It is evident that Multi-static and Imaging radars in their stand-alone version are not completely compliant with railway surveillance system requirements. For this reason we have developed a hybrid approach combining the UWB multi-static radar and the mono-static imaging scanner configurations. As a consequence, it allows for gaining some of the advantages of both configuration and mitigating their drawbacks. The system maintains the flexibility to use weak directive antennas and its simplicity by detecting obstacle through TOA direct path and replicas estimation, without performing scanning track around monitored area and DOA estimation process, while allowing the possibility to extract a rough 3D image and volume computation.

#### 4.4 The FOS Imaging Algorithm

The previous sections have illustrated the two types of UWB radars studied to develop the idea of PAI-PL systems taking advantage of UWB features. The surveillance system investigated is composed of a set of transmitting (TX) and receiving (RX) nodes, located at different heights at the vertices of the monitored area, as shown in Fig. 1.1. As it will be described later, the sounding of the environment via UWB interrogation signals and subsequent analysis of backscattered signals is split in different phases to which only a subset of nodes participate leading to a partial multi-static radar configuration. In addition, with the purpose to facilitate the 3D imaging algorithm described later, the monitored area is subdivided into  $N_{\text{pixel}}$  3D cubic pixels of side  $\Delta$ . The 3D imaging process of the obstacle can be summarized in the following steps: clutter removal, pixel detection, imaging, and volume estimation.

#### 4.4.1 Signal Model

Denote with  $\mathcal{A}_p$  the set of transmitters and receivers pairs which are active during the phase  $p$ , with  $p \in \{A, B, C, D, E\}$  as shown in Fig. 4.6. To avoid inter-nodes interference a time division multiple access (TDMA) approach is considered where only one node is transmitting and the others are receiving. Consider, without loss of generality, the active transmitter sends an interrogation UWB pulse  $g(t)$ . Note that in actual UWB systems, to overcome the low emission power imposed by regulatory issues, a sequence of  $N_p$  pulses is usually transmitted to allow the receiver for collecting more energy. In case of coherent receivers, our analysis considering the transmission of a single pulse is equivalent to that of multiple pulses if a noise power reduction of  $N_p$  is taken into account (processing gain).

The signal backscattered by the environment and received by the RX node of the  $i$ th pair, with  $i \in \mathcal{A}_p$ , is

$$r_i(t) = s_i(t) + n_i(t) \quad (4.4)$$

where  $s_i(t)$  is the useful signal component and  $n_i(t)$  is the additive white Gaussian noise (AWGN). The useful component can be further decomposed into a sum of contributions (if any) coming from all the 3D pixels the area has been subdivided into. Specifically, it can be written as,

$$s_i(t) = \sum_{k=1}^{N_{\text{pixel}}} a_i^{(k)} \cdot p_i^{(k)}(t - \tau_i^{(k)}) \quad (4.5)$$

with  $\tau_i^{(k)}$  being the transmitter-pixel-receiver time-of-flight of the signal, and  $p_i^{(k)}(t)$  being the channel response to  $g(t)$  (if present) due to the  $k$ th pixel including also the multipath. The term  $a_i^{(k)}$  accounts for the total path loss, that is

$$a_i^{(k)} = \begin{cases} 0 & \text{empty or shadowed pixel} \\ \frac{1}{\sqrt{PL_i^{(k)}}} & \text{otherwise} \end{cases} \quad (4.6)$$

having defined  $PL_i^{(k)} = PL_{\text{TX},i}^{(k)} \cdot PL_{\text{RX},i}^{(k)} \cdot \sigma_i^{(k)}$  the total path loss experienced by the two nodes, where  $PL_{\text{TX},i}^{(k)}$  and  $PL_{\text{RX},i}^{(k)}$  are the attenuations due to the free-space propagation between the TX and the obstacle, and the obstacle and the RX, respectively.  $\sigma_i^{(k)}$  accounts for the obstacle reflection coefficient related to the part of the obstacle falling in the  $k$ th pixel, and it is strictly linked to the angle  $\theta$  formed by the incident and the backscattered waves. In Fig 4.7 all propagation phenomena

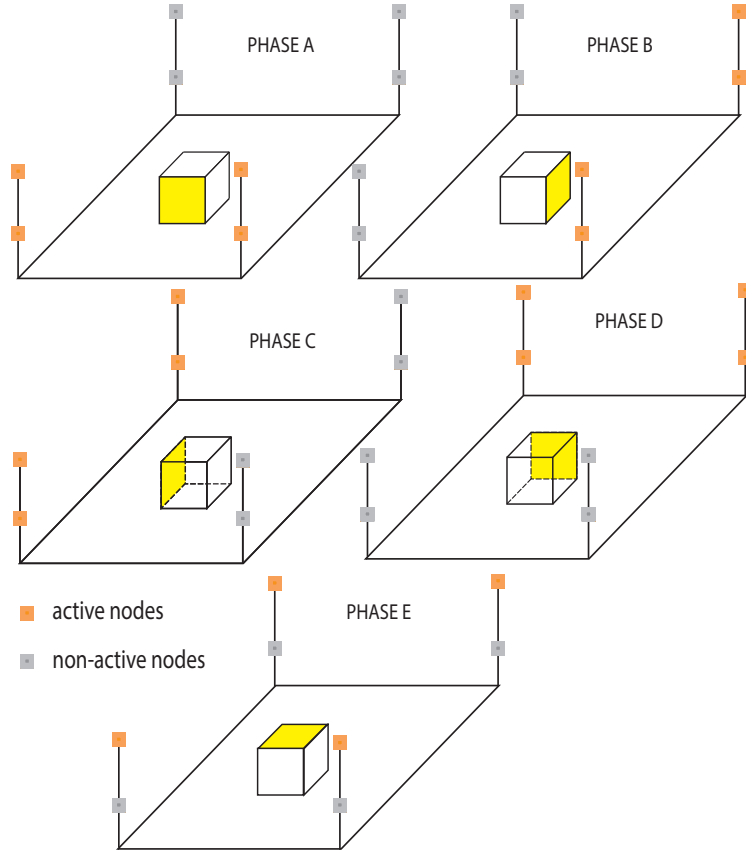


Figure 4.6: Active sensors depending on the phase  $p$  considered on FOS algorithm.

involved in the interrogation phase are illustrated. Note that typically only rays with  $\theta < 90^\circ$  (blue line) are reflected. This aspect will be taken into account in the 3D imaging algorithm described later.

Signals are successively sampled, with sampling time  $t_s$ , in  $N$  time instants  $t_1, t_2, \dots, t_N$  belonging to an observation interval containing all the useful received components, leading to

$$\mathbf{r}_i = \mathbf{s}_i + \mathbf{n}_i \quad (4.7)$$

with  $\mathbf{r}_i = [r_{i,1}, r_{i,2}, \dots, r_{i,N}]^T = [r_i(t_1), r_i(t_2), \dots, r_i(t_N)]^T$  and similarly for  $\mathbf{s}_i$  and  $\mathbf{n}_i$ . Each component of vector  $\mathbf{n}_i$  is a zero mean Gaussian random variable (RV) with variance  $\sigma^2$ .

#### 4.4.2 Clutter Removal and Ghost Effect Mitigation

An important issue when detecting the presence of steady obstacles is the static environment response (*static clutter*) caused, for example, by the rail and poles.

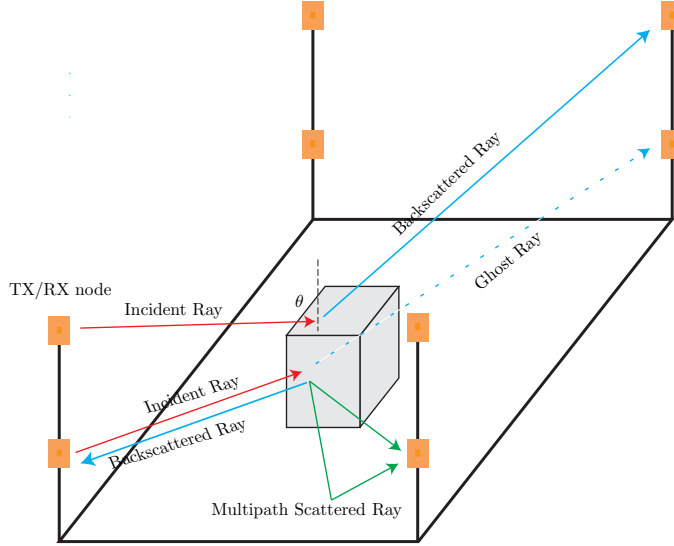


Figure 4.7: Path loss between nodes when the signal is backscattered by the obstacle

This component is removed by using an *empty-room* approach [3] in which the reference signals  $\check{\mathbf{r}}_i$ , recorded in the absence of obstacles, are subtracted from the actual received signals. Note that when an obstacle is present, part of the static clutter could be hidden leading to imperfect clutter suppression (see Fig 4.7). To counteract this *ghost effect*, only the signal components corresponding to positive variations in the received energy are taken into account during the clutter removal process.

In particular, for each sampled version of the received signal, we have

$$\begin{cases} \mathbf{r}_i = \mathbf{r}_i - \check{\mathbf{r}}_i & \text{if } |\mathbf{r}_i|^2 \geq |\check{\mathbf{r}}_i|^2 \\ \mathbf{r}_i = 0 & \text{if } |\mathbf{r}_i|^2 < |\check{\mathbf{r}}_i|^2 \end{cases} \quad (4.8)$$

where  $|\mathbf{r}|^2$  means element wise square operation.

### 4.4.3 3D Image Formation

In classical multi-static radar schemes, the backscattered response to the UWB interrogation signals sent by the transmitters is collected by all nodes and jointly processed by the localization algorithm. However, the finite size and the anisotropic scattering of the obstacle might prevent some nodes (e.g., those located in the opposite direction) from receiving the backscattered signal, differently from that expected by the multi-static radar algorithm (for example, in Fig 4.7 the ray represented by the dashed blue line). This generates, in addition to multipath components, serious

ambiguities in imaging formation and localization that might not be solved. To overcome such a limitation and inspired by the imaging scanner system, we consider a partial multi-static radar system which alternatively activates each side of the monitored area, as shown in Fig. 4.6. In particular, the proposed FOS algorithm performs 5 phases, 4 for the lateral sides and one for the top of the area. During each phase  $p$ , only the TX-RX pairs located in the considered side are activated and are included in the set  $\mathcal{A}_p$  thus miming mono-static imaging scanners with fixed nodes. In this way the resulting partial multi-static radar operates most likely in conditions where  $\theta < 90^\circ$  is satisfied, with a consequent significant mitigation of the aforementioned ambiguities during the imaging process.

Obstacle detection and image formation consist in checking whether the generic pixel is a candidate for containing part of the obstacle (if present). This can be accomplished by performing during phase  $p$  and for each pixel  $k$ , with  $k = 1, 2, \dots, N_{\text{pixel}}$ , the following binary detection test with unpredictable sign

$$\begin{cases} \mathbf{r}_i^{(k)} = \mathbf{n}_i & \mathcal{H}_0 \\ \mathbf{r}_i^{(k)} = \pm a_i^{(k)} \tilde{\mathbf{g}}_i^{(k)} + \mathbf{n}_i & \mathcal{H}_1 \end{cases} \quad (4.9)$$

$\forall i \in \mathcal{A}_p$ , having defined

$$\tilde{\mathbf{g}}_i^{(k)} = [g(t_1 - \tau_i^{(k)}), g(t_2 - \tau_i^{(k)}), \dots, g(t_N - \tau_i^{(k)})]^T \quad (4.10)$$

the expected received signal templates delayed by time-of-flight  $\tau_i^{(k)}$ . The probability distribution functions (p.d.f.s) of the composite received signal  $\mathbf{r}^{(k)} = \left[ \left\{ \mathbf{r}_i^{(k)} \right\}_{i \in \mathcal{A}_p} \right]$  under  $\mathcal{H}_0$  and  $\mathcal{H}_1$  can be written, respectively, as

$$P(\mathbf{r}^{(k)} | \mathcal{H}_0) = \prod_{i \in \mathcal{A}_p} K \exp\left(-\frac{\sum_{n=1}^N (r_{i,n}^{(k)})^2}{2\sigma^2}\right) \quad (4.11)$$

$$\begin{aligned} P(\mathbf{r}^{(k)} | \mathcal{H}_1) = \prod_{i \in \mathcal{A}_p} \frac{K}{2} & \left[ \exp\left(-\frac{\sum_{n=1}^N (r_{i,n}^{(k)} - a_i^{(k)} \tilde{g}_{i,n}^{(k)})^2}{2\sigma^2}\right) \right. \\ & \left. + \exp\left(-\frac{\sum_{n=1}^N (r_{i,n}^{(k)} + a_i^{(k)} \tilde{g}_{i,n}^{(k)})^2}{2\sigma^2}\right) \right] \end{aligned} \quad (4.12)$$

with  $K$  being a constant whose value does not affect the test.

The LLR based on (4.11) e (4.12) can be written as

$$\ln \Lambda^{(k)}(\mathbf{r}^{(k)}) = \ln \frac{P(\mathbf{r}^{(k)}|\mathcal{H}_1)}{P(\mathbf{r}^{(k)}|\mathcal{H}_0)} \quad (4.13)$$

$$= -\frac{1}{2\sigma^2} \sum_{i \in \mathcal{A}_p} \sum_{n=1}^N \left( a_i^{(k)} \tilde{g}_{i,n}^{(k)} \right)^2 + \sum_{i \in \mathcal{A}_p} \ln \cosh \left( \frac{1}{\sigma^2} \sum_{n=1}^N r_{i,n}^{(k)} a_i^{(k)} \tilde{g}_{i,n}^{(k)} \right). \quad (4.14)$$

To simplify the implementation of the test, the nonlinear function  $\ln \cosh(\cdot)$  can be approximated as

$$\ln \cosh(x) = \begin{cases} |x| - \ln 2, & \text{if } |x| \gg 1 \\ x^2/2, & \text{if } |x| \ll 1 \end{cases}.$$

Finally we can write the LLR test as follows

$$\sum_{i \in \mathcal{A}_p} \frac{1}{\sigma^2} \left| \sum_{n=1}^N r_{i,n}^{(k)} a_i^{(k)} \tilde{g}_{i,n}^{(k)} \right| \underset{\mathcal{H}_0}{\overset{\mathcal{H}_1}{\geq}} \ln \xi + \sum_{i \in \mathcal{A}_p} \sum_{n=1}^N \frac{\left( a_i^{(k)} \tilde{g}_{i,n}^{(k)} \right)^2}{2\sigma^2} \quad (4.15)$$

when  $\frac{1}{\sigma^2} \left| \sum_{n=1}^N r_{i,n}^{(k)} a_i^{(k)} \tilde{g}_{i,n}^{(k)} \right| \gg 1$  and, in the opposite case, the approximation becomes

$$\sum_{i \in \mathcal{A}_p} \frac{1}{\sigma^2} \left( \sum_{n=1}^N r_{i,n}^{(k)} a_i^{(k)} \tilde{g}_{i,n}^{(k)} \right)^2 \underset{\mathcal{H}_0}{\overset{\mathcal{H}_1}{\geq}} \ln \xi + \sum_{i \in \mathcal{A}_p} \sum_{n=1}^N \frac{\left( a_i^{(k)} \tilde{g}_{i,n}^{(k)} \right)^2}{2\sigma^2}. \quad (4.16)$$

Note that in both cases the threshold  $\xi$  is set according to the Neyman-Pearson criterion in order to guarantee a certain probability of false alarm (PFA), which is the probability to detect an object even if it is not present in the monitored area [29]. The system has an overall false alarm probability depending on the single pixel probability of false alarm. Specifically, the probability of false alarm (PFA) for each pixel is defined as,

$$p_{FA}^{N_{pixel}} = \int_{\tilde{\xi}_k}^{\text{inf}} P(\mathbf{r}^{(k)}|\mathcal{H}_0) \quad (4.17)$$

where this integral can be expressed as in [30] resulting in

$$p_{FA}^{N_{pixel}} = \frac{\Gamma\left(\frac{N}{2}, \frac{\tilde{\xi}_k}{2}\right)}{\Gamma(N/2)} = \tilde{\Gamma}\left(\frac{N}{2}, \frac{\tilde{\xi}_k}{2}\right) \quad (4.18)$$

where  $N = 2WT_I$ , with  $T_I$  is the sampling pulse and  $W$  is the bandwidth.  $\Gamma(a, x) = \int_x^{\text{inf}} x^{a-1} e^{-x} dx$  is the upper incomplete gamma function and  $\tilde{\Gamma}(\cdot, \cdot)$  is the gamma regularized function. The overall PFA can be expressed as,

$$P_{FA} = 1 - (1 - p_{FA})^{N_{pixel}}. \quad (4.19)$$

Finally, the threshold  $\xi$  can be derived according to

$$\xi = \frac{4}{N_{pixel}} \tilde{\Gamma}^{-1} \left( \frac{P_{FA}^*}{N_{pixel}}, \frac{N}{2} \right) \quad (4.20)$$

which now depends on the desired false alarm probability  $P_{FA}^*$ .

As stated before, the procedure expressed in 4.16 is repeated for each pixel and phase. In the end, all binary test outputs are combined to form the 3D image. In particular, the presence of part of an obstacle in a 3D pixel is detected if at least one LLR was successful during the scanning phases.

#### 4.4.4 Obstacle Volume Estimation

The result of the 3D image formation described in the above section is used as input for volume computation to estimate the obstacle size when it is present and generate an alarm to stop the train if it is greater than 1 cubic meter. Two methods of volume computation are provided:

- average sphere volume computation (ASVC)
- average parallelepiped volume computation (APVC).

The common step of these two approaches is to find the centroid of illuminated the pixels i.e., those detecting as not empty. Assuming that the FOS algorithm returns the set  $\mathbf{i}_1, \dots, \mathbf{i}_M$  of illuminated pixels, where  $\mathbf{i}_i = [x_i \ y_i \ z_i]$ , the centroid coordinates  $\mathbf{c} = [c_x \ c_y \ c_z]$  are computed as

$$\begin{aligned} c_x &= \frac{1}{M} \sum_{i=1}^M x_i \\ c_y &= \frac{1}{M} \sum_{i=1}^M y_i \\ c_z &= \frac{1}{M} \sum_{i=1}^M z_i \end{aligned} \quad (4.21)$$

with  $M$  being the cardinality of the set. Once the centroid coordinates are evaluated, the ASVC method computes the volume of a sphere centered in  $\mathbf{c}$  with radius  $R$  equal to the average pixels distance, that is

$$R = \frac{1}{M} \sum_{i=1}^M \|\mathbf{i}_i - \mathbf{c}\|. \quad (4.22)$$

The APVC method creates, instead, a parallelepiped centered in  $\mathbf{c}$  with sides

$$\begin{aligned}\Delta x &= \frac{2}{M_{\text{BC}}} \sum_{i=1}^{M_{\text{BC}}} |x_i - c_x| \\ \Delta y &= \frac{2}{M_{\text{AD}}} \sum_{i=1}^{M_{\text{AD}}} |y_i - c_y| \\ \Delta z &= \frac{2}{M_{\text{E}}} \sum_{i=1}^{M_{\text{E}}} |x_i - c_z|. \end{aligned} \tag{4.23}$$

where  $M_{\text{BC}}$  is the subset cardinality of illuminated pixel coming from the union of phases B and C of FOS algorithm used to determine the  $x$  side of the parallelepiped. Similarly for the subset coming from the union of phases A and B to determine  $y$  component ( $M_{\text{AD}}$ ) and phase E to  $z$  component ( $M_{\text{E}}$ ).

## Chapter 5

# Simulation Results

In order to evaluate the effect of a single obstacle placed in different positions within the area between the barriers, in this chapter two system configurations composed, the first of  $N_{\text{TX}} = N_{\text{RX}} = 4$  sensors and the second of  $N_{\text{TX}} = N_{\text{RX}} = 8$  sensors are considered respectively. In the first one all nodes are at height of 3 m, whereas the second has 4 sensors at height of 3 m and 4 at 0.8 m (as shown in Fig. 4.7). The surveillance area is divided in 3-D pixels of side  $\Delta = 10$  cm and the overall false alarm probability is set to  $P_{\text{FA}} = 10^{-3}$ . The channel transfer function between each TX-RX pair has been simulated with the aid of the 3D RT software described in [31] and in chapter 2. As mentioned, in addition to specular reflection and edge/-corner diffraction, modeled through geometrical optics (GO) and uniform theory of diffraction (UTD), the RT tool accounts for the effect of diffuse scattering, modeled through the ER approach. Therefore, we take into account the scattering parameter  $S$ , which accounts for the amount of the incident power diffused in all directions at the expenses of specular reflection, due to the presence of surface and volume irregularities. The obstacle is modeled as a metal box, whereas ground, barriers, tracks and antenna poles are modeled as slabs. Successively, the UWB channel responses obtained for each TX-RX couple are convoluted in time with a root-raised cosine pulse centered in the frequency  $f_0 = 4.3$  GHz with roll-off factor  $\beta = 0.6$  and pulse and pulse width  $t_p = 1$  nsec, compliant with the FCC mask in the 3 – 5 GHz band [16].

In section 5.1 we illustrate the first results obtained with classical multi-static radar algorithms (as explained in section 4.2), where all 4 nodes cooperate simultaneously to the localization and detecting process. Here the need to move toward a system configuration enhanced with additional sensors will be evident. Starting

from this consideration, the FOS is tested and the results in section 5.2 are shown to provide the goodness of the solution proposed. Specifically, the 3D imaging approach described in section 4.4 has been validated with obstacles having volume 5.83, 1, 0.34  $m^3$  placed inside the surveillance area [16].

Finally, results on the possibility to remotize the post-processing decision into a fusion center placed far from the LCs areas as described in chapter 3 are shown [18].

## 5.1 Simulation results with multi-static radar approach

First of all, the configuration with  $N_{TX} = N_{RX} = 4$  sensors with the classic multi-static radar approach was verified to understand whether it can provide any obstacle volume information. To asses that, the UWB channel transfer function between each TX-RX pair was obtained through 3D RT where the obstacle was modeled as a metal box, whereas ground, barriers, tracks and antenna poles were modeled as slabs, as introduced at the beginning of this chapter. Moreover, the scattering parameter was varied for different value to asses the detection and localization system capability w.r.t. the level of roughness of the obstacle.

Figure 5.1 shows the illuminated pixels derived from classic approach relative to the scenario studied with RT. From the left figure, it is evident that with  $S = 0.3$  (realistic value representative of materials with significant surface and volume irregularities), the algorithm is able to detect with a precision of 10 *cm* the upper face of metal box, since it is seen by all 4 sensors. Some pixels are illuminated at slightly larger height due to the pixel discretization. The right figure, instead, reports how a lower level of roughness ( $S = 0.1$ ) makes obstacle localization less reliable. In fact, the limited scattering diminishes the capability of some receivers to detect the backscatter signal. This generates ambiguities in the localization process leading to the detection of pixels in incorrect locations, as evident in Fig. 5.1-right. The results reported by this study of a surveillance system based on UWB multi-static radar highlight some interesting problems when considering real propagation conditions and 3-D scenarios. While in the literature most of results have been presented for ideal point obstacles and it is claimed that at most 4 receivers are sufficient for a reliable detection and localization [1, 27], here we have seen that with realistic obstacles the scattering characteristics play a fundamental role. In fact, when scattering is almost absent and under certain conditions of reflection, the localization of obstacles might suffer from discrimination ambiguities. Therefore, for

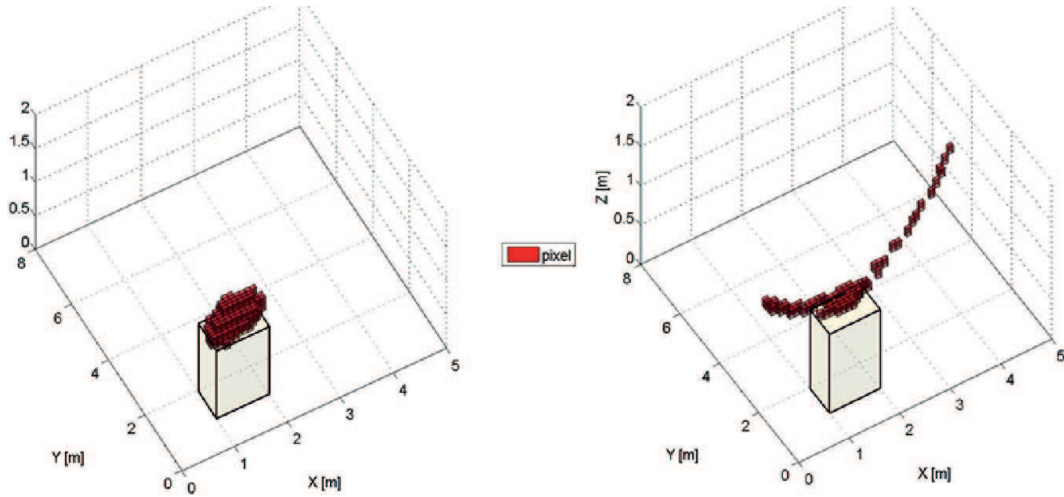


Figure 5.1: Illuminated pixels with 4-sensor classic approach, scatter parameter  $S=0.3$  (left figure) and  $S=0.1$ (right figure) for the metal box

a more accurate obstacle image reconstruction, the classical 4-receivers configuration must be enhanced with the introduction of additional receivers/transmitters and more effective signal processing.

## 5.2 Simulation results with FOS algorithm

For the reasons shown in the previous section, we have developed the FOS algorithm with a new system configuration. Here we show its improved performance in localizing, detecting and estimating volume of obstacles.

Figure 5.2 shows the 3D image output of the FOS algorithm when a metal box of  $5.72 \text{ m}^3$ , modeled with scattering parameter  $S = 0.3$ , is located in the middle of the area. The green line represents the real position of the obstacle in RT simulations. As can be noticed, the illuminated pixels match well with the obstacle contour, apart from a small set of outliers pixels. The yellow sphere juxtaposed is derived from the ASVC method whose volume can be taken as representative of the actual volume of the obstacle.

For comparison, the same simulation set up has been used to derive the results in Fig. 5.3 where the classical UWB multi-static radar approach is considered. Even though the presence of the obstacle is detected, the a huge number of outlier pixels arise due to ambiguities, thus making impossible a realistic volume computation and/or localization of the obstacle. Comparing with 5.2, the gain introduced by the

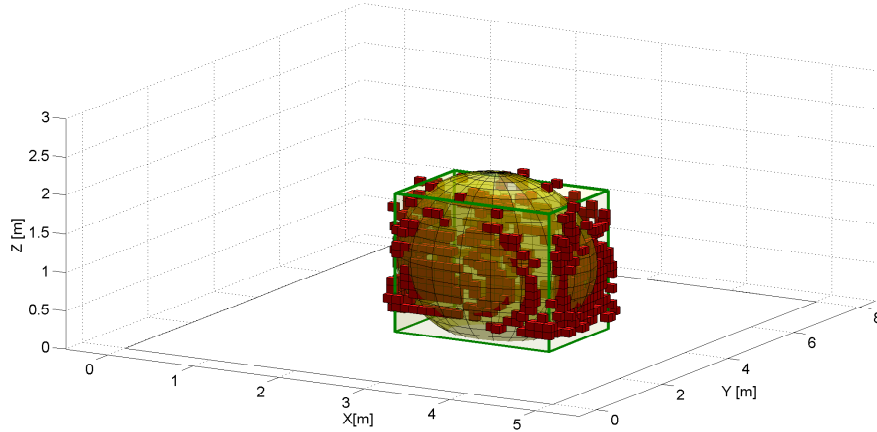


Figure 5.2: 3D image of a metal box of  $5.83 \text{ m}^3$  in the middle of the surveillance area. ASVC method.

proposed FOS algorithm is evident.

Figs. 5.4 and 5.5 report the results for a metal box of volume  $1.00 \text{ m}^3$  (critical volume set by railway regulation) placed in the lower corner on the left and in the middle of the area, respectively. The proposed FOS algorithm allows for the location of the obstacle in different positions as well as its 3D imaging.

Successively, a metal box of volume  $0.34 \text{ m}^3$ , which is below the critical volume value, is placed in the middle of the area, as shown in Fig. 5.6. As can be seen, the FOS algorithm is still capable of providing a 3D image with small objects.

To understand the effect of different scattering properties of the obstacle, Fig. 5.7 reports the results of FOS when an obstacle of critical volume with  $S = 0.2$  is present in the middle of the area. In this case our approach is still capable of detecting and locating the obstacle despite the total number of illuminated pixels compared with Fig. 5.5 is diminished due to the reduction of the total scattered power.

Finally, Table 5.1 summarizes the volumes computed in the scenarios investigated in the previous figures using the ASCV and APVC methods. As can be noticed, results provide a rough estimation of the actual volume of the obstacle.

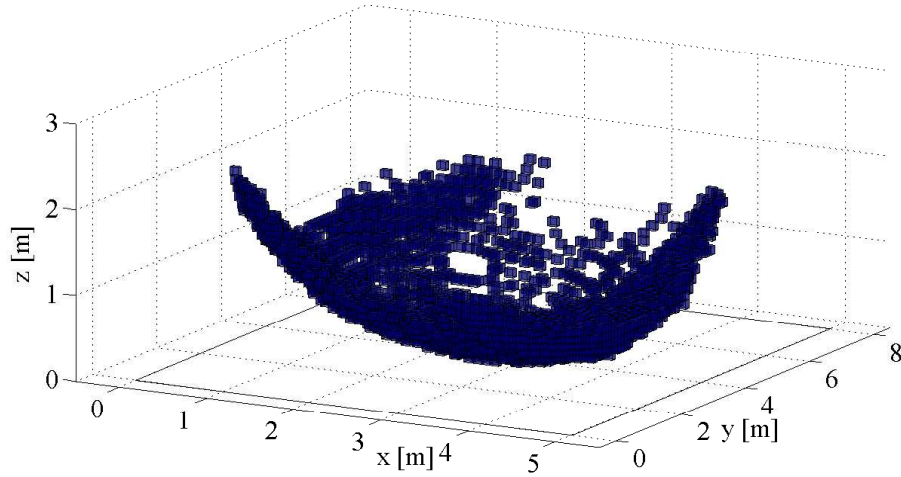


Figure 5.3: 3D image of a metal box of  $5.83 \text{ m}^3$  in the middle of the surveillance area using the classic UWB multi-static radar approach.

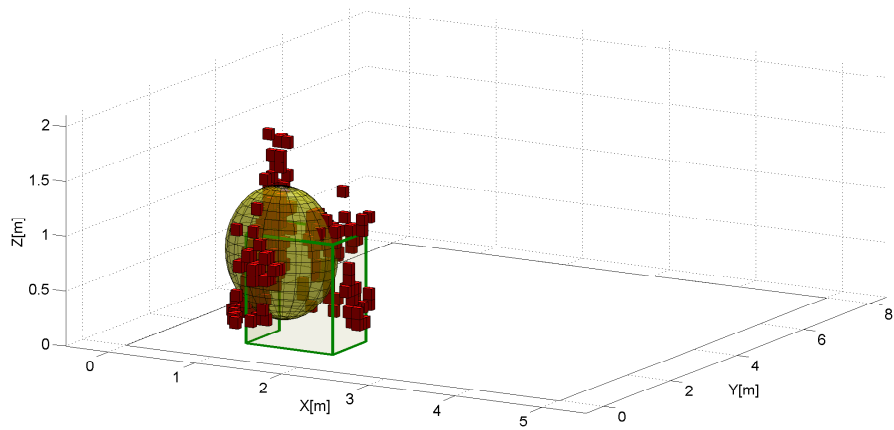


Figure 5.4: 3D image of a metal box of  $1 \text{ m}^3$  in the corner of the surveillance area. ASVC method.

### 5.3 UWBoF Simulation Results

Referring to a typical scenario, the various  $W_{i,j}(t)$  have been obtained and given in input to the UWBoF system, for the different applicative situations considered. Through the aid of the commercial software *Optsim* [32], the transmission of the  $W_{i,j}(t)$  through the UWBoF link was then simulated. The length of the fiber strand

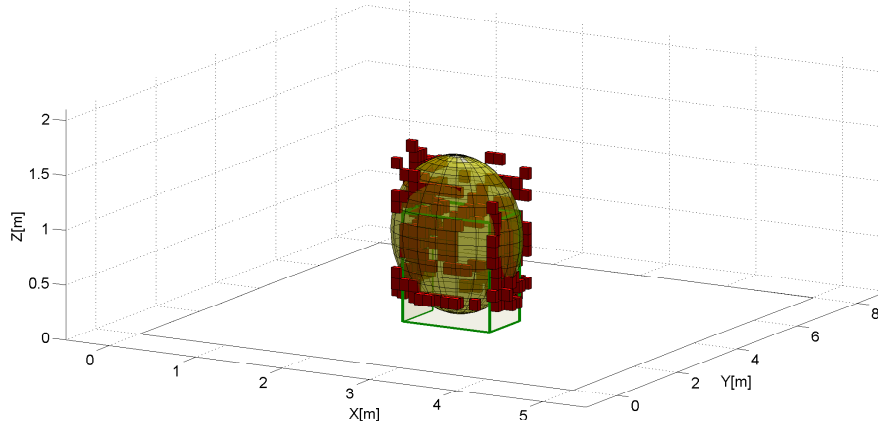


Figure 5.5: 3D image of a metal box of  $1 \text{ m}^3$  in the middle of the surveillance area. ASVC method.

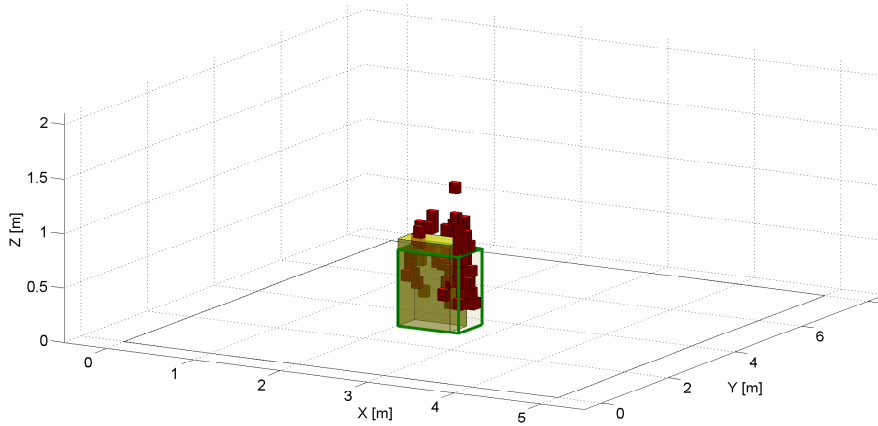


Figure 5.6: 3D image of a metal box of  $0.34 \text{ m}^3$  in the middle of the surveillance area. APVC method.

was varied in steps of  $10 \text{ km}$ , while typical values of the parameters of the optical and electrical components have been assumed. Table 5.2 reports a set of such values.

The two configurations described in the previous section have been considered. The total RF gain of the RoF link was set to be  $G_{RoF LINK} = 0 \text{ dB}$  in both of them. In the first case, the amplification of the UWB current necessary to counterbalance the losses of the optical part of the RoF link was performed by the RF amplifier at

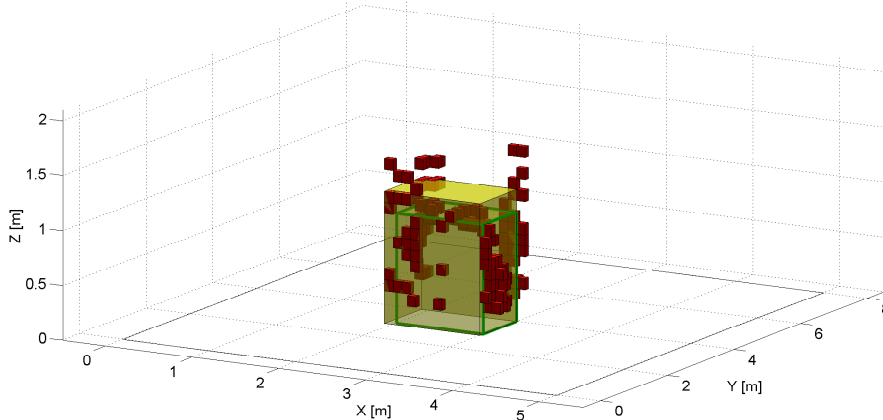


Figure 5.7: 3D image of a metal box of  $1.00 \text{ m}^3$  in the middle of the surveillance area with scattering  $S = 0.2$ . APVC method.

Table 5.1: Volume derived after FOS algorithm

Box volume [ $\text{m}^3$ ]	Position	S	APVC [ $\text{m}^3$ ]	ASVC [ $\text{m}^3$ ]
5.83	in the middle	0.3	6.50	5.72
1.00	in the middle	0.3	1.45	1.58
1.00	in the corner	0.3	1.44	0.95
1.00	in the middle	0.2	1.48	1.63
0.34	in the middle	0.3	0.24	0.18

the output section, while, in the case of presence of the amplitude limiter, it was performed by the low noise amplifier located at the front-end.

The 3D imaging approach described in section 4.4 has then been applied to the signals coming at the output of the UWBoF links, for obstacles having different volumes placed either at the center or at a corner of the surveillance area. Figs. 5.8 and 5.9 refer respectively to obstacles of volumes 1 and  $0.34 \text{ m}^3$ . It can be preliminarily noted that in both cases, when the length of the fiber span increases, the effect of the impairments of the link tend to determine an overestimation of the dimensions of the obstacle. This constitutes a minor problem, in case the obstacle is present, but can determine a situation of false alarm in case its dimension should require not to consider it as a danger. However, the distances at which a false alarm is generated (see again Fig. 5.9) are around  $60, 70 \text{ km}$ , depending on the position of the obstacle, in the configuration with clipping and preamplification, while they are reduced to

Table 5.2: Quantities utilized in the simulation of the *RoF* link

<i>DFB</i> specifics:	
bias current	70 mA
threshold current	15 mA
P-I slope	0.1 mW/mA
IIP2	43 dBm
IIP3	33 dBm
RIN	-160 dB(1/Hz)
<i>PIN</i> Responsivity	1 mA/mW
Noise Figure of Receiver RF Amplifier	3 dB
Noise Figure of LNA	0.5 dB

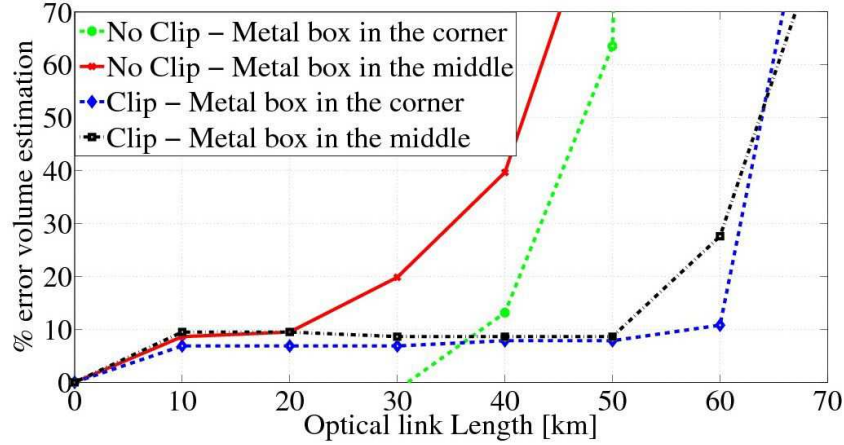


Figure 5.8: Error estimation in the volume computation of a metal box of  $1 \text{ m}^3$  in the surveillance area.

still acceptable values of around 30, 40 km in the configuration with the simplified electronic front-end. Choosing a value of 75% for the maximum acceptable relative error in the estimation of the obstacle volume when it is present, the same limitations in the fiber span length can be derived from the observation of Fig. 5.8. Simulations performed considering obstacles of greater dimensions give the same or even greater values for the maximum distances that can be covered by the UWBoF link. It is worth noticing that the laser non-linearities have practically shown no detrimental effects on the signals at the output of the UWBoF link. In addition to this, the

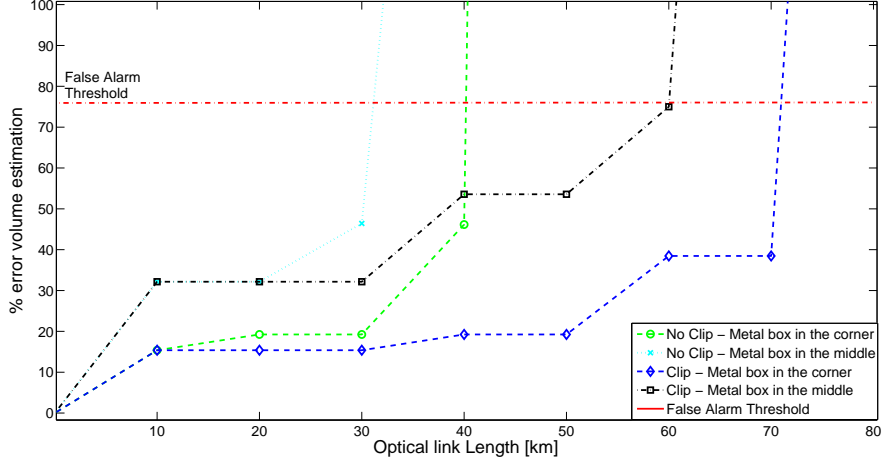


Figure 5.9: Error estimation in the volume computation of a metal box of  $0.34 \text{ m}^3$  in the surveillance area.

Table 5.3: Object volume estimation capabilities in different configurations without clipping operation.

Box Volume [ $\text{m}^3$ ]	Position	Classical Approach [ $\text{m}^3$ ]	FOS [ $\text{m}^3$ ] for different RoF links				
			0 km	10 km	20 km	30 km	50 km
5.83	middle	$> 10$	6.49	6.52	6.52	6.53	11.01
1.00	middle	$> 10$	1.14	1.14	1.14	1.16	3.15
1.00	corner	$\approx 10$	1.23	1.28	1.23	1.12	13.45
0.34	middle	$> 1$	0.24	0.37	0.37	0.41	1.13

impairments due to the noise of the link, which ultimately give the limitations to its length, are mitigated by the fact that an averaging operation has been put into account at the post processing stage. Indeed, for the generic  $i$ -th antenna, the sequence of the eight received signals  $W_{i,1}(t), W_{i,2}(t), \dots, W_{i,8}(t)$ , whose total duration is  $90 \text{ ns}$ , is continuously generated. The post processor located at the fusion node is then able to perform an average over a high number (1000 in this case) of repeated measurements, determining a progressive reduction of the impact of the noise contributions.

## Chapter 6

# Experimental Results

In this section the feasibility of FOS hybrid approach by using the available commercial hardware is provided. Detecting the presence of the object in the correct position by using the UWB commercial devices was the goal of the experimental measurements, as a milestone to build a really full prototype. Experimental results have involved and tested only pieces of the algorithm approach due to limited number of sensors available in laboratory.

Signal data collected using the Time Domain (TD) UWB commercial devices are post-processed to create a point map representing the presence of obstacles.

Specifically, the PhD experimental activity was scheduled as follows:

- A. **Validation using the mono-static radar.** The first step was to demonstrate the goodness of the measurements obtained with the mono-static configuration as a fundamental step to build the UWB multi-static radar prototype exploiting the FOS algorithm. The prototype set up involved a sensor collecting backscattered signals from the environments and subtracting the reference scenario to the signal generated when an obstacle is present, implementing a clutter removal process. After understanding and solving some problems typical of mono-static radars, blind zone and cross-talk antenna effect, this simple configuration performed pretty well and it was possible to clearly see the presence of the target, when it was present, as illustrated in section 6.2.
- B. **Validation using the bi-static radar.** After the mono-static validation, I built up the bi-static configuration as subsequent step. The bi-static configuration presented a new challenge with respect to the mono-static one, i.e., how to reproduce a portion of the FOS algorithm that requires the full syn-

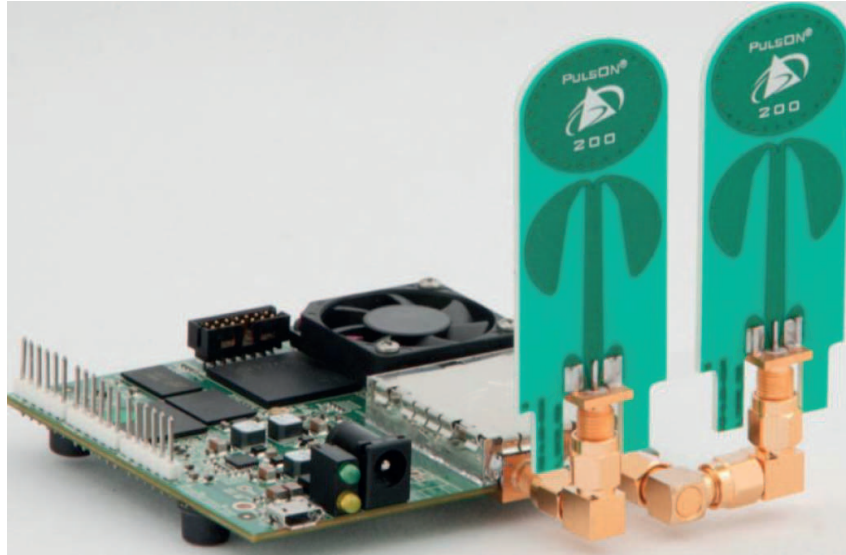


Figure 6.1: P410 RCM device with Broadspec antenna

chronization of sensors. In particular, signals have to be aligned in time to take into account the starting time of the transmission (leading edge) and the cross-correlation among signals. All these effects can cause large detection errors if improperly compensated. The results are shown in section 6.3.

- C. **Test of a new firmware for multi-static radar measurement.** During the bi-static validation, a new firmware in the beta version is used that allows to collect data in mono-static and bi-static way at the same time was used.

## 6.1 Time Domain devices

The devices used in experimental validation are TD PulsON 410 Ranging and Communications Module (P410 RCM) [4]. The P410, shown in Fig. 6.1, is an UWB radio transceiver and/or radar sensor that mainly provides:

- Accurately and reliably measures of the distance between two devices also in high multipath and high clutter environments;
- Wireless channel impulse response (CIR) measurements;
- Two different range measurement techniques (Two-Way TOF and Coarse Range Estimation) with highly precision;

Table 6.1: P410 characteristics

Dimensions (with mounting feet):	76 x 80 x 19 mm
Weight	58 grams
Operating Temperature	0 °C to 75 °C
Input Power Range	5.75 V to 30 V DC
Maximum Power Consumption	4.2 Watts
Operating Band	3.1 GHz to 5.3 GHz
Center Freq	4.3 GHz
Transmit power (standard)	-31.6 to -12.64 dBm
Noise Figure:	4.8 dB
Pulse index integration	1, 16, 64, 1024, 32768
Transmit Pulse Repetition Rate	10.1 MHz (default)

- Data Communication between two or more P410s;
- Operation as a mono-static radar;
- Operation as hybrid device that is both a ranging radio and a radar sensor;
- RF transmissions from 3.1 GHz to 5.3 GHz, with center at 4.3 GHz;
- UWB chipset enables low cost, small size, and low power operation.

Table 6.1 summarizes the P410 specifications and key performance parameters.

As can be noted, the P410 has been designed to be in compliance with the FCC regulations both UWB hand-held systems also known as "battery powered devices" and UWB surveillance systems. For this reason we have selected TD devices to build the partial multi-static radar prototype.

## 6.2 Mono-static Measurements

The quality of measurements obtained with the mono-static configuration is described in this section.

All the system prototype is tested in the laboratory of the University of Bologna as shown in Fig. 6.2.



Figure 6.2: An example of prototype in the laboratory

### 6.2.1 Mono-static Setup

Measurements involve the use of the Monostatic Radar Module (MRM) explained in the Appendix B.1 to collect signal data and manipulate the configuration parameters of TD commercial devices as UWB mono-static radar sensor.

The main parameter manipulated to perform mono-static measurements is the *Pulse Integration Index (PII)* which allows to integrate multiple scans and thereby improve the received SNR but also the amount of time to take a scan consequently increases. Therefore the *Interval (ms)* between subsequent scans has to be properly setted.

The PII, acquisition window and Interval between subsequent scan are set to 15, 100 *ns* and 500 *ms* respectively. The acquisition window is selected in such a way as to take into account the greatest backscattered two-way TOF according with the laboratory dimension. The *Maximum Transmit Gain* represents the transmitted power supported by the device which is selected equal to 63 (the maximum). The sensor is positioned at an height of 0.55 *m* on a tripod as shown in Figure 6.3.

The collected backscattered UWB signals are post-processed in Matlab according to the following steps:

- A. **Cross-talk antennas suppression.** The two antennas (Transmit on Antenna A, Receive on Antenna B) mounted on the device board were very closed



Figure 6.3: Mono-static prototype in the laboratory

together and the amplitude of the direct path pulse saturated the electronic front-end of the device. To counteract this effect the first  $9\text{ ns}$  of the received UWB signal  $s(t)$  are deleted (i.e., time gating).

- B. **Start Transmission Delay Shifting.** The electronic front-end of commercial device starts transmitting after an activating period which is not ideal (no zero). At this step, the implemented Matlab script removes others  $\Delta = 11\text{ ns}$ . For example, a signal variation at  $23\text{ ns}$  represents an obstacle at distance equal to  $1.80\text{ m}$  which corresponds at two-way TOF equal to  $12\text{ ns}$ . At the end of this step the signal can be represented as  $s(t - \Delta)$ .
- C. **Filtering** All the collected signals are band-pass filtered in the  $[3 - 5]\text{ GHz}$  to remove all interferences caused by systems operating in the near frequencies, e.g. WiFi. An ideal rectangular filter is implemented obtaining the signal  $r(t) = s(t - \Delta) * g(t)$  where  $g(t)$  is the filter impulse response.
- D. **Baseband Conversion.** To simplify the subsequent radio stages and make the algorithms less sensitive to synchronization errors the signal is baseband converted through  $x(t) = (F[r(t) * \cos(2\pi f_0 t)]^2 + (F[r(t) * \sin(2\pi f_0 t)])^2)$ , where

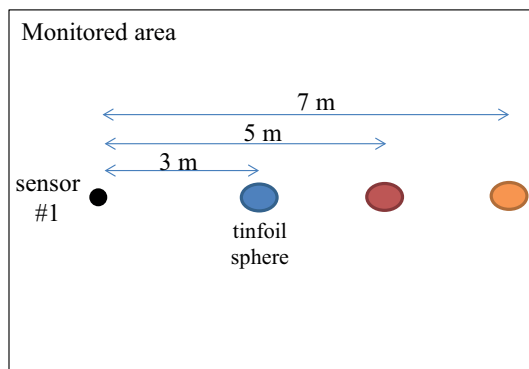


Figure 6.4: Mono-static measurement set up

$F[\cdot]$  indicates a low-pass filtering operation with bandwidth equal to the half-bandwidth of the signal.

- E. **Signals Synchronization.** The UWB signals recorded in the reference and scan scenarios are aligned depending on their correlation value reducing the possible shifts introduced by the operations of the front-end device.
- F. **Empty-room Clutter Removal.** Subtracting the signals obtained in the reference scenario (empty-room) to the signal generated when an obstacles is present. Assuming  $\check{x}(t)$  the signal obtained in the reference scenario and  $x(t)$  the signal obtained when obstacle is present, the clutter removal signal is equal to  $c(t) = x(t) - \check{x}(t)$ .

### 6.2.2 Mono-static measurement results

In order to assess the mono-static system capability to detect the obstacle presence I performed several measurements. First of all, I collected signal in the reference scenario (empty monitored area) at different times to verify the time-variant UWB propagation channel. Every 10 minutes a empty reference scenario signal was collected in an half a hour. Then, I placed at different distances, a little sphere covered by tinfoil (see Figure 6.4 with the aim to identify the contribution due to its presence in the clutter removed UWB signals, along the time axis.

In Fig. 6.5 the clutter removal results are shown where the reference scenario is subtracted to signals obtained when sphere is present at different distances. In this case the scan scenario signals were collected immediately after the measurement of the last reference scenario (less than 10 minutes). Here, it is evident the importance of filtering the signal. In fact, if the filter is applied, in the clutter removal operation

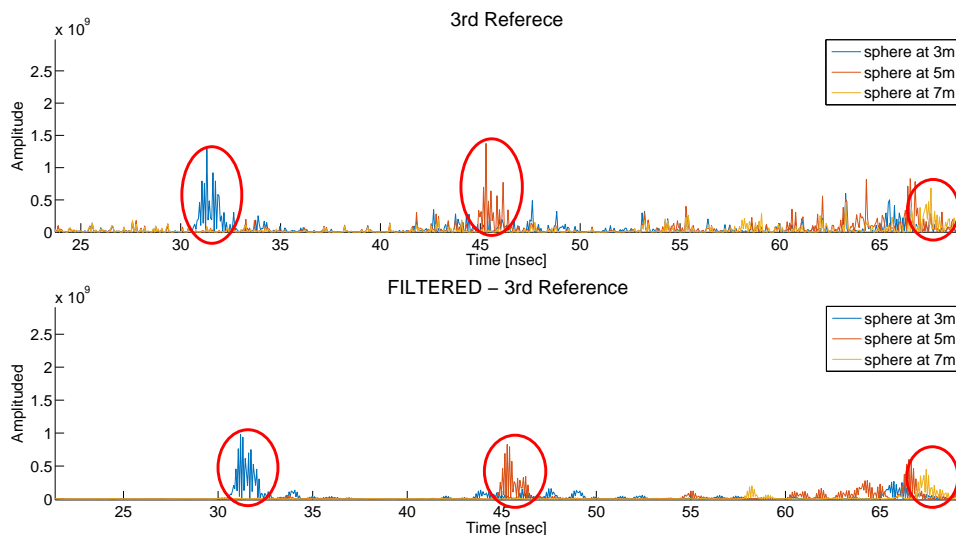


Figure 6.5: Filtering effects on the clutter removal with the 3rd reference signal

the reference signal suppression is quasi-ideal since the resulting UWB signal does not have residual variation due to noise/interference contributions. In particular, we can note that in *FILTERED - 3rd Reference* signals of the Fig. 6.5 the first 40 ns of the clutter removal returns signals equal zero.

In both Figures 6.5, we can clearly note the contribution of the sphere covered by tinfoil at relative TOF (red ellipses). Contributions appear at TOF equal to 31.1, 45.6 and 66.2 ns which correspond to distances of 3, 5, 7 m respectively. The time axis takes into account delays due to both the 9 ns of the cross-talk antennas and the 11 ns of the non-ideal start transmission, in addition to the two-way TOF along the scan period. Moreover, it is possible to note that several contributions due to multipath arise along the scan period but their amplitudes are negligible w.r.t. the first obstacle contribution.

In Fig. 6.6 the time-variance of UWB propagation channel is shown by comparing two different reference scenarios collected with an half a hour of time gap. The *FILTERED - 3rd Reference* figure represents the clutter removal process with the reference scenario collected closed (in time) to the signal generated when the sphere is positioned in the scenario. Here, it is clear that before the first 30 ns no variation between signals is present. Instead, in the *FILTERED - 1rd Reference* figure where the reference scenario is collected half a hour before to the scanning period (where the sphere is placed inside the scenario) shows some little variation in the first 30 ns

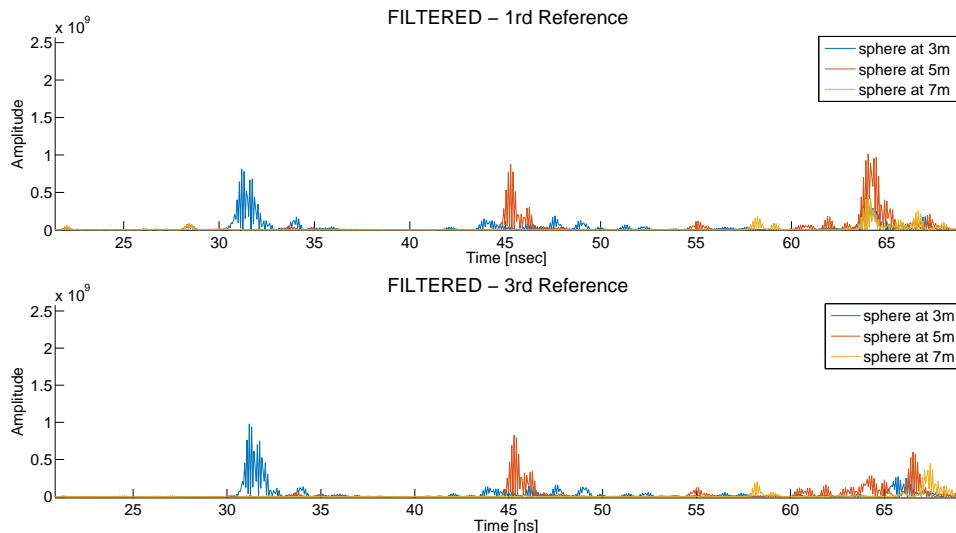


Figure 6.6: Time-variance effects on the clutter removal with 1st and 3rd reference signal

of the time axis. In addition, we can note that between the two Figures 6.6 (at the top and at the bottom) little amplitude variations are present along all the time axis to represent the time-variance of UWB propagation channel.

### 6.3 Bi-static Measurements

The bi-static prototype configuration tested in the laboratory involves 2 sensors at an height of  $0.55\text{ m}$  spaced apart of  $6\text{ m}$ , as shown in Fig. 6.2. Now, the backscattered signal records registered in logfiles refer to the transmission by sensor 1 and reception by sensor 2 and viceversa.

According with the CAT software explained in Appendix B.2, the Acq Index (which determines the operating range at which transmissions can be acquired), acquisition window and Interval are set to 11,  $100\text{ ns}$  and  $500\text{ ms}$  respectively. Maximum Transmit power (Transmit Gain equal to 63) is allowed with Index Integration (PII) selected coherently with Acq Index (Auto Integration is disabled). The acquisition window is selected in such a way to take into account the greatest backscattered two-way TOF according with the laboratory dimension.

### 6.3.1 Bi-static Setup

The collected backscattered UWB signals are post-processed in a similar way as mono-static case. Steps are the following:

- A. **Start Transmission Delay Shifting.** The electronic front-end of commercial device in bi-static mode starts transmitting after an activating period which is not ideal (no zero) but equal to  $\Delta = 7 ns$ . The signal can be represented as  $s(t - \Delta)$ .
- B. **Filtering.** As for the mono-static procedure, all the collected signals are band-pass filtered in the  $[3 - 5] GHz$  to remove all interferences caused by systems operating in the near frequencies, e.g. WiFi. An ideal rectangular filter is implemented obtaining the signal  $r(t) = s(t - \Delta) * g(t)$  where  $g(t)$  is the filter impulse response.
- C. **Leading Edge Alignment.** As explained in Appendix B.2 the leading edge,  $l_e$ , is an approximate measure of when the receiver sensor hooks the considered transmitted waveform. Here, depending of this quantity the collected signal is shifted to the right TOF corresponding to the TOF direct path between sensors,  $r(t - \tau_{l_e})$ .
- D. **Baseband Conversion.** To simplify the subsequent radio stages and make the algorithms less sensitive to synchronization errors the signal is baseband converted through  $x(t) = (F[r(t - \tau_{l_e}) * \cos(2\pi f_0 t)]^2 + (F[r(t - \tau_{l_e}) * \sin(2\pi f_0 t)])^2$ , where  $F[.]$  indicates a low-pass filtering operation with bandwidth equal to the half-bandwidth of the signal.
- E. **Signals Synchronization** Reference and Scan UWB signals are aligned depending on their correlation value reducing the possible shifts introduced by the operation of the front-end device.
- F. **Empty-room Clutter Removal.** Subtracting the reference scenario to signals generated when an obstacle is present (called "scan scenario"). Assuming  $\check{x}(t)$  the signal obtained in the reference scenario and  $x(t)$  the signal obtained when obstacle is present, the clutter removal signal is equal to  $c(t) = x(t) - \check{x}(t)$ .

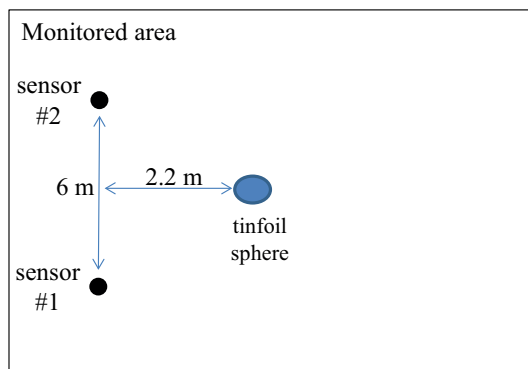


Figure 6.7: Bi-static measurement set up

### 6.3.2 Bi-static Measurements results

As for the mono-static case, in order to assess the capability of the bi-static configuration to detect the presence of the obstacle I performed some measurements. Different reference scenarios (in half an hour) and scans with the obstacle (sphere) in several positions are collected (see Figure 6.7).

First of all, Figure 6.8 shows the reference scenario (green line) and the resulting signal after the signals synchronization step when a sphere is placed at 2.2 m. Here, we can note perfect TOF matching between the direct path components of two considered signals. Moreover, a little variation in the scanned signal (dash blue line) due to the presence of an obstacle is present around 32.4 ns. By considering the  $\Delta = 7$  ns delay of the electric front-end, the TOF direct path  $d_{direct\ path}/c = 20$  ns (where  $c$  is the speed of light); the relative TOF of the replica generated by the presence of the sphere arises at the corresponding distance of  $(TOF_{replica} - \Delta - t_{direct\ path}) \cdot c = 2.3$  m. Comparing the real position to the relative TOF of the replica in a bi-static configuration, it appears to work properly.

As stated before, the variation due to the presence of the sphere seems to be small compared to the amplitude of the direct path between the two sensors since the direct path pulse is much stronger than the multipath component. Actually the sphere contribution is quite remarkable as we can see in figure 6.9 after the clutter removal step where clutter suppression is almost perfect. Here, the output signal is almost zero except in proximity of obstacle contribution, as desired. So the presence of a sphere resulted to be clearly identified during the measurement campaign.

We can conclude that also in this case the principle of FOS can be further analyzed to build a prototype with 4 sensors to validate a lateral object volume

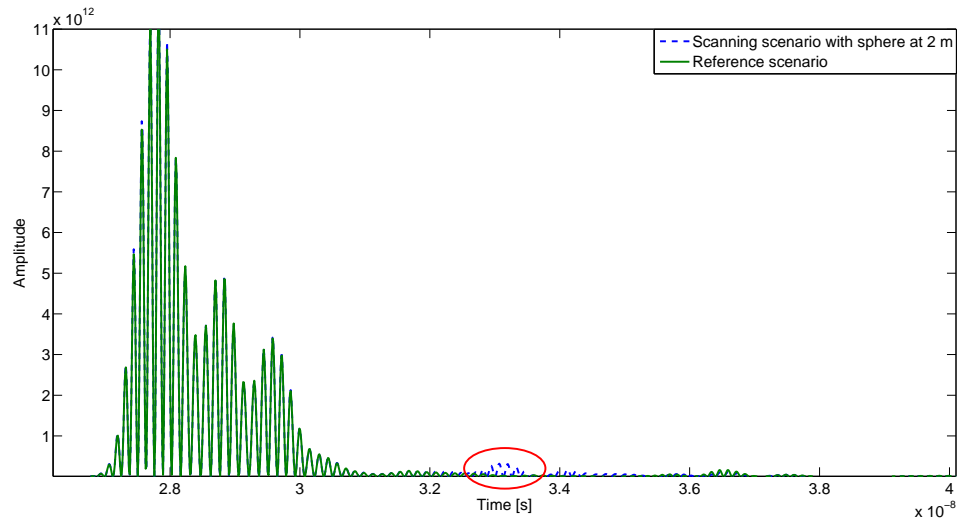


Figure 6.8: Clutter removal with the 1st and 3rd reference signal

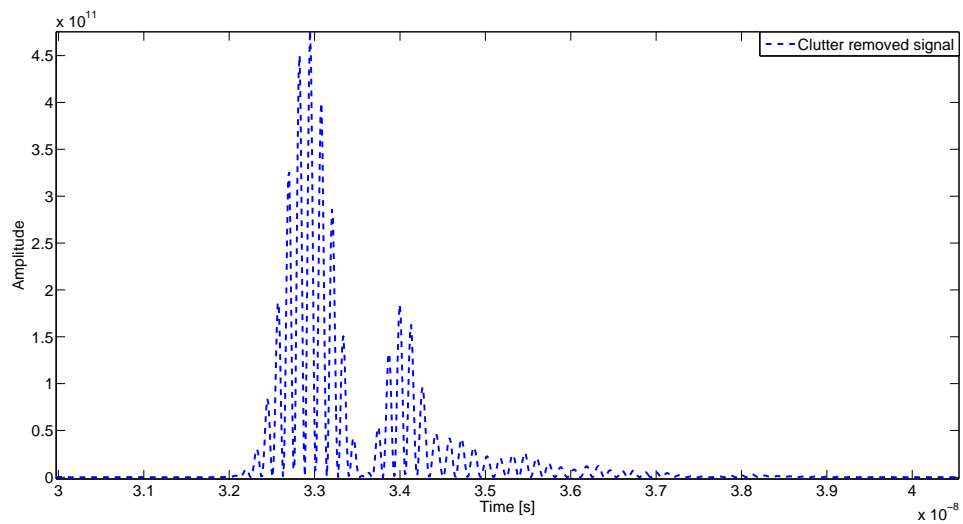


Figure 6.9: Clutter removal with the 1st and 3rd reference signal

estimation.

## 6.4 Multi-static radar Measurements

The multi-static prototype configuration tested in the laboratory involves 4 sensors: 2 at the height of 0.55 m and 2 at the height of 1.3 m spaced apart of 6 meters, as shown in Fig. 6.2. The backscattered signal records registered in logfiles refer to

Table 6.2: Transmission and reception by sensors

<b>Transmitter</b>	<b>Receivers</b>
sensor 1	sensor 1 sensor 2 sensor 3 sensor 4
sensor 2	sensor 1 sensor 2 sensor 3 sensor 4
sensor 3	sensor 1 sensor 2 sensor 3 sensor 4
sensor 4	sensor 1 sensor 2 sensor 3 sensor 4

the transmission and reception by all sensors simultaneously (both mono-static and bi-static configurations) as summarized in Table 6.2. Here, only the transmission by sensor 1 and reception by sensor 2 and viceversa are considered for brevity.

According with the new firmware, separate start and stop time for mono-static (acquisition windows equal to  $[0, 99000]$   $ps$ ) and bi-static (acquisition windows equal to  $[-35000, 64000]$   $ps$ ) scanning are setted. The same resolution and pulse integration values are used as in bi-static measurements.

#### 6.4.1 Multi-static Setup

The collected backscattered UWB signals are post-processed as in the bi-static case. Therefore, the script procedure involve the same steps described in section 6.3: Start Transmission Delay Shifting, Filtering, Leading Edge Alignment, Baseband Conversion, Signals Synchronization and Empty-room Clutter Removal.

#### 6.4.2 Multi-static Measurements results

Multi-static measurements have underlined some problems in order to detect the presence of an obstacle in the laboratory. Different reference scenarios (in half an hour) and scans with the obstacle (sphere) in several potions are collected (in similar configuration as depicted in Figure 6.7).

First of all, Figure 6.10 shows two signals (transmission by sensor 1 and reception by sensor 2) of the reference scenario took with the time gap of 10 minutes. Around  $32 ns$  it is evident a amplitude difference in the direct path pulse of the two signals. This difference can be better understood when the clutter removal step is performed. In particular, in Figure 6.11 it is illustrated clutter removed signals obtained from the resulting signal (after the signals synchronization step) when a sphere is placed at  $2.2 m$  with the subtraction of the aforementioned two signals of the reference scenario. The signal variation attended around  $5 ns$  later to the TOF of the direct

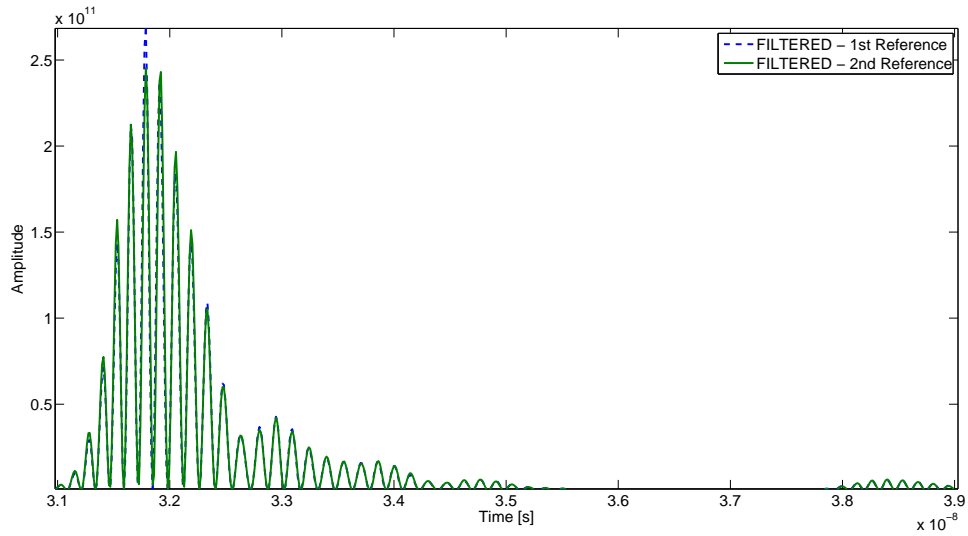


Figure 6.10: Amplitude variation in the direct path pulse with the 1st and 3rd reference signal

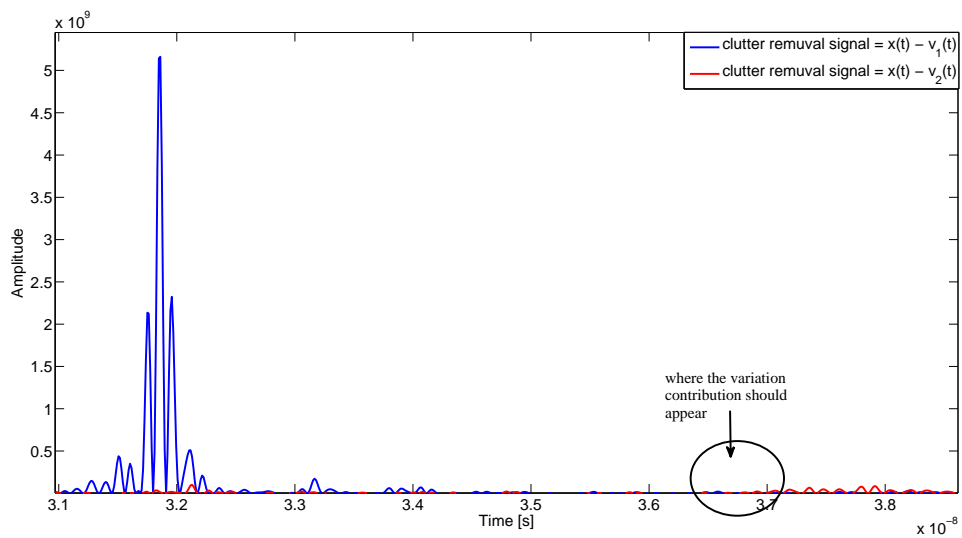


Figure 6.11: Error in the Clutter removal with the 1st and 3rd reference signal

path does not appear (missing sphere contribution) and moreover, the variation due to the difference between two direct paths is too strong with respect to others variations along the time axis.

This result characterized all measurements made with any TX-RX couples considered.

Results obtained with multi-static configuration have shown some difficulties in order to detect obstacle (sphere) in the laboratory. Unfortunately, there was not enough time to further investigate the unexpected behaviours of sensors.

Errors can be related to:

- A. amplitude variations due to amplifiers and RF front end, saturation and non-idealities;
- B. errors in synchronization.

## Chapter 7

# Conclusions

In this dissertation the problem of increasing the protection of *Level crossing (LC)* to guarantee a given level of safety was investigated. First of all, normative frameworks adopted in the World and with particular attention to the Europe were described by providing efforts and concepts, as *common safety targets* and *common safety methods*. This constitutes the basis for an high-speed and safe interoperable Trans-European rail network where LC are one of the most critical points.

Among all possible feasible solutions compliant with EU safety requirements against LC accidents and/or trapped obstacles (like vehicles) in the LC area to prevent collisions with train, the most suitable countermeasure is the adoption of monitoring systems to control unauthorized access, called **Integrated Automatic Protection (PAI-PL)** by the Italian rail operator.

Current technologies candidate to guarantee the LC safety with respect to the main requirements (as promoted in CENELEC EN 50126) in terms of reliability, availability, maintainability and safety were discussed together with their advantages and limitations. Particular attention was given to the system designed in this Thesis based on partial ultrawide-band (UWB) multi-static radar introduced in section 1.3.

In order to assess the idea of UWB technology as a good candidate for LC surveillance systems, a preliminary analysis about properties of obstacles backscattering was performed in a reference LC-like scenario and for a wide frequency range. This study was performed with the aid of 3DSCAT ray tracing (RT) simulator.

The proposed UWB partial multi-static radar for railway crossings surveillance, able of detecting, localizing and estimating the obstacle volume, even in static conditions, and makes use of a fixed set of sensors to obtain the information about the volume of the obstacle thus discriminating between large or small obstacles. The

developed detection algorithm (in section 4.4), namely fixed object scanner (FOS), performs a sequence of scanning phases and can be considered as an hybrid approach combining the UWB multi-static radar and the mono-static imaging scanner configurations. As a consequence, it allows for gaining some of the advantages of both configurations and at the same time can mitigate their drawbacks.

The adoption of the radio-over-fiber (RoF) technique for the centralized processing of several UWB partial multi-static radar far from LC area has been proposed in chapter 3. Two UWBoF solutions has been studied, and compared in section 5.3, which combine proper processing of UWB signal and backhauling over the already deployed optical fiber backbone. The proposed method has shown its advantages in the simulation results , allowing to remotize the post-processing of several LCs up to tens of kilometers.

The results reported by this first study of a surveillance system based on UWB multi-static radar highlight some interesting problems when considering real propagation conditions and 3-D scenarios (see section 5.1). While in the literature most of results have been presented for ideal point obstacles and it is claimed that at most 4 receivers are sufficient for a reliable detection and localization, here we have seen that with realistic obstacles the scattering characteristics play a fundamental role. In fact, when scattering is almost absent and under certain conditions of reflection, the localization of obstacles might suffer from discrimination ambiguities. Therefore, for a more accurate obstacle image reconstruction, the classical 4-receivers configuration must be enhanced with the introduction of additional receivers/transmitters.

This is the reason why the idea of FOS algorithm was investigated to develop a partial multi-static UWB radar for railway crossings surveillance capable of detecting and localizing obstacle and its volume, even in static conditions, through 3D imaging. To mitigate the ambiguity effects arising when forming the 3D image, the proposed FOS algorithm performs different scanning phases, where only a suitable subset of nodes are active at each phase and a binary hypothesis test is conducted for each 3D pixel. The preliminary simulation results obtained, through the 3DSCAT RT simulator, encourage the development of the proposed solution toward the experimental validation.

Preliminary experimental results on two simple prototypes in mono-static and bi-static configuration confirm the ability of the system to detect and localize the obstacle in a controlled laboratory environment. In particular, the measurements

shows the ability of UWB radar to recognize the variation on backscattering signals with precision into the scanning period. Moreover, these results partially validate the RT simulation as a tool to give a reliable UWB channel characterisation of real environment. This is shown by the results reported in chapter 6, which are substantially in line with the results previously obtained through RT simulations.

Finally, the experimental results provide the basis to establish the FOS algorithm as a real good candidate for LC surveillance system. We can conclude that the PhD activities gave the foundations to build an effective real surveillance system adoptable in railway sites, compliant both with regulations and functional/technical requirements.

# Appendix A

## RayTracing files

### A.1 Reference Scenario

```
;-*- mode:text; -*-
;numero delle pareti
25
;descrizione delle pareti
;n      x1      y1      z1      x2      y2      z2      x3      y3      z3      x4      y4      z4      tipo_parete
1  0.00  1.50  0.00  5.00  1.50  0.00  5.00  1.60  0.00  0.00  1.60  0.00  rail
2  0.00  2.835 0.00  5.00  2.835 0.00  5.00  2.935 0.00  0.00  2.935 0.00  rail
3  0.00  4.965 0.00  5.00  4.965 0.00  5.00  5.065 0.00  0.00  5.065 0.00  rail
4  0.00  6.40  0.00  5.00  6.40  0.00  5.00  6.50  0.00  0.00  6.50  0.00  rail
5  0.10  -0.10 0.00  -0.10 0.10  0.00  -0.10 0.10  3.00  0.10  -0.10 3.00  poles
6  4.90  -0.10 0.00  5.10  0.10  0.00  5.10  0.10  3.00  4.90  -0.10 3.00  poles
7  5.10  7.90  0.00  4.90  8.10  0.00  4.90  8.10  3.00  5.10  7.90  3.00  poles
8  -0.10 7.90  0.00  0.10  8.10  0.00  0.10  8.10  3.00  -0.10 7.90  3.00  poles
9  0.00  0.00  0.00  5.00  0.00  0.00  5.00  8.00  0.00  0.00  8.00  0.00  asphalt
10 0.00  -0.30 1.00  5.00  -0.30 1.00  5.00  -0.30 1.20  0.00  -0.30 1.20  sbarre_legno
11 0.00  8.30  1.00  5.00  8.30  1.00  5.00  8.30  1.20  0.00  8.30  1.20  sbarre_legno
12 0.00  1.35  0.00  0.26  1.35  0.00  0.26  3.035 0.00  0.00  3.035 0.00  traverse_cemento
13 0.76  1.35  0.00  1.02  1.35  0.00  1.02  3.035 0.00  0.76  3.035 0.00  traverse_cemento
14 1.52  1.35  0.00  1.78  1.35  0.00  1.78  3.035 0.00  1.52  3.035 0.00  traverse_cemento
15 2.28  1.35  0.00  2.54  1.35  0.00  2.54  3.035 0.00  2.28  3.035 0.00  traverse_cemento
16 3.04  1.35  0.00  3.30  1.35  0.00  3.30  3.035 0.00  3.04  3.035 0.00  traverse_cemento
17 3.80  1.35  0.00  4.06  1.35  0.00  4.06  3.035 0.00  3.80  3.035 0.00  traverse_cemento
18 4.56  1.35  0.00  4.82  1.35  0.00  4.82  3.035 0.00  4.56  3.035 0.00  traverse_cemento
19 0.00  4.88  0.00  0.26  4.88  0.00  0.26  6.565 0.00  0.00  6.565 0.00  traverse_cemento
20 0.76  4.88  0.00  1.02  4.88  0.00  1.02  6.565 0.00  0.76  6.565 0.00  traverse_cemento
21 1.52  4.88  0.00  1.78  4.88  0.00  1.78  6.565 0.00  1.52  6.565 0.00  traverse_cemento
22 2.28  4.88  0.00  2.54  4.88  0.00  2.54  6.565 0.00  2.28  6.565 0.00  traverse_cemento
23 3.04  4.88  0.00  3.30  4.88  0.00  3.30  6.565 0.00  3.04  6.565 0.00  traverse_cemento
24 3.80  4.88  0.00  4.06  4.88  0.00  4.06  6.565 0.00  3.80  6.565 0.00  traverse_cemento
25 4.56  4.88  0.00  4.82  4.88  0.00  4.82  6.565 0.00  4.56  6.565 0.00  traverse_cemento

;numero degli spigoli di diffrazione
76
;numero degli spigoli di diffrazione
;
1  0  1.5  0  5  1.5  0  1  1  0
2  5  1.6  0  0  1.6  0  1  1  0
3  0  2.835  0  5  2.835  0  2  2  0
4  5  2.935  0  0  2.935  0  2  2  0
5  0  4.965  0  5  4.965  0  3  3  0
```

6	5	5.065	0	0	5.065	0	3	3	0	
7	0	6.4	0	5	6.4	0	4	4	0	
8	5	6.5	0	0	6.5	0	4	4	0	
9	0	1.35	0	0	0.26	1.35	0	12	12	0
10	0.26	1.35	0	0	0.26	3.035	0	12	12	0
11	0.26	3.035	0	0	3.035	0	12	12	0	
12	0	1.35	0	0	3.035	0	12	12	0	
13	0.76	1.35	0	1.02	1.35	0	13	13	0	
14	1.02	1.35	0	1.02	3.035	0	13	13	0	
15	1.02	3.035	0	0.76	3.035	0	13	13	0	
16	0.76	1.35	0	0.76	3.035	0	13	13	0	
17	1.52	1.35	0	1.78	1.35	0	14	14	0	
18	1.78	1.35	0	1.78	3.035	0	14	14	0	
19	1.78	3.035	0	1.52	3.035	0	14	14	0	
20	1.52	1.35	0	1.52	3.035	0	14	14	0	
21	2.28	1.35	0	2.54	1.35	0	15	15	0	
22	2.54	1.35	0	2.54	3.035	0	15	15	0	
23	2.54	3.035	0	2.28	3.035	0	15	15	0	
24	2.28	1.35	0	2.28	3.035	0	15	15	0	
25	3.04	1.35	0	3.3	1.35	0	16	16	0	
26	3.3	1.35	0	3.3	3.035	0	16	16	0	
27	3.3	3.035	0	3.04	3.035	0	16	16	0	
28	3.04	1.35	0	3.04	3.035	0	16	16	0	
29	3.8	1.35	0	4.06	1.35	0	17	17	0	
30	4.06	1.35	0	4.06	3.035	0	17	17	0	
31	4.06	3.035	0	3.8	3.035	0	17	17	0	
32	3.8	1.35	0	3.8	3.035	0	17	17	0	
33	4.56	1.35	0	4.82	1.35	0	18	18	0	
34	4.82	1.35	0	4.82	3.035	0	18	18	0	
35	4.82	3.035	0	4.56	3.035	0	18	18	0	
36	4.56	1.35	0	4.56	3.035	0	18	18	0	
37	0	4.88	0	0.26	4.88	0	19	19	0	
38	0.26	4.88	0	0.26	6.565	0	19	19	0	
39	0.26	6.565	0	0	6.565	0	19	19	0	
40	0	4.88	0	0	6.565	0	19	19	0	
41	0.76	4.88	0	1.02	4.88	0	20	20	0	
42	1.02	4.88	0	1.02	6.565	0	20	20	0	
43	1.02	6.565	0	0.76	6.565	0	20	20	0	
44	0.76	4.88	0	0.76	6.565	0	20	20	0	
45	1.52	4.88	0	1.78	4.88	0	21	21	0	
46	1.78	4.88	0	1.78	6.565	0	21	21	0	
47	1.78	6.565	0	1.52	6.565	0	21	21	0	
48	1.52	4.88	0	1.52	6.565	0	21	21	0	
49	2.28	4.88	0	2.54	4.88	0	22	22	0	
50	2.54	4.88	0	2.54	6.565	0	22	22	0	
51	2.54	6.565	0	2.28	6.565	0	22	22	0	
52	2.28	4.88	0	2.28	6.565	0	22	22	0	
53	3.04	4.88	0	3.3	4.88	0	23	23	0	
54	3.3	4.88	0	3.3	6.565	0	23	23	0	
55	3.3	6.565	0	3.04	6.565	0	23	23	0	
56	3.04	4.88	0	3.04	6.565	0	23	23	0	
57	3.8	4.88	0	4.06	4.88	0	24	24	0	
58	4.06	4.88	0	4.06	6.565	0	24	24	0	
59	4.06	6.565	0	3.8	6.565	0	24	24	0	
60	3.8	4.88	0	3.8	6.565	0	24	24	0	
61	4.56	4.88	0	4.82	4.88	0	25	25	0	
62	4.82	4.88	0	4.82	6.565	0	25	25	0	
63	4.82	6.565	0	4.56	6.565	0	25	25	0	
64	4.56	4.88	0	4.56	6.565	0	25	25	0	
65	0	-0.3	1	5	-0.3	1	10	10	0	
66	5	-0.3	1.2	0	-0.3	1.2	10	10	0	
67	0	8.3	1	5	8.3	1	11	11	0	
68	5	8.3	1.2	0	8.3	1.2	11	11	0	
69	-0.1	0.1	0	-0.1	0.1	3	5	5	0	
70	0.1	-0.1	0	0.1	-0.1	3	5	5	0	
71	4.9	-0.1	0	4.9	-0.1	3	6	6	0	
72	5.1	0.1	0	5.1	0.1	3	6	6	0	
73	5.1	7.9	0	5.1	7.9	3	7	7	0	

```

74 4.9 8.1 0 4.9 8.1 3 7 7 0
75 -0.1 7.9 0 -0.1 7.9 3 8 8 0
76 0.1 8.1 0 0.1 8.1 3 8 8 0
0
0

```

## A.2 Run Time File and auxiliary parameters

```

function RT_run_main_PALPL()

clear all;
close all;

for N_RUN = 2 : 2
    %% Create a new simulation or select a scenario already created
    %% This function call the "create_scenarios" function to generate a new
    %% scenario...
    %%... inside there are also functions which update the DataBase of
    %%scenarios, RX and TX antennas already simulated!!!
    [pars, PW_tx, f0_tx, temp, lx, ly] = Create_Load_Scenario(N_RUN);

    %% RAYTRACING
    pars.make_new_simulation=1;    % set pars.make_new_simulation to 1 to make a new Ray Tracing simulation
                                   % set pars.make_new_simulation to 0 to post-process a previously done simulation
                                   % and
                                   % to plot graphs (simulation output files , marked with 'pars.run_name', must
                                   % exist
                                   % in ./OUT directory)

    pars.enable_graph_visualization=1; % set to 1 to plot graphs (e.g. power, delay spread, angle spread, and so on)
    pars.enable_map_rays_visualization=1; % set to 1 to plot the simulation scenario and the rays (pay attention, do not
    enable it for big simulations with many receivers and many interactions enabled!!)

    pars.OUTPUT_path='OUT'; % path of the simulation output files

    pars.INPUT_path=fullfile('INPUT','scenarios','PALPL'); % path of the considered input scenario

    pars.ELEMENTS_FILE='PALPL.list'; % input file 2: walls electromagnetic parameters

    pars.TX_Path=fullfile('INPUT','scenarios','PALPL'); % path of the considered tx file
    pars.TX_number=8; % number of tx (usually 1): it must be set manually

    pars.RX_Path=fullfile('INPUT','scenarios','PALPL'); % path of the considered rx file
    pars.RX_number=GetRxNumber(fullfile(pars.RX_Path,pars.RX_FILE)); % this script automatically gets the number of
    receivers from Rx file
    pars.exe_path='EXE_FILE'; % path of the RT executable
    pars.exe_scattray='RT_indoor.exe'; % name of the RT executable

    pars.POSTPROCESSING_SCRIPTS_path='POSTPROCESSING_SCRIPTS';
    pars.enable_selective=0;    % set to 1 to select only some ray types before plotting the results

    pars.current_RX_Pos=1; % set the Rx index corresponding to the power-delay profile displayed in graphs

    pars.inverted=0;    % set to 1 if you want to reverse the Rx order in Rx route

    %% In the following, the RT simulation parameters are set
    pars.param_file= fullfile (pars.exe_path, 'param.dat');
    fid = fopen(pars.param_file, 'w');
    fprintf (fid, '%s\t%s\n', 'DEBUG', '0'); % do not change this parameter
    fprintf (fid, '%s\t%s\n', 'VERBOSE_RAY', '1'); % do not change this parameter
    fprintf (fid, '%s\t%s\n', 'SAVE_MR', '1'); % do not change this parameter

```

```

fprintf(fid, '%s\t%s\n', 'WALLS_MAP', '1'); % do not change this parameter
fprintf(fid, '%s\t%s\n', 'EDGES_MAP', '1'); % do not change this parameter
fprintf(fid, '%s\t%s\n', 'HOLES_MAP', '1'); % do not change this parameter
fprintf(fid, '%s\t%s\n', 'TX_RX', '1'); % do not change this parameter
fprintf(fid, '%s\t%s\n', 'ANTENNA', '1'); % do not change this parameter
fprintf(fid, '%s\t%s\n', 'BSP_TREE_MAX_DEPTH', '15'); % do not change this parameter
fprintf(fid, '%s\t%s\n', 'BSP_NODE_MAX_ELEMENTS', '100'); % do not change this parameter
fprintf(fid, '%s\t%s\n', 'COHERENT_MODE', '1'); % do not change this parameter
fprintf(fid, '%s\t%s\n', 'COHERENT_SCAT', '0'); % do not change this parameter
fprintf(fid, '%s\t%s\n', 'PATTERN_EXTRAPOLATION', '0');
fprintf(fid, '%s\t%s\n', 'ENHANCED_REFL_TRANSM_COEFF', '1');
fprintf(fid, '%s\t%s\n', 'ENABLE_SCAT_FAR', '1'); % set to 1 to enable diffuse scattering from "far objects"
fprintf(fid, '%s\t%s\n', 'UTD_DIEL', '0'); % set to 1 to enable heuristic diffraction coefficients for dielectrical
    wedges (otherwise, UTD is used)
fprintf(fid, '%s\t%s\n', 'ENABLE_SCAT_TX', '1'); % set to 1 to enable diffuse scattering at Tx side
fprintf(fid, '%s\t%s\n', 'ENABLE_SCAT_RX', '1'); % set to 1 to enable diffuse scattering at Rx side (pay attention,
    do not enable it if you have many receivers!)
% The 2 following parameters are related to the size of the "scattering tiles": increase t% number of scattering ray
    subdivisions in elevation (the elevation scattering resolution is: (theta_max-theta_min)/scat_n_theta )oheir
    values to use smaller scattering tiles
fprintf(fid, '%s\t%s\n', 'SCAT_N_THETA', '48'); % number of scattering ray subdivisions in elevation (the elevation
    scattering resolution is: (theta_max-theta_min)/scat_n_theta )
fprintf(fid, '%s\t%s\n', 'SCAT_N_PHI', '96'); % number of scattering ray subdivisions in azimuth (the azimuth
    scattering resolution is: (phi_max-phi_min)/scat_n_phi )

% For further details on the following 9 parameters, see the papers:
% 1) V. Degli-Esposti, F. Fuschini, E. M. Vitucci, G. Falciasecca, "Measurement and modelling of scattering from
    buildings", IEEE Transactions on Antennas and Propagation, Vol. 55 No 1, pp. 143-153, January 2007
% 2) F. Fuschini, V. Degli-Esposti, E. M. Vitucci, "A model for forward-diffuse scattering through a wall," in Proc.
    4th European Conference on Antennas and Propagation (EuCAP 2010), Barcelona, Spain, 12-16 April 2010.
fprintf(fid, '%s\t%f\n', 'S_R', 0.3); % scattering parameter (backward scattering only)
fprintf(fid, '%s\t%f\n', 'S_T', 0); % scattering parameter (forward scattering only)
fprintf(fid, '%s\t%s\n', 'SCAT_PATTERN_MODEL', '1'); % '0' to use lambertian scattering pattern, '1' to use
    directive scattering pattern (single or double lobe)
fprintf(fid, '%s\t%f\n', 'SCAT_ALPHA_R', 3.0); % alpha_r is related to the width of the scattering lobe centered on
    the specular reflection (only for scattering pattern '1')
fprintf(fid, '%s\t%f\n', 'SCAT_ALPHA_I', 3.0); % alpha_i is related to the width of the back-scattering lobe (only for
    scattering pattern '1')
fprintf(fid, '%s\t%f\n', 'SCAT_ALPHA_T', 3.0); % similar to alpha_r, but for forward scattering (lobe centered on the
    transmission direction)
fprintf(fid, '%s\t%f\n', 'SCAT_ALPHA_B', 3.0); % similar to alpha_i, but for forward scattering
fprintf(fid, '%s\t%f\n', 'SCAT_K_R', 0.95); % power division between the 2 scattering lobes (only for pattern '1'). Set
    this parameter to 1 to use a single scattering lobe (no back-scattering lobe)
fprintf(fid, '%s\t%f\n', 'SCAT_K_T', 0.95); % similar to the previous parameter, but for forward scattering

fprintf(fid, '%s\t%f\n', 'SCAT_XPOL', 0.05); % scattering XPOL parameter. For further details, see the paper: E. M.
    Vitucci, F. Mani, V. Degli-Esposti, C. Oestges, "Polarimetric Properties of Diffuse Scattering from Building
    Walls: Experimental Parameterization of a Ray-Tracing Model", IEEE Transactions on Antennas and
    Propagation, Vol. 60 No. 6, pp. 2961-2969, June 2012
fprintf(fid, '%s\t%s\n', 'POWER_THRESHOLD_DB', '-500'); % minimum power threshold (in dB-units) for a single
    ray
fprintf(fid, '%s\t%s\n', 'WALL_AREA_MIN', '4'); % do not change this parameter
fprintf(fid, '%s\t%s\n', 'EDGE_LENGTH_MIN', '1'); % do not change this parameter
fprintf(fid, '%s\t%s\n', 'N_MAX_INTERACTIONS', '2'); % maximum total number of interactions allowed (including
    transmissions)
fprintf(fid, '%s\t%s\n', 'N_MAX_REFL', '2'); % maximum number of reflections allowed
fprintf(fid, '%s\t%s\n', 'N_MAX_DIFF', '1'); % maximum number of diffractions allowed
fprintf(fid, '%s\t%s\n', 'N_MAX_REFL_WITH_SCAT', '1'); % maximum number of reflections combined with
    scattering allowed (pay attention, this can dramatically increase the computation time!)
fprintf(fid, '%s\t%s\n', 'N_MAX_DIFF_WITH_SCAT', '1'); % maximum number of diffractions combined with
    scattering allowed (pay attention, this can dramatically increase the computation time!)
fprintf(fid, '%s\t%s\n', 'N_MAX_REFL_AND_DIFF', '2'); % maximum total number of reflections and diffractions
    allowed in a single ray (e.g. if this is equal to 3, you can have at most 2 reflections and 1 diffraction, or 2
    diffraction and 1 reflection in the same ray)
fprintf(fid, '%s\t%s\n', 'N_MAX_TRANSM', '0'); % maximum number of transmissions allowed (usually this number is
    high in indoor environment)
status = fclose(fid);
if (status ~= 0)

```

```

        error('ERROR IN WRITING RAY TRACING PARAMETERS FILE!');
    end

    % Small modifications to take more parameters and process the H(f)
    %%% Multistatic Radar (4 sensor on poles head) %%%
    New_run_execution(pars, PW_tx, f0_tx, temp, l_x, l_y); % this scripts starts the RT simulation and/or post-
        processing
    %%%
    %%% Cooperative Monostatic Radar (each poles have 6 sensors) %%%
    %New_run_execution_BICO_CMR(pars, PW_tx, f0_tx, temp);
    %%%
end

```

## Appendix B

# Software tool for experimental measurements

### B.1 Monostatic Radar Module (MRM)

The Monostatic Radar Module allows manipulating the configuration parameters of TD commercial devices and illustrating their operation as UWB mono-static radar sensors. The MRM provides raw radar scan data to develop detection strategies targeted to a specific application.

When the sensor board is successful connected, the main operating window will open (Fig. B.1). Several messages should appear in the status window at the bottom of the screen with the `Received MRM_GETSTATUSINFO_CONFIRM` final message.

Tab Control (in the upper area) provides access to seven selectable tab pages. The function of each tab is summarized below:

- Configuration: Defines various parameters including integration rate, antenna configuration, and radar scan windows
- Control: Starts and stops radar scanning
- Scan: Displays a live plot of the radar scans including filtered response and detections
- MRM Server: Allows the user to connect to a Windows Service that converts raw radar scans from the MRM into filtered radar scans
- Status Info: Displays software and hardware version numbers as well as MRM board temperature

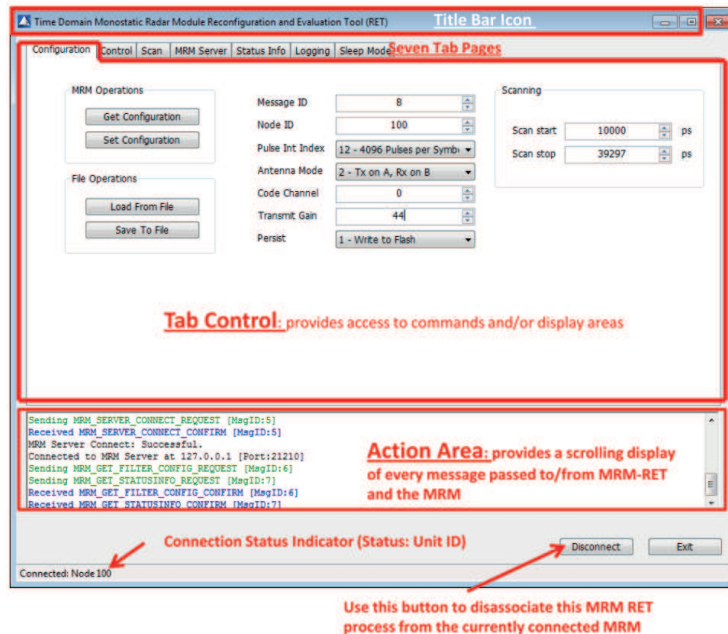


Figure B.1: MRM Configuration screen with indication of the main areas

- Logging: Allows the user to record radar scan data to log files
- Sleep Mode: Allows the user to reduce the power consumption of the radar when it is not in active use.

The bottom part of the window contains the Action Area, which provides scrolling text indication of every message sent to and received from the device.

Successful connection to a device brings up the configuration tab showing the current setted parameters (see Figure B.2). Here, the user can read and write the Node ID, Pulse Integration Index, Antenna Mode, Code Channel, Transmit Gain, Radar Scan Start point, and Radar Scan Stop point. A new configuration is correctly loaded if in the bottom part of the tab appears sequentially the `MRM_SET_CONFIG_REQUEST` and `MRM_GET_CONFIG_CONFIRM` messages after clicking the *Set Configuration* button (adjusting the parameters according to the user needs).

### B.1.1 Configuration of Parameters

The *Pulse Integration Index (PII)* allows coherent operation, it is possible to integrate multiple scans and thereby improve the received SNR. Each time the integration is doubled, an improvement of the SNR of the received signal of 3 dB is experienced but also doubling the amount of time it takes to produce a scan con-

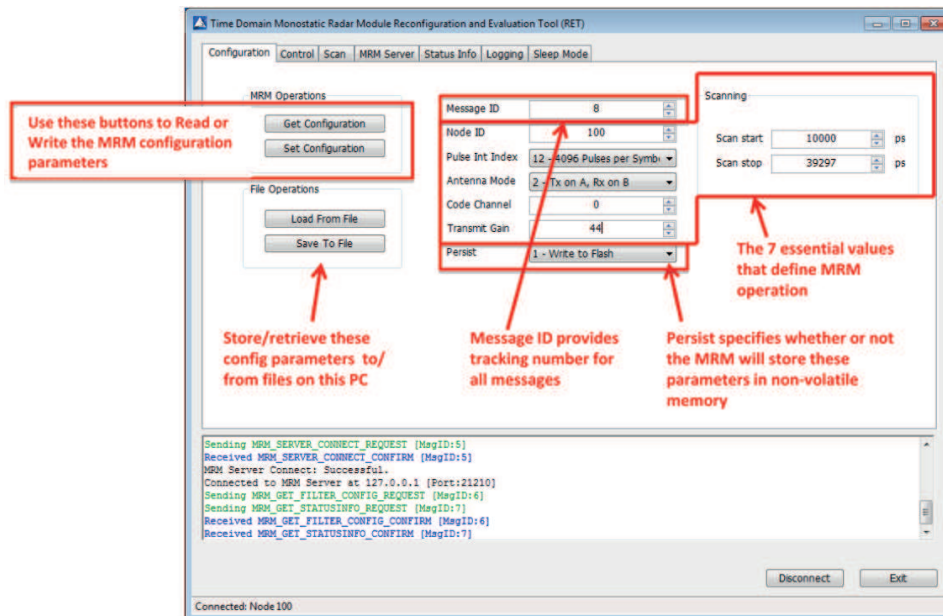


Figure B.2: MRM-RET Configuration Tab

sequently. The minimum integration is  $64 : 1$  (or  $2^6$ ). A PII setting of 6 increases the received SNR by 18 dB. Similarly a PII of 15 (the maximum allowed by MRM) integrates 32.768 scans and thereby provide an SNR improvement of 45 dB. The *Code Channel* parameter guarantees no interference between two or more operating devices in the same vicinity. Code channels are numbered from 0 – 6. *Transmit Gain* when set to zero, the minimum transmitted power supported by the device is used. Setting the transmit gain to a value of 63 the maximum transmitted power is available. *Scan Start* express the starting of signals transmission in picoseconds (ps). The device converts the input values into "bins" where each bin is 1.907 ps. Because this conversion involves rounding, the value shown in Scan Start may not match the value originally entered by the user. For example, setting a Scan Start value to 5000 will actually result in the Scan Start value being set to 4999. *Scan Stop* have the function complementary to Scan Start.

### B.1.2 Logging File

The data collection and post-processing analysis of signals transmitted by the device can be performed through the Logging Tab provided by MRM RET. The logfile is a comma-separated variable ASCII .csv text file in which all messages sent to, and received from, the device are captured in raw. Logfiles is stored in the directory

indicated. An example of logfile is reported in Fig. B.3. Before the first instance of

The screenshot shows an Excel spreadsheet with the following header row (A1 to U1):

A1	B1	C1	D1	E1	F1	G1	H1	I1	J1	K1	L1	M1	N1	O1	P1	Q1	R1	S1	T1	U1																							
Timestamp	Config	NodeId	ScanStartPs	ScanStopPs	ScanResolutionBins	BaseIntegrationIndex	Segment1NumSamples	Segment2NumSamples	Segment3NumSamples	Segment4NumSamples	Segment1AdditionalIntegrati																																
1460983295.872	Config	100	0	0	0	0	0	0	0	0	0	0	0	0	0	0	0	0	0	2	63																						
Timestamp	MrmControlRequest	ScanCount	IntervalTimeMicroseconds																																								
1460983310.302	MrmControlRequest	10	10	500000																																							
Timestamp	MrmControlConfirm	MessageId	Status																																								
1460983310.396	MrmControlConfirm	10	0																																								
Timestamp	MrmFullScanInfo	MessageId	SourceId	EmbeddedTimestamp	Reserved	Reserved	Reserved	Reserved	Reserved	ScanStartPs	ScanStopPs	ScanStepBins	Filtering	AntennaId	Reserved	NumSamplesTotal	ScanData																										
1460983311.425	MrmFullScanInfo	10	100	11801862	0	0	0	0	0	0	99609	32	1	2	1	1632	85	-609	-87	596	26	-402	-235	469	445	345	-440	968	544	905	-750	370	-666	1184	-693	-673	-337	783	-77	-283	274	-205	8

Figure B.3: MRM RET Logfile Format

each message type, a header description will be provided (see Fig. B.3). The initial time-stamp (always the first parameter in each message line) is a floating point time value, in seconds, provided. All parameters for all messages are described in [4].

Manipulating the raw UWB data signals in logfiles it is possible to clearly see the presence of the target, when it was present.

## B.2 Channel Analysis Tool (CAT)

The Channel Analysis Tool (CAT) serves to configure and operate with TD PulsON 410 devices which one the user can generate, capture, display, and log UWB signals in bi-static or multi-static configuration. Since its connecting/configuration process and parameters are very similar to MRM case, only the software peculiarities w.r.t. the mono-static one are explained.

Successful connection to a Radio brings up the Configuration Tab showing the device's current configuration parameters. The parameters are divided into three general groupings: Commands, Parameter Settings, and Communications Statistics (See Figure B.4). This tab provides the user with an easy method for reading and writing the configuration parameters.

The **Command Section** in CAT represented in the bottom of the Fig. B.4, i.e. the *Set Configuration*, *Get Configuration* and *Start/Stop Radio* have the same

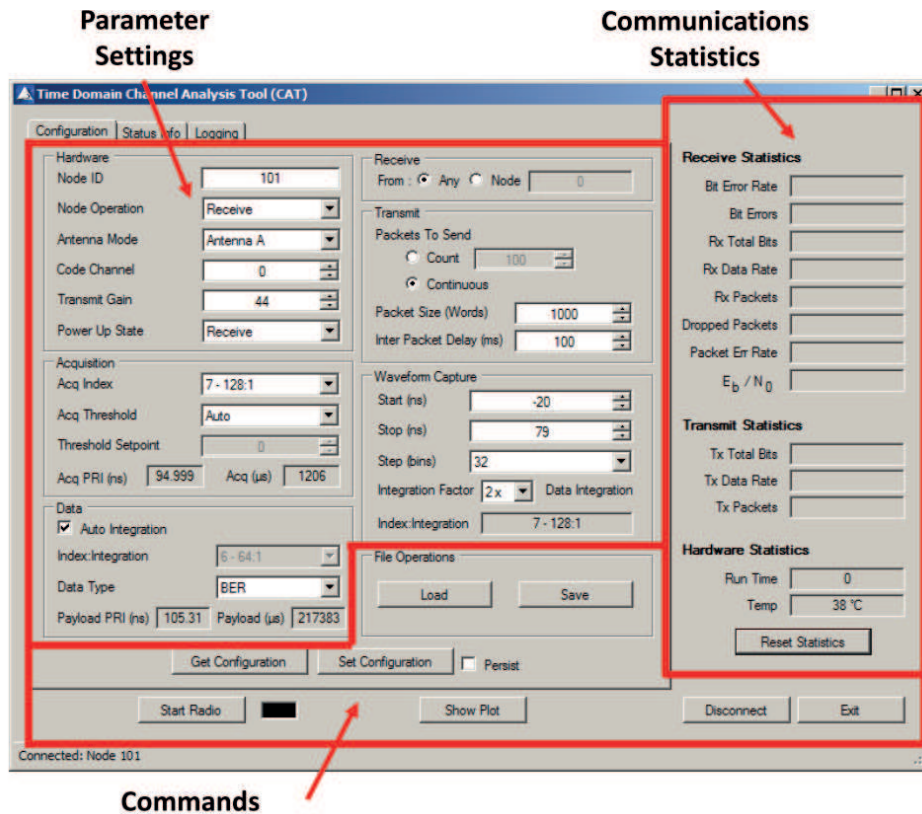


Figure B.4: CAT Configuration Tab showing settings

functionality explained in MRM case.

The various CAT **parameter settings** are subdivided into the *Hardware*, *Acquisition*, *Data*, *Receive*, *Transmit*, and *Waveform Capture Settings*. It is important to note that any settings that define transmission characteristics (such as Acquisition Index, Waveform Capture Start location, etc.) must be common to both the transmit unit and the receive unit. If there is a mismatch between the two, then the receiver will not be able to properly acquire the transmissions, process the received information, or produce waveforms.

### B.2.1 Parameter Settings

*Node Operation* indicates the operating state (Transmit, Receive, or Ambient Scan) of the device. *Antenna Mode* indicates the four supported antenna modes as described in Table B.1. *Code Channel* and *Transmit Gain* parameters have the same meaning w.r.t. the MRM case. *Power Up State* is the state in which the Radio will operate when it is powered up.

Table B.1: Antenna Configuration

Field Entry	Result
Antenna A	Transmit and Receive on Antenna A
Antenna B	Transmit and Receive on Antenna B
TX on A, RX on B	Transmit on Antenna A, Receive on Antenna B
TX on B, RX on A	Transmit on Antenna B, Receive on Antenna A

The Acquisition Settings are described by *Acq PII Index* which determines the operating range at which transmissions can be acquired. Higher is the value then longer is the operating range. *Acq Threshold* determines the threshold (Auto and Manual) for receiving signals. It is preferred set to Auto. *Acq pulse repetition interval (PRI)* is the time interval between individual pulses transmitted in the acquisition portion of the transmitted packet measured in nanoseconds. *Acq* is the amount of time, in microseconds, allocated for the packet acquisition header (this duration constitutes most, but not all, of the communications overhead).

The *Auto Integration* parameter determines the PII index to integrate data. In our measurement campaign "Auto Integration" is not set, then the user can selected a Data Index less than or equal to the Acq Index. This capability allows to reliably acquire packets by sending the data with lower integration. Other Data Setting are out of scope of this thesis and no information are given for brevity.

*Receive Settings* determine whether the receiver will process packets received from any transmitting node (*Any*) or only from a specifically designated node (*Node*). *Transmit Settings* determine the transmitting packets mode, *Packets to Send*, whether a specific number of packets or packets will be sent continuously (*Count* or *Continuous* button respectively). *Inter Packet Delay* is the delay in milliseconds between the transmissions of a packet (available values are 0 to 10.000).

Waveforms captured and displayed by CAT will have a starting and ending point relative to the radio lock spot. The lock spot is a specific point on the received waveform. Any zero crossing is a candidate lock spot. The CAT has been designed to find a zero crossing close to one of the largest amplitude signals. For example, any of the points marked in Figure B.5 with a red circle are likely (and desirable) lock points. *Leading Edge* is an approximate measure of when the receive hooks the considered transmitted waveform. In Fig. B.5 is marked with a vertical green line.

In *Waveform Capture Setting* the *Start* parameter represent the beginning point of a captured waveform in nanoseconds relative to the lock spot. A negative value

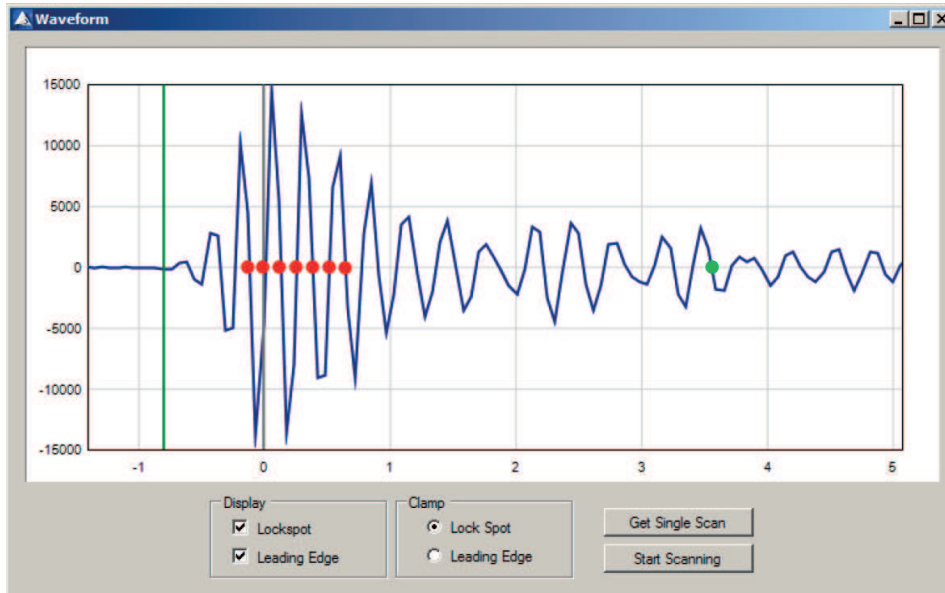


Figure B.5: Sample captured waveform showing potential radio lock spots [4]

will start the waveform prior to the lock spot. A positive value starts the waveform after the lock spot. The maximum number of measurement points in a scan is 4094, i.e. when using a step size of 32 (one measurement every 61 ps), the user may select Start and Stop values between  $-100$  ns and  $+100$  ns. The *Stop* parameter is complementary with respect to Start one. *Step (bins)* is the amount of time between measurements in a scan. A bin is approximately 1.9073 ps in duration. The standard amount of time between readings is 32 bins, or approximately 61.035 ps. *Integration Factor* defines the PII to be used in collecting the waveforms.

# Bibliography

- [1] M. Chiani, A. Giorgetti, M. Mazzotti, R. Minutolo, and E. Paolini, “Target detection metrics and tracking for UWB radar sensor networks,” in *Proc. IEEE Int. Conf. on Ultra-Wideband (ICUWB)*, Sept 2009, pp. 469–474.
- [2] S. Kidera, T. Sakamoto, and T. Sato, “Accurate uwb radar 3d imaging algorithm for complex boundary without range points connections,” in *IEEE Trans. Geoscience and Remote Sensing*, vol. 48, no. 4, Apr. 2010, pp. 1993–2004.
- [3] S. Nag and M. Barnes, “A moving target detection filter for an ultra-wideband radar,” in *Proc. IEEE Radar Conf.*, May 2003, pp. 147–153.
- [4] C. Time Domain “PulseON<sup>®</sup>410 Series tools,” <http://www.timedomain.com>.
- [5] D. Deborja and B. A. Hamilton., *Compilation of State Laws and Regulations Affecting Highway-Rail Grade Crossings*, 6th ed. Federal Railroad Administration (FRA), U.S. Department of Transportation, April 2014.
- [6] I. Forvente, “Existing international rules and regulations on level crossing,” *International Union of Railways (UIC)*, no. 1, july 2012.
- [7] European Parliament and Council of the European Union, “Directive 2004/49/EC,” Brussels, pp. 1–24, 2004.
- [8] S. Lohmeier, R. Rajaraman, and V. Ramasami, “Development of an ultra-wideband radar system for vehicle detection at railway crossings,” in *Proc. IEEE Conf. on Ultra Wideband Syst. and Technologies*, May 2002, pp. 207–211.
- [9] A. Narayanan, P. Brennan, R. Benjamin, N. Mazzino, G. Bochetti, and A. Lancia, “Railway level crossing obstruction detection using MIMO radar,” in *Proc. European Radar Conference (EuRAD)*, Oct 2011, pp. 57–60.

- [10] G. Ermak, A. Vasilev, A. Varavin, I. Popov, V. Noskov, and K. Ignatkov, "Autodyne sensors for hump yard and rail crossing applications," in *Proc. 13th Int. Radar Symposium (IRS)*, May 2012, pp. 209–212.
- [11] M. Watanabe, K. Okazaki, J. Fukae, N. Tamiya, N. Ueda, and M. Nagashima, "An obstacle sensing radar system for a railway crossing application: a 60 GHz millimeter wave spread spectrum radar," in *Proc. IEEE MTT-S Int. Microwave Symp. Digest*, vol. 2, June 2002, pp. 791–794 vol.2.
- [12] R. Campbell, "Vital inductive loop processor detection," Aug 2014.
- [13] G. Kim, J. Baek, H. Jo, K. Lee, and J. Lee, "Design of safety equipment for railroad level crossings using laser range finder," in *Proc. 9th Int. Conf. on Fuzzy Systems and Knowledge Discovery (FSKD)*, May 2012, pp. 2909–2913.
- [14] N. Fakhfakh, L. Khoudour, E. El-Koursi, J. Bruyelle, A. Dufaux, and J. Jacot, "Background subtraction and 3D localization of moving and stationary obstacles at level crossings," in *Proc. 2nd Int. Conf. on Image Process. Theory Tools and Applicat. (IPTA)*, July 2010, pp. 72–78.
- [15] Z. Silar and M. Dobrovolny, "The obstacle detection on the railway crossing based on optical flow and clustering," in *Proc. 36th Int. Conf. on Telecommun. and Signal Process. (TSP)*, July 2013, pp. 755–759.
- [16] M. Govoni, E. M. Vitucci, V. D. Esposti, F. Guidi, G. Tartarini, and D. Dardari, "Study of a UWB multi-static radar for railroad crossing surveillance," in *Proc. IEEE Int. Symp. on Antennas and Propag. and North American Radio Science Meeting*, Vancouver, British Columbia, Canada, 2015, pp. 1–2.
- [17] E. Paolini, A. Giorgetti, M. Chiani, R. Minutolo, and M. Montanari, "Localization capability of cooperative anti-intruder radar systems," in *EURASIP Journal on Advances in Signal Processing*, April 2008, pp. 1–14.
- [18] M. Govoni, G. Boatto, E. Vitucci, V. Degli-Esposti, F. Guidi, and D. Dardari, "UWB over fiber system for railroad crossing surveillance," in *Fotonica AEIT Italian Conference on Photonics Technologies, 2015*, May 2015.
- [19] C. A. Balanis, *Antenna Theory*, 3rd ed. Hoboken, New Jersey: John Wiley & Sons, Inc., 2005.

- [20] V. Degli Esposti, F. Fuschini, E. Vitucci, and G. Falciasecca, “Measurement and modelling of scattering from buildings,” *IEEE Trans. Antennas Propag.*, vol. 55, no. 1, pp. 143–153, Jan 2007.
- [21] F. Fuschini, V. Degli Esposti, and E. Vitucci, “A model for forward-diffuse scattering through a wall,” in *Proc. 4th European Conference on Antennas and Propagation (EuCAP 2010)*, April 2010.
- [22] G. Tartarini and P. Faccin, “Efficient characterization of harmonic and inter-modulation distortion effects in dispersive radio over fiber systems with direct laser modulation,” vol. 46, no. 2, pp. 114–117, 2005.
- [23] M. Jazayerifar, B. Cabon, and J. Salehi, “Transmission of multi-band OFDM and impulse radio ultra-wideband signals over single mode fiber,” *J. of Light-wave Technology*, vol. 26, no. 15, pp. 2594–2603, Aug 2008.
- [24] I. Cox, C.H., E. Ackerman, G. Betts, and J. Prince, “Limits on the performance of rf-over-fiber links and their impact on device design,” *Microwave Theory and Techniques, IEEE Transactions on*, vol. 54, no. 2, pp. 906–920, Feb 2006.
- [25] V. S. Chernyak, *Fundamentals of Multistatic Radar Systems*. Gordon and Breach Science Publisher, 1998.
- [26] D. Dardari, A. Conti, A. Ferner, A. Giorgetti, and M. Win, “Ranging with ultrawide bandwidth signals in multipath environments,” in *Proc. IEEE*, vol. 97, no. 2, Feb 2009, pp. 404–426.
- [27] B. Sobhani, E. Paoletti, A. Giorgetti, M. Mazzotti, and M. Chiani, “Target tracking for uwb multistatic radar sensor networks,” *IEEE Journal of Selected Topics in Signal Processing*, vol. 8, no. 1, pp. 125–136, Feb 2014.
- [28] R. Salman and I. Willms, “3d uwb radar super-resolution imaging for complex objects with discontinuous wavefronts,” in *Proc. IEEE Int. Conf. Ultra-Wideband (ICUWB)*, 2011, pp. 346–350.
- [29] H. L. V. Trees, *Detection, Estimation, and Modulation Theory: Part I*, 2nd ed. New York, NY: John Wiley & Sons, Inc., 2001.
- [30] F. Guidi, N. Decarli, S. Bartoletti, A. Conti, and D. Dardari, “Detection of multiple tags based on impulsive backscattered signals,” *IEEE Transactions on Communications*, vol. 62, no. 11, Nov. 2014.

- [31] F. Fuschini, E. Vitucci, M. Barbiroli, G. Falciasacca, and V. Degli-Esposti, “Ray tracing propagation modeling for future small-cell and indoor applications: a review of current techniques,” in *Radio Science*, june 2015, pp. 469–485.
- [32] Synopsis, “*Software Optsim<sup>TM</sup>*,” <http://optics.synopsys.com/rsoft/rsoft-system-network-optsim.h>